

ABSTRACT

Title of Document: FAILURE MECHANISMS IN
OVERDISCHARGED AND OVERCHARGED
LITHIUM-ION BATTERIES

Christopher Edward Hendricks, Mechanical
Engineering, 2019

Directed By: Professor Michael Pecht, Ph.D., PE
Director, CALCE Electronics Products and
Systems Center
George Dieter Chair Professor Mechanical
Engineering
Professor of Applied Mathematics

Lithium-ion batteries are employed in applications as varied as consumer electronics, electric vehicles, satellites, and airplanes. As lithium-ion battery systems are increasingly scaled to large systems, safety and reliability are paramount.

Catastrophic failure of a lithium-ion battery can cause damage to the host system and pose a risk to human life. While many lithium-ion batteries degrade in a benign fashion, others can enter into thermal runaway, generate gas within the battery, and catch fire and/or spontaneously disassemble. Determining precursors to catastrophic failure will allow for early failure mitigation strategies that can reduce the effects of a thermal runaway or prevent it from occurring in the first place. This research will identify several critical factors affecting performance and safety in lithium-ion batteries that are exposed to overdischarge or overcharge abuse. Lithium-ion batteries

that are operated outside of their intended voltage range can experience both performance and safety degradation. Operation at voltages below the battery manufacturer's recommended lower voltage limit results in overdischarge.

Overdischarge of lithium-ion batteries can lead to copper dissolution, and the use of X-ray photoelectron spectroscopy (XPS) and X-ray absorption fine structure (XAFS) analysis combines surface- and bulk-level analysis to characterize the risk of short circuit due to copper dissolution and re-precipitation. Operation at voltages above the battery manufacturer's recommended upper voltage limit results in overcharge.

Overcharge initiates exothermic reactions within the battery that can lead to thermal runaway. Furthermore, gas is generated during these side reactions, causing pressure buildup within lithium-ion cells as they undergo abuse. Pressure evolution is measured and a model developed to explain the relationship between state of charge, temperature, and internal cell pressure.

FAILURE MECHANISMS IN OVERDISCHARGED AND OVERCHARGED
LITHIUM-ION BATTERIES

By

Christopher Edward Hendricks

Dissertation submitted to the Faculty of the Graduate School of the
University of Maryland, College Park, in partial fulfillment
of the requirements for the degree of
Doctor of Philosophy
2019

Advisory Committee:
Professor Michael Pecht, Chair
Dr. Abhijit Dasgupta
Dr. Bongtae Han
Dr. Chunsheng Wang
Dr. Eric Wachsman

© Copyright by
Christopher Edward Hendricks
2019

Dedication

This dissertation is dedicated to my wonderful and amazing family. My wife, Lisa, has been there with me throughout the entire process and has sacrificed so much to help me achieve my goals. She is the reason for my success, and I cannot possibly thank her enough. My daughters, Nora and Charlotte, and son, Cooper, are huge inspirations to me, and drive me to meet all of my goals. I cannot put into words how thankful I am for each and every one of them. I would also like to dedicate this dissertation to my mom and dad, who helped me follow my dreams from an early age. They provided me with many early opportunities to develop a love of science and math, and ensured that I had every opportunity to succeed.

Acknowledgements

I would like to acknowledge the support of my adviser, Professor Michael Pecht, and the more than 150 companies and organizations that support research activities at the Center for Advanced Life Cycle Engineering (CALCE) at the University of Maryland annually. I would like to acknowledge financial support received through the ARCS Foundation, and in particular Lynn and John Dillon and the Aerospace Corporation. Support was also received through the Naval Surface Warfare Center Carderock Division Naval Innovative Science and Engineering (NISE) program, managed by the NSWC Carderock Division Director of Research, Jack Price. The XAS experiments were performed at the DuPont-Northwestern-Dow Collaborative Access Team (DND-CAT) located at Sector 5 of the Advanced Photon Source (APS). DND-CAT is supported by Northwestern University, E.I. DuPont de Nemours & Col, and the Dow Chemical Company. This research used resources of the Advanced Photon Source, a U.S. Department of Energy (DOE) Office of Science User Facility operated for the DOE Office of Science by Argonne National Laboratory under Contract No. DE-AC02-06CH11357. I received significant mentorship at NSWC Carderock under the guidance of Dr. Azzam Mansour and Dr. Daphne Fuentevilla. Experiment support was provided by my colleagues Dr. Jonathan Ko, Dr. Gordon Waller, Mr. Tom Hoeger, and Mr. Adam Dolezal. I also was supported by my branch heads, Mr. Eric Shields, and Mr. Robert Skelding. Finally, gas analysis support was provided by colleagues at NSWC Indian Head including Dr. Chad Stoltz, Dr. Sean Maharrey, and Mr. Jason Steffin.

Table of Contents

Table of Contents	iv
List of Tables	vi
List of Figures	vii
List of Abbreviations	x
Chapter 1: Introduction	1
1.1 – Motivation	1
1.2 – Problem Statement	5
Chapter 2: Background	7
2.1 – Lithium-ion battery construction and manufacturing	7
2.2 – Lithium-ion battery working principle	10
Chapter 3: Failure modes, mechanisms, and effects analysis of lithium-ion batteries	15
3.1 – Negative Electrode Active Material	18
3.2 – Positive Electrode Active Material	23
3.3 – Current Collectors	25
3.4 – Separator	25
3.5 – Electrolyte	27
3.6 – Cell Terminals and Casing	28
3.7 – Summary	30
Chapter 4: Overdischarge of lithium-ion batteries	31
4.1 – Literature Review	31
4.2 – Research Gaps	39
4.3 – Experimental	40
4.3.1 – Overdischarge procedure	41
4.3.2 – Cell disassembly procedure	43
4.3.3 – Scanning Electron Microscopy	47
4.3.4 – X-ray Photoelectron Spectroscopy	48
4.3.5 – X-ray Absorption Fine Structure	51
4.3.6 – Three-electrode cell	58
4.3.7 – Coin cell	61
4.4 – Results and Discussion	63
4.4.1 – SEM	63
4.4.2 – Three-electrode measurements	70
4.4.3 – Cycling comparison	71
4.4.4 – XPS	81
4.4.5 – XAFS	90
4.4.6 – Discussion	99
Chapter 5: Overcharge of lithium-ion batteries	104
5.1 – Literature Review	104
5.2 – Research Gaps	108
5.3 – Experimental	109
5.3.1 – Cell Puncturing	109

5.3.2 – Overcharge Test	111
5.3.3 – Gas Sampling	113
5.3.4 – Gas Analysis	114
5.4 – Results.....	116
5.4.1 – Overcharge with multiple gas samples	116
5.4.2 – Overcharge with single gas samples	125
5.4.3 – Overcharge without gas samples	126
Chapter 6: Contributions, Future Work, and Conclusions.....	129
Bibliography	134

List of Tables

Table 1: Comparison of secondary battery technologies [1].	2
Table 9: Full cell voltage and the voltage of each electrode with respect to Li/Li ⁺ ...	71
Table 2: Summary of copper reference sample fit parameters	82
Table 3: Average elemental atomic percentage in negative electrode samples.....	83
Table 4: Average elemental atomic percentage in positive electrode samples.....	83
Table 5: Transmission edge steps of the cell samples	93
Table 6: Crystallographic data for Cu ₂ O and Cu(OH) ₂ used for simulations in Artemis	96
Table 7: Local structure parameters calculated from simulated Fourier transforms of EXAFS spectra for 0.25 V cell (uncertainties reported in parentheses).	97
Table 8: Mole fraction of Cu ₂ O and Cu(OH) ₂ for varying storage conditions.....	97
Table 10: Gas species measured during overcharge at approximately 148% SOC..	124

List of Figures

Figure 1: Lithium-ion cell structure.....	9
Figure 2: Ion and electron transport in lithium-ion cells. The battery consists of both a solid phase where lithium ions diffuse into the electrode particles and an electrolyte phase where the ions travel to the opposing electrode.....	13
Figure 3: FMMEA of lithium-ion batteries from [5].....	17
Figure 4: Lithium ion intercalation in graphite and corresponding volume change...	23
Figure 5: Lithium staging in graphite negative electrode. Modified from [70].....	23
Figure 6: Large format cylindrical cell with positive and negative terminals on top.	41
Figure 7: Overview of overdischarge study.....	42
Figure 8: CT scan of cell showing top current collector and connection to terminal via busbar and bottom current collector connected directly to casing.....	44
Figure 9: Jelly-roll with glass rod through center mandrel and elevated over cutting board end view (left) and top view (right).....	46
Figure 10: Negative electrode and positive electrode separated and wound onto separate rollers. The negative electrode is on the left and the positive electrode on the right.	46
Figure 11: Samples removed from electrode sheets	47
Figure 12: Plan view of the APS facilities showing the linear accelerator (LINAC), the booster/injector synchrotron, and the main storage ring [123]	52
Figure 13: Schematic of 5-BM-D XAFS setup. The incident X-ray beam passes through a detector measuring the initial intensity of the X-rays. The X-rays strike the sample and a fraction pass through to be measured at the transmission detector. The remaining X-rays pass through a reference foil before their intensity is measured again. A fluorescence detector placed perpendicular to the transmission detectors can measure fluoresced X-rays.....	53
Figure 14: Delamination of negative electrode from copper current collector.....	55
Figure 15: Image of graphite flake and graphite samples captured on tape	55
Figure 16: X-ray sample holder mounted on motorized stage. Flakes of graphite from the negative electrode are taped to the holder and positioned in the X-ray path for XAFS measurements.	56
Figure 17: K-edge step for reference Cu foil.	57
Figure 18: Three-electrode assembly.....	59
Figure 19: Electrode stack assembly.....	60
Figure 20: Lithium reference electrode.....	60
Figure 21: Negative electrode with current collector folded over.	62
Figure 22: Coin cell schematic	62
Figure 23: SEM micrograph of negative electrode from a healthy cell.....	63
Figure 24: SEM micrograph of negative electrode from a healthy cell at 10,000x magnification.	64
Figure 25: SEM micrograph of positive electrode from a healthy cell.....	64
Figure 26: SEM micrograph of positive electrode from a healthy cell at 10,000x magnification.	65
Figure 27: SEM micrograph of graphite particle in a cell overdischarged to 0 V. Deposits on the surface of the particle can be clearly observed at 15,000x magnification.	66

Figure 28: SEM micrograph of graphite particle in a cell overdischarged to 0.25 V. Deposits on the surface of the particle can be clearly observed at 10,000x magnification.	67
Figure 29: SEM micrograph of cathode particle in a cell overdischarged to 0 V	68
Figure 30: SEM micrograph of cathode particle in a cell overdischarged to 0.25 V .	68
Figure 31: EDS spectra for a negative electrode from a healthy cell	69
Figure 32: EDS spectra for a negative electrode from a cell overdischarged to 0 V..	70
Figure 33: Overdischarge of three-electrode pouch cell to 0 V.....	71
Figure 34: Cycling following a single overdischarge event	72
Figure 35: Capacity fade for 3 cells overdischarged to 0 V and then cycled within nominal voltage range of 2.5 V to 4.1 V.....	73
Figure 36: Capacity fade for 3 cells overdischarged to 0.25 V and then cycled within nominal voltage range of 2.5 V to 4.1 V.....	73
Figure 37: Capacity fade for 3 cells overdischarged to 0.5 V and then cycled within nominal voltage range of 2.5 V to 4.1 V.....	74
Figure 38: Impedance prior to cycling.....	75
Figure 39: Impedance after 40 cycles	75
Figure 40: 0.25 V cell 1 impedance	76
Figure 41: 0.25 V cell 2 impedance	77
Figure 42: 0.25 V cell 3 impedance	77
Figure 43: 0.5 V cell 1 impedance	78
Figure 44: 0.5 V cell 2 impedance	78
Figure 45: 0.5 V cell 3 impedance	79
Figure 46: 0 V cell 1 impedance	80
Figure 47: 0 V cell 2 impedance	80
Figure 48: 0 V cell 3 impedance	81
Figure 49: Copper reference samples, Cu _{2p_{3/2}} region	82
Figure 50: Cu _{2p_{3/2}} region of 0.5 Volt cell negative electrode. Slight copper peak with binding energy around 933 eV is observed.....	84
Figure 51: C1s (top) and Cu _{2p_{3/2}} (bottom) spectra for negative electrodes from samples 1, 2, 3, and 5.....	85
Figure 52: C1s (top) and Cu _{2p_{3/2}} (bottom) spectra for positive electrodes from samples 1, 2, 3, and 5.....	86
Figure 53: C1s spectra during Argon ion sputtering. Each minute of sputtering is equivalent to the removal of 8 nm of SiO ₂	87
Figure 54: Cu _{2p_{3/2}} spectra during Argon ion sputtering. Each minute of sputtering is equivalent to the removal of 8 nm of SiO ₂	87
Figure 55: C1s spectra before and after sputtering.	88
Figure 56: Cu _{2p_{3/2}} spectra before and after sputtering.....	88
Figure 57: C1s spectra from a charged negative electrode	89
Figure 58: Cu _{2p_{3/2}} spectra from a charged negative electrode	90
Figure 59: XANES spectra for relevant copper compounds.	91
Figure 60: X-ray absorption near edge structure for overdischarged cells	92
Figure 61: XANES spectra for multiple locations within a cell overdischarged to 0.25V.....	92

Figure 62: XANES spectra for multiple locations within a cell overdischarged to 0.25 V and recharged prior to disassembly.....	93
Figure 63: Comparison of sample from 0 V cell to the reference spectra of Cu ₂ O and Cu(OH) ₂ . Peaks labeled “A” through “C” on the left (XANES) and right (1 st Derivative of XANES) are associated with peaks in the reference compounds.	94
Figure 64: Fourier transform of EXAFS data. All samples exhibit similar traits, with differences in the peak magnitudes. Comparing a sample (0 V) to the reference EXAFS of Cu ₂ O and Cu(OH) ₂	95
Figure 65: Model fit comparison to a 0 V cell. Close agreement between the experimental and model data indicate that it is sufficient to model the spectra as a linear combination of Cu ₂ O and Cu(OH) ₂	97
Figure 66: Cobalt K-edge XANES data for a 0 V cell, 2.5 V cell, and the reference NCA powder.	99
Figure 67: Nickel K-edge XANES data for a 0 V cell, 2.5 V cell, and the reference NCA powder.	99
Figure 68: Schematic of cell cross section showing a "safe penetration zone" at the bottom of the cell. The cell is case positive and the only current collector present at the bottom of the cell is also the positive electrode.	110
Figure 69: Cell puncturing assembly with option of gas sampling	110
Figure 70: Cell puncturing assembly with limited added free volume	111
Figure 71: Constant current overcharge test	113
Figure 72: Cell with puncturing mechanism, pressure transducer, and solenoid valve (left) and gas sampling manifold (right)	114
Figure 73: Gas sample extraction using an air-tight GC/MS syringe.....	116
Figure 74: Pressure and voltage plot for cell 1.	117
Figure 75: Failed cell with ejected terminal end and electrode jelly roll.....	118
Figure 76: Temperature on side of cell 1 during overcharge.....	118
Figure 77: Pressure and voltage plot for cell 2.	120
Figure 78: Cell 2 following the overcharge test. The majority of the electrode jelly roll remained inside of the cell despite an internal pressure of 95 psi (absolute) immediately prior to failure.	120
Figure 79: Temperature on side of cell 3 during overcharge.....	121
Figure 80: Pressure and voltage plot for cell 3.	122
Figure 81: Cell 3 following overcharge. The electrode jelly roll mostly remained in the cell except for some ribbons of copper current collector.....	122
Figure 82: Temperature on side of cell 3 during overcharge.....	123
Figure 83: Chromatogram before and during overcharge with the curves offset for clarity.	124
Figure 84: Overcharge test results with single gas sample taken	126
Figure 85: Overcharge at 26A (C/2 rate) can be separated into four different regimes. Failure occurs shortly after the cell enters into stage IV, in which rapid increases in voltage and pressure are observed.	127
Figure 86: Overcharge of cells at 10.4 A (C/5) voltage (top), pressure (middle), temperature (bottom).	128

List of Abbreviations

A – Amperes
AFM – Atomic Force Spectroscopy
Ah – Ampere hours
B.E. – Binding Energy
BMS – Battery Management System
CEI – Cathode Electrolyte Interphase
CFD – Computational Fluid Dynamics
CID – Current Interrupt Device
CT – Computed Tomography
DEC – Diethyl Carbonate
DMC – Dimethyl Carbonate
DPA – Destructive Physical Analysis
DSC – Differential Scanning Calorimetry
EC – Ethylene Carbonate
EDS – Energy Dispersive Spectroscopy
EMC – Ethyl-Methyl Carbonate
EXAFS – Extended X-ray Absorption Fine Structure
FEA – Finite Element Analysis
FIB – Focused Ion Beam
FTIR – Fourier Transform Infrared
FMMEA – Failure Modes, Mechanisms, and Effects Analysis
FVM – Finite Volume Method
FWHM – Full width at half maximum
GC – Gas Chromatography
ICP – Inductively Coupled Plasma
LCO – Lithium cobalt oxide, LiCoO_2
LFP – Lithium iron phosphate, LiFePO_4
LTO – Lithium titanate oxide, $\text{Li}_4\text{Ti}_5\text{O}_{12}$
MS – Mass Spectrometry
NCA – Nickel cobalt aluminum oxide, $\text{LiNi}_x\text{Co}_y\text{Al}_{1-x-y}\text{O}_2$
NCM – Nickel cobalt manganese oxide, $\text{LiNi}_x\text{Co}_y\text{Mn}_{1-x-y}\text{O}_2$
NMR – Nuclear Magnetic Resonance
PC – Propylene Carbonate
PHM – Prognostics and Health Management
SEI – Solid Electrolyte Interphase
SEM – Scanning Electron Microscopy
SOC – State of Charge
SOH – State of Health
TEM – Transmission Electron Microscopy
TGA – Thermogravimetric Analysis
TTF – Time To Failure
V – Volts
VC – Vinylene Carbonate
Wh/kg – Gravimetric Energy Density, Watt-hours per kilogram

Wh/L - Volumetric Energy Density, Watt-hours per liter
XAFS – X-ray Absorption Fine Structure
XANES – X-ray Absorption Near Edge Structure
XPS – X-ray Photoelectron Spectroscopy
XRD – X-ray Diffraction

Chapter 1: Introduction

1.1 – Motivation

Lithium-ion batteries are rechargeable (secondary) energy storage devices used in a variety of applications since becoming commercially available in the early 1990's [1]. Compared to non-rechargeable (primary) batteries, Lithium-ion batteries can be repeatedly charged and discharged, whereby external electrical energy is converted to chemical energy and chemical energy is converted into electrical energy, respectively. Compared to a primary battery that needs to be replaced after its useable chemical energy has been converted into electrical energy, secondary batteries offer many benefits. In applications where replacing a battery is either too costly or inconvenient, secondary battery technologies are advantageous.

Other secondary battery technologies include lead acid (Pb-Acid), Nickel Metal Hydride (NiMH), and Nickel Cadmium (NiCd). Each of these technologies has their own distinct advantages and disadvantages, and different use scenarios may dictate the desired technology. Table 1 outlines a number of features for each of the battery chemistries. The columns in the table provide the nominal voltage of an electrochemical cell, the gravimetric energy density, the volumetric energy density, and the cycle life. The nominal voltage of the cell is governed by the electrochemical potential between the battery electrodes and is measured in Volts. The gravimetric energy density is the number of Watt-hours per kilogram (Wh/kg) that the given technology can deliver in electrical energy. The volumetric energy density is the number of Watt-hours per liter (Wh/L) that the given technology can deliver. The

cycle life is a measure of the number of charge and discharge cycles the battery defined as the number of full cycles before the battery's capacity or resistance decreases or increases as a percentage of its original capacity or resistance.

Table 1: Comparison of secondary battery technologies [1].

Battery Technology	Nominal Cell Voltage (V)	Gravimetric Energy Density (Wh/kg)	Volumetric Energy Density (Wh/L)	Cycle Life Until 20% Loss of Capacity at 100% Depth of Discharge
Lead Acid	2.0	35	70	200-300
Nickel Cadmium	1.2	40	135	500-1000
Nickel Metal Hydride	1.2	100	235	500-1000
Lithium-ion	3.8 / 3.2*	200	570	1000+

* Most lithium-ion batteries have a nominal voltage of 3.8 V; however Lithium Iron Phosphate (LiFePO₄)-based batteries exhibit a lower nominal voltage of 3.2V.

Lithium-ion batteries have a higher cell voltage, higher energy density, and longer cycle life than other secondary battery technologies. Furthermore, lithium-ion batteries tend to have higher power capability, low self-discharge rate, and no memory effect when undergoing partial charge/discharge cycles [1-4] compared to the other secondary battery technologies. While historically more mature technologies such as Pb-Acid have been utilized where gravimetric energy density (Wh/kg) is not a concern, Lithium-ion batteries are rapidly expanding to fill these roles due to their many advantages. As a result, lithium-ion batteries have been used in consumer electronics, electric vehicles, unmanned autonomous vehicles, airplanes, satellites, grid storage, back-up power supplies, and many other applications.

Failure in lithium-ion batteries can be classified as either performance-based failure or catastrophic failure. Performance-based failure describes the degradation of

the battery, resulting in insufficient power or a decrease in the deliverable energy. As with many electrochemical storage technologies, degradation is an inevitable side effect of operation that eventually results in a battery that can no longer meet its intended requirements. Performance degradation often results in benign failure and is not the subject of this work.

Alternately, catastrophic failures of batteries can result in rapid disassembly of the battery, fire, and destruction of the host-device. This type of failure is often referred to as thermal runaway, due to the series of exothermic reactions that continue fueling a progressively dangerous event. If heat is generated inside a battery or in close proximity to the battery, and the heat generation rate outweighs the heat dissipation rate, the battery is at risk of entering thermal runaway. The source of heat generation could be elevated ambient temperatures, overcharge of the battery, or a short circuit. Once thermal runaway is initiated, it is nearly impossible to stop. The battery may undergo any number of failure modes; however, the worst case scenario results in the cell splitting open, releasing flaming electrolyte and battery components into the environment in addition to hazardous gases. Advanced warning of conditions leading up to thermal runaway could allow for mitigation strategies to improve the safety of battery powered systems.

Avoiding thermal runaway requires knowledge of lithium-ion battery failure modes, mechanisms, and effects to design mitigation strategies [5]. Cell manufacturers, battery pack designers, and battery algorithm developers have all implemented a variety of strategies to try to avoid, or at least lessen the impact of thermal runaway. On the cell level, manufacturers take advantage of internal disks

called current interrupt devices (CID) that prevent further current flow when excessive gas is generated, vents to release the internal pressure within the cell, and inclusion of additives to the electrolyte, modifications to the separator (shutdown mechanism or ceramic coating), or selection of electrode active materials. On the pack level, fuses and diodes can prevent excessive charge from being delivered or removed from the battery. Furthermore, active and passive thermal management strategies try to counteract excessive heat generation to extend the life and improve the safety of the battery pack. A battery management system (BMS) is used to set voltage, current, and temperature operational limits on the battery. The BMS also contains algorithms for estimating the internal state of the battery such as its state of health (SOH) and state of charge (SOC). The BMS tries to ensure that the battery is maintained within safe operating limits in addition to alerting the user or host device of anomalous behavior.

However, despite the number of preventative measures taken, lithium-ion batteries continue to experience catastrophic failures. In the mid 2000's, millions of lithium-ion batteries manufactured by Sony were recalled due to concerns about battery fires in laptops [6]. Additionally, as lithium-ion batteries are used in applications with harsher environmental stresses such as electric vehicles and aerospace, catastrophic failures have captured the media's attention. The lithium-ion battery fires that grounded the Boeing Dreamliner 787 in the first half of 2013 may have been avoided if proper consideration of the operating conditions (i.e. altitude and low temperatures) was factored into the risk analysis [7]. Several incidents involving Tesla Model S electric cars resulted from mechanical damage leading to a

short circuit in the battery pack. Better protection of the battery pack is needed and was later added by Tesla in the form of a titanium barrier and in-depth analysis of the danger that road debris presented [8]. Fires in hoverboards, popular Lithium-ion battery-powered consumer devices, caused the devices to be banned from passenger flights [9], and E-cigarette failures have led to bodily harm and death in users [10]. Samsung had to recall its popular Samsung Galaxy Note 7 due to several reports of spontaneous disassembly of the cell phones accompanied with fire [11]. Clearly, despite their many advantages, lithium-ion batteries continue to pose safety issues. A greater understanding of failure mechanisms leading up to catastrophic failure is needed to develop improved mitigation strategies.

1.2 – Problem Statement

Lithium-ion batteries and their failure mechanisms are the source of significant research. Researchers have investigated ways to prevent and mitigate failure at the cell-, battery-, and module-level through physical, electrical, and software safety devices. Despite commercialization for nearly three decades, lithium-ion batteries continue to fail for a myriad of reasons. Externally measurable signals of impending failure such as voltage and temperature, are often observed too late to prevent failure outright. Therefore, it is necessary to study the progression of failure by observing precursors to the failure event. These precursors include gas generation, initiation of exothermic reactions, dissolution of metal species, and formation of internal short circuits. This research will investigate prominent and likely failure mechanisms in lithium-ion batteries when they are operated outside of their intended

voltage limits, as is the case with overdischarge and overcharge. The chemistry of dissolved copper due to overdischarge conditions is measured using both surface- and bulk-sensitive spectroscopy techniques. The impact of copper dissolution on performance and safety is evaluated in commercial lithium-ion cells and related to cell design parameters. Overcharge abuse is studied through continuous internal pressure measurement in modified cells to establish a relationship between externally measurable quantities (voltage, current, external temperature) and the internal state of the electrochemical cell (pressure). The progression of pressure rise in the cell can be used to predict the likelihood of a cell bursting and the impact on adjacent cells in a pack configuration.

Chapter 2: Background

2.1 – Lithium-ion battery construction and manufacturing

Lithium-ion batteries are complex electrochemical systems with a number of permutations based on electrode chemistry. At the most fundamental level, lithium-ion batteries are a class of electrochemical energy storage technology whereby the charge carrier is a lithium ion. Depending on the electrode selection, the lithium ions will undergo different oxidation and reduction reactions at the electrodes when the battery is charged and discharged. For the majority of commercial lithium-ion batteries, the negative and positive electrodes undergo an insertion reaction in which the lithium ions are accommodated in the lattice structure.

Lithium-ion battery electrodes are heterogeneous, porous composite structures. The electrodes are produced by applying a slurry composed of a solvent, the active material, binder, and electronically conducting particles to a metal foil current collector. The most common negative electrode in commercial batteries is carbon-based, such as graphite; however, alternative chemistries are being researched including silicon, tin, and lithium titanate [12]. The carbon slurry is usually applied to a copper foil that acts as a current collector for electron transport. The positive electrode includes a variety of compounds, such as lithium cobalt oxide (LiCoO_2), lithium manganese dioxide (LiMn_2O_4), lithium iron phosphate (LiFePO_4), or various oxides consisting of mixtures of cobalt, aluminum, manganese, and/or nickel [13]. The positive electrode slurry is usually applied to an aluminum foil current collector.

Between the negative and positive electrodes, a separator is employed that is ionically conductive, but electronically insulating. The separator prevents short

circuiting and direct transfer of electrons between the two electrodes, but allows lithium ions to migrate freely. The separator is typically a polymeric sheet composed of polyethylene (PE) or polypropylene (PP). Some separators employ ceramic coatings to inhibit lithium dendrite growth or feature a multi-layer design whereby the inner layer can melt and fill the pores of the remainder of the separator [14].

Advances in solid state batteries utilize a solid electrolyte; however, the technology is still under development and not widely commercialized.

A simplified schematic of a unit cell stack is shown in Figure 1. The current collector is typically coated on both sides and this unit cell is repeated to increase the energy storage capabilities of the battery. The entire cell structure can be stacked, rolled, or wound together to form a “jelly-roll” which is then placed in the cell case or housing. Once the electrode assembly is placed in its cell housing, the cell is filled with an electrolyte that facilitates ion transport. The electrolyte fills the pores in the electrode structure to enable lithium ions to penetrate into the full electrode. For use in lithium-ion batteries, the electrolyte must be ionically conductive, electrically insulating, and have a wide stable voltage and temperature window. The majority of lithium-ion batteries utilize an organic electrolyte consisting of a lithium salt dissolved in a mixture of organic carbonate solvents. Early lithium-ion batteries used propylene carbonate (PC); however, research has demonstrated that the propylene carbonate forms a solvation sheath around the lithium ions and cause exfoliation of the graphite during intercalation [15, 16]. The primary solvent typically used is ethylene carbonate (EC) combined with linear carbonate solvents such as dimethyl carbonate (DMC), diethyl carbonate (DEC), and ethyl methyl carbonate (EMC) [17–

20]. Sometimes a small percentage of vinylene carbonate (VC) is included to promote a healthy solid electrolyte interphase layer on the carbon-based negative electrode [21]. A lithium salt is incorporated into the electrolyte mixture, most often lithium hexafluorophosphate (LiPF_6) for commercial lithium-ion batteries. Further additives are also included in the electrolyte mixture to act as flame retardants, reduce gas generation, stabilize the solid electrolyte interphase layer, protect the positive electrode, enhance solvation, inhibit corrosion, and improve wettability [22].

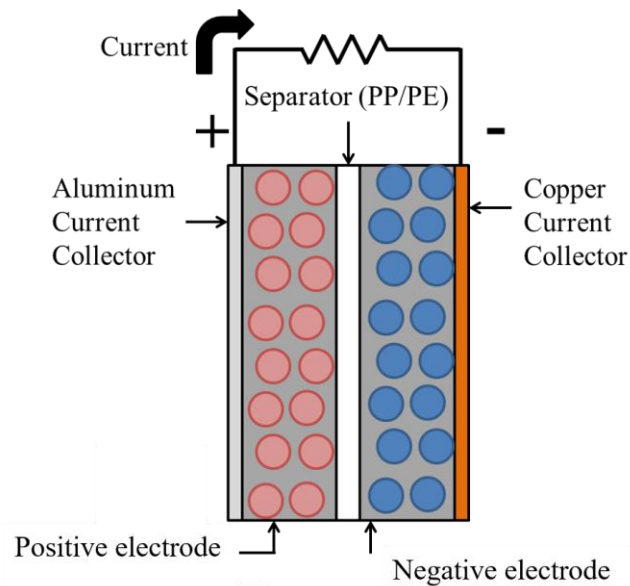


Figure 1: Lithium-ion cell structure

When the lithium-ion cell is assembled, the housing is sealed, for example, by crimping, welding, or heat-sealing. The cell then undergoes formation cycling in which a charge/discharge routine is implemented with the aim of forming a passivation layer on the negative electrode. The formation of a passivation layer, also known as the solid electrolyte interphase (SEI) layer, is essential to the long-term stability of a lithium-ion cell. Without a passivation layer, the electrolyte would

continue to react with the negative electrode, resulting in a loss of active lithium and charge storage capabilities [23–26]. Formation cycling is often performed at a slow rate to enable the formation of the SEI; however, the protocol differs from manufacturer to manufacturer and is often a proprietary trade secret.

After formation cycling, the cell can be opened back up to release gases formed during the formation of the SEI layer and then resealed. This is more typical of pouch cells due to the ease of re-sealing the packaging after purging the formation gases. In hard-case cells, such as cylindrical or prismatic cells, the gas remains in the cell for the duration of the cell's life. Cells are typically monitored and screened to make sure internal short circuits due to latent manufacturing defects are identified. Cells can then be stored, shipped to the end user, or shipped to a battery pack assembler.

2.2 – Lithium-ion battery working principle

Commercial Lithium-ion batteries operate based on an insertion principle called intercalation, in which lithium ions are accommodated in the lattice structures of both electrodes. The lithium ions are inserted into the electrode undergoing a reduction reaction and extracted from the electrode undergoing the oxidation reaction. The electrode undergoing reduction/oxidation depends on if the battery is being charged from an external power source or discharged through a load. When a lithium-ion battery is charged, an external power supply drives electrons to the battery's negative electrode. In lithium-ion battery literature, the electrode with the lower potential is typically referred to as the anode, regardless of whether it is undergoing

oxidation (during discharge) or reduction (during charge). For clarity, the term negative electrode will be used in place of anode. Similarly, positive electrode will be used instead of cathode. The negative electrode's active material is typically composed of graphite or other carbon-based materials. For carbon based electrodes, lithium ions intercalate into the electrode's active material according to the relationship:



A graphite electrode that is completely intercalated with lithium contains one lithium atom for every six carbon atoms, whereas a partially lithiated graphite negative electrode, has lithium in alternating layers of the structure and undergoes a number of stages [27] including LiC_{12} (also written as $Li_{0.5}C_6$), LiC_{18} ($Li_{0.33}C_6$), LiC_{30} ($Li_{0.2}C_6$), and LiC_{60} ($Li_{0.1}C_6$). The potential of a fully intercalated graphite electrode is very close to the potential of metallic lithium. This can lead to plating of metallic lithium as the preferred reaction instead of intercalation [28–37]. Plating occurs when diffusion is inhibited, such as charging at low temperatures or fast charging, or when the active material balance is skewed towards the positive electrode. Plating of metallic lithium can cause growth of dendritic structures and short circuiting in the cell, leading to safety concerns. To avoid this, manufacturers often create cells with excess negative electrode to minimize the chance of plating and define operating conditions to avoid charging at extreme temperatures or rates.

When the battery is being charged, lithium-ions are concurrently removed from the positive electrode. In lithium-ion battery literature, the positive electrode is the electrode with a higher potential. Lithium ions deintercalate from the electrode by

diffusing out of the electrode active material's structure into the electrolyte. In some positive electrodes, only partial removal of lithium is possible without destabilizing the crystal structure. Therefore, there is a difference between theoretical and achievable energy densities on the material level.

Lithium ions travel between electrodes through an ionically conductive electrolyte and a porous separator as seen in

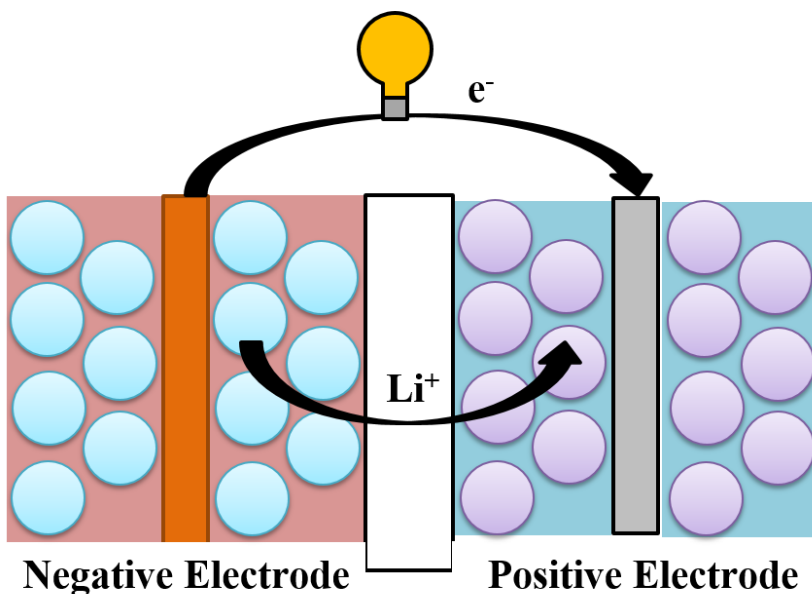


Figure 2. The separator typically has “micropores” that allow ions to pass through but prevent contact of the electrodes and its thickness is often optimized for performance. A thin separator is desirable to reduce the internal resistance of the cell and improve energy density; however, too thin of a separator can more easily be damaged or compromised if the cell undergoes compression. Separators are often on the order of 25 microns thick for many applications.

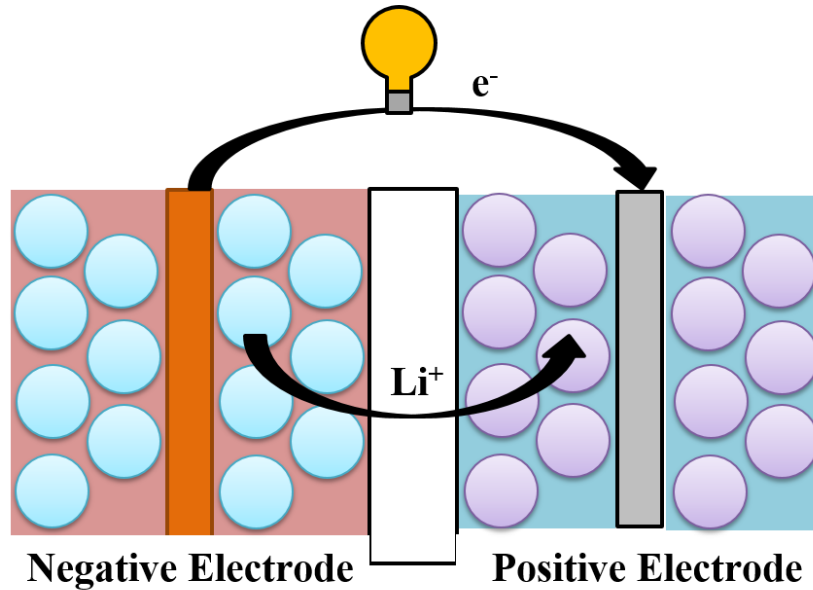


Figure 2: Ion and electron transport in lithium-ion cells. The battery consists of both a solid phase where lithium ions diffuse into the electrode particles and an electrolyte phase where the ions travel to the opposing electrode

The voltage of a lithium-ion cell is determined by the potential difference between the electrodes, ohmic polarization, and charge polarization. As lithium is intercalated or de-intercalated, the potential of the electrode (as measured compared to a standard reference such as Lithium metal) decreases or increases, respectively. This can be considered the half-cell potential of a given electrode. When combined with another counter electrode, the full cell has an open circuit voltage that is simply the difference between each of the half-cell potentials. When a battery is either charged or discharged, lithium ions will begin to diffuse out of the oxidizing electrode, diffuse through the electrolyte, and diffuse into the reducing electrode. The internal ohmic resistance of the battery itself arises as a combination of the current collectors, porous electrodes, electrolyte, and separator stack, and causes a voltage drop when current is applied to the battery. Furthermore, lithium ion concentration gradients can develop because diffusion of the ions into the porous electrode is the

rate limiting step. This concentration gradient also has an effect on the voltage of the cell.

Chapter 3: Failure modes, mechanisms, and effects analysis of lithium-ion batteries

Portions of this chapter are extracted from the article, A failure modes, mechanisms, and effects analysis (FMMEA) of lithium-ion batteries, published in 2015 in the Journal of Power Sources [5].

Lithium-ion batteries are rechargeable, meaning that they can be charged and discharged repeatedly throughout their life. However, lithium-ion battery performance eventually degrades until the battery no longer meets the requirements of the intended use. This is seen by the user as a reduced runtime due to a diminished battery capacity or due to increased internal resistance. Loss of capacity is associated with loss of cyclable lithium in the cell and active material dislocation and isolation. The loss in capacity is often referred to as capacity fade. Degradation initially manifests in an approximately linear decrease in deliverable capacity. After the battery reaches approximately 20% loss in capacity, the degradation rate often increases resulting in rapid capacity fade. Many manufacturers consider this 20% loss in capacity as end-of-life because the battery becomes increasingly unreliable at this point. Alternatively, increased internal resistance results in lower power performance and achievable discharge capacity at various operating currents. Thickening of the solid electrolyte interphase (SEI) layer on the negative electrode and the cathode electrolyte interphase (CEI) on the positive electrode increases internal battery resistance, leading to a larger ohmic drop when discharging the battery and increased ohmic heating. Performance degradation depends on numerous environmental and usage factors such as charge/discharge rate, operating temperature, upper voltage cutoff, lower voltage cutoff, and ambient pressure. Manufacturers often specify limits

for the battery's voltage, current, temperature, and pressure. As long as the battery is operated within these limits, it can be considered to undergo typical use scenarios. If a lithium-ion battery is operated outside of these limits, or if the battery is poorly constructed, it can undergo catastrophic failure.

Due to the many ways in which a battery can fail, a failure modes, mechanisms, and effects analysis (FMMEA) is a useful step to determine likelihood and severity of failure under various operating conditions, both typical and abusive. FMMEA is “a systematic methodology to identify potential failure mechanisms and models for all potential failure modes, and to prioritize failure mechanisms” [38] and it expands upon the traditional FMEA approach as it considers failure mechanisms and their role in failure. Failure mechanisms are identified as the “processes by which physical, electrical, chemical, and mechanical stresses induce failures” [39], and represent a fundamental first-principles initiator of failure. In contrast, failure modes are the visible indicator of failure, and it may not be easily observed without detailed failure analysis. The way in which the failure mechanism impacts device reliability is the failure effect. Inclusion of failure mechanisms is critical in a physics-of-failure approach to understanding the role that the environment plays in accelerating failure. As a result, models can be developed to predict the onset and evolution of a failure mechanism to be used in diagnostics, prognostics, and health management [40, 41].

A FMMEA was performed for lithium-ion batteries in [5] and is summarized in Figure 3. The table contains a detailed list of the various components within a battery, their failure modes, mechanisms, effects, and causes. Furthermore, the type

of mechanism (overstress vs. wearout), the likelihood, severity, and ease of detection of the failure mechanism are detailed.

Battery Component	Potential Failure Mode(s)	Potential Failure Mechanism(s)	Mechanism Type	Observed Effect	Potential Failure Causes	Likelihood of Occurrence	Severity of Occurrence	Ease of Detection
Anode (Active Material)	Thickening of solid electrolyte interphase layer	Chemical reduction reaction and deposition	Wearout	Increased charge transfer resistance, reduction of capacity, reduction of power	Chemical side reactions between lithium, electrode, and solvent	High	Low	High
	Particle fracture	Mechanical stress	Overstress	Reduction of capacity, reduction of power	Intercalation stress	Moderate	Low	Low
	Reduced electrode porosity	Mechanical degradation	Wearout	Increased diffusion resistance, reduction of capacity, reduction of power	Dimensional changes in electrode	Moderate	Low	Low
	Lithium plating and dendrite growth on anode surface	Chemical reaction	Wearout	Can cause short circuit if dendrites puncture separator	Charging the battery at low temperatures or high rates	Low	High	Low
Anode (Current Collector)	Free copper particles or copper plating	Chemical corrosion reaction and dissolution	Wearout	Increased resistance, reduction of power, reduction of current density	Overdischarge of the battery	Low	High	Low
Cathode (Active Material)	Thickening of solid electrolyte interphase layer	Chemical reduction reaction and deposition	Wearout	Increased charge transfer resistance, reduction of capacity, reduction of power	Chemical side reactions between lithium, electrode, and solvent	High	Low	High
	Particle fracture	Mechanical stress	Overstress	Reduction of capacity, reduction of power	Intercalation stress	Moderate	Low	Low
	Reduced electrode porosity	Mechanical degradation	Wearout	Increased diffusion resistance, reduction of capacity, reduction of power	Dimensional changes in electrode	Moderate	Low	Low
	Gas generation and bloating of cell casing	Thermally driven electrode decomposition	Overstress	Reduction of capacity	Overcharge of the battery or short circuit	Low	High	Low
Cathode (Current Collector)	Pitting corrosion of aluminum	Chemical corrosion reaction	Wearout	Increased resistance, reduction of power, reduction of current density	Overcharge of the battery	Low	Moderate	Low
Battery Component	Potential Failure Mode(s)	Potential Failure Mechanism(s)	Mechanism Type	Observed Effect	Potential Failure Causes	Likelihood of Occurrence	Severity of Occurrence	Ease of Detection
Separator	Hole in separator	Mechanical damage	Overstress	High heat generation due to joule heating, bloating of cell casing, drastic voltage reduction	Dendrite formation, external crushing of cell	Low	High	Moderate
	Closing of separator pores	Thermally induced melting of separator	Overstress	Inability to charge or discharge battery	High internal cell temperature	Low	High	High
Lithium ions	Reduction in lithium ions, thickening of solid electrolyte interphase layer	Electrolyte reduction and solid product formation	Wearout	Reduction of capacity	Chemical side reactions between lithium, electrodes, and solvent	High	Low	High
Electrolyte Salt	Decrease in lithium salt concentration	Chemical reduction reaction and deposition	Wearout	Increased diffusion resistance	Chemical side reactions between lithium, electrodes, and solvent	High	Low	High
Organic Solvents	Gas generation and bloating of cell casing	Chemical decomposition of solvent	Overstress	Increased diffusion resistance, and may lead to thermal runaway	High external temperature, overcharging of the cell	Low	High	Low
	Thickening of solid electrolyte interphase layer	Chemical reduction reaction and deposition	Wearout	Increased charge transfer resistance, reduction of capacity, reduction of power	Chemical side reactions between lithium, electrodes, and solvent	High	Low	High
Terminals	External corrosive path between positive and negative leads	Chemical corrosion reaction	Wearout	High heat generation due to joule heating, bloating of cell casing, drastic voltage reduction	Inadvertent shorting of the terminals	Low	High	Moderate
	Solder cracking	Thermal fatigue Mechanical vibration fatigue	Wearout	Loss of conductivity between battery and host device	Circuit disconnect	Low	Moderate	High
Casing	Internal short circuit between anode and cathode	Mechanical stress	Overstress	High heat generation due to joule heating, bloating of cell casing, drastic voltage reduction	External load on cell	Low	High	Moderate

Figure 3: FMMEA of lithium-ion batteries from [5].

3.1 – Negative Electrode Active Material

The vast majority of commercial lithium-ion batteries utilize a carbon-based negative electrode. Capacity loss can be partially attributed to the reactivity between the negative electrode and the organic solvents used in lithium-ion battery electrolytes. Carbon-based negative electrodes react with ethylene carbonate (EC) or dimethyl carbonate (DMC) [15], two common solvents in lithium-ion battery electrolytes. As a battery is cycled, new reaction sites become available due to electrode expansion and contraction as a result of lithium-ion intercalation and de-intercalation from the negative electrode. Capacity fade is a wearout failure mechanism that manifests as a chemical reduction reaction at the electrode. The failure mode is the thickening of the SEI layer, which is hard to detect without disassembling a cell. Research into the composition and morphology of the SEI layer has provided insights into the capacity and power fade of lithium-ion batteries. Due to the fragile nature of the SEI layer, researchers have attempted to perform studies with minimal cell disassembly. Nuclear magnetic resonance (NMR) imaging of lithium-ion batteries has been performed on lithium-ion batteries with graphite negative electrodes to elucidate the SEI growth mechanism [42–44]. If cell disassembly is performed, the procedure needs to take place in a glove box purged with an inert gas (often argon) with a low water vapor and oxygen environment (<5 ppm of each). Once the cell is disassembled, researchers have utilized analytical techniques including time-of-flight secondary ion mass spectrometry (TOF-SIMS) [45], scanning electron microscopy (SEM) [21, 45], transmission electron microscopy (TEM) [46], X-ray photoelectron spectroscopy (XPS) [45, 47–51], X-ray absorption spectroscopy

(XAS) [49], atomic force microscopy (AFM) [50], Fourier transform infrared (FTIR) spectroscopy [48, 51], and Raman spectroscopy [52] to study the thickness, morphology, and composition of the SEI layer. Despite the numerous measurement techniques, additional research into the SEI layer is necessary, especially if a realistic SEI growth model is desired. The difficulty in SEI layer characterization is due to the fact that the SEI layer is fragile, readily reacts with the environment if it is not properly protected, and consists of a wide variety of organic and inorganic species.

SEI layer growth is typically modeled as a parasitic side reaction [54–56] where a TTF or time-to-capacity reduction is obtained as a function of reaction kinetics, mass transport, and cell geometry. An assumption is often made that the SEI layer is wholly responsible for the capacity and power fade, often neglecting concurrent failure mechanisms. While the SEI layer does not directly lead to catastrophic failure, it can decompose at elevated temperatures [23], and could contribute to a thermal runaway event by releasing gas. In this FMMEA, the formation and growth of the SEI layer is seen as a wearout failure that leads to a reduction in battery capacity and increased resistance.

If the battery is charged rapidly or at low temperatures, lithium metal can deposit on the surface of the negative electrode [65–30]. Over time, these deposits can develop into dendritic structures that may puncture the separator and initiate internal short circuits. This situation can lead directly to catastrophic failure and is often difficult to detect until a short circuit actually occurs. Several studies [30–36] have identified models for predicting lithium plating as a relationship between dendrite tip velocity and the applied current density and diffusion characteristics of

the lithium. Experimental validation of lithium growth in full electrochemical cells is difficult to observe, and the models are limited to predicting the growth of individual dendrites. Specialized cells with quartz glass windows have been developed to observe dendrite growth in-situ [35], but observation of lithium dendritic structures in commercial cells is not possible. NMR has been performed to detect metallic dendrites in lithium-ion cells [36]. Cell disassembly can also be performed, but the reactivity of the lithium dendrites complicates the process. Zier et al. suggested dyeing the electrode structure to elucidate the location of dendritic structures [37] by creating a greater contrast in electron microscopy images. If dendrite formation occurs, but causes an internal short circuit prior to disassembly, detection may be even more difficult. The lithium dendrites can vaporize due to surge currents, eliminating traces of their presence. Localized melting of the separator can indicate possible dendrite formation, but it could also be a result of local heating or metallic contamination. There are many opportunities to further develop models that predict not only the onset of lithium plating, but the time-to-failure under a number of operating conditions.

Electrode particle fracture can also occur if the battery is charged too quickly or if the electrode particle size distribution is not well designed. Typically, sub-micron-sized electrode particles have reduced internal intercalation-induced stresses, allowing the battery's life to be prolonged [57, 58]. Particle fracture can be observed as microcracks on the electrode particle surface as a result of crack initiation and propagation during repeated lithium intercalation and deintercalation. The exposed particle surface will then form a fresh SEI layer, which can be investigated with a

variety of analytical techniques described above. After the cell is disassembled, the electrode can be observed using SEM to locate fractured particles. Much work has been performed in optimizing the design of battery electrodes through an understanding of the stress generation during lithium-ion intercalation. Christensen and Newman [59, 60] developed the initial framework for the modeling of intercalation stresses, and other researchers have continued to expand their work for other materials and electrode geometries [57, 58, 61–63]. While modeling of particle stresses has helped in the design of battery electrodes to minimize mechanical stresses, the effect of particle fracture on the TTF of a lithium-ion battery has not been discussed in the literature. The role of particle fracture in capacity loss and power fade needs to be further elucidated to implement accurate lifetime prediction models based on a particle fracture failure mechanism.

Volumetric changes to the electrode structure can also lead to electronic disconnect in the battery, whereby parts of the electrode become unusable. The lithium intercalation reaction occurs when an electron and lithium ion combine in the graphite particles. Because the electrolyte is electronically insulated, a conductive network of particles is required to facilitate electron transport through the electrode structure. Volumetric changes associated with repeated intercalation can cause isolation of electrode particles, resulting in a reduction in usable capacity. This change in electrode structure can be observed by measuring the porosity and tortuosity of the electrode structure. This process is typically performed by milling away the electrode surface using focused ion beam (FIB) and measuring a cross-

section of the electrode using SEM [68] or employing high resolution X-Ray tomography [69].

Graphite experiences an approximate 10% volume change as lithium ions are inserted between its layered sheets as identified through X-Ray Diffraction [70, 71]. Initially the graphene sheets are in an alternating A-B pattern where adjacent layers are offset as seen in Figure 4. As an electric potential is applied, lithium ions begin inserting into the layers, and the graphene sheets rearrange into an A-A pattern. At various states of charge, lithium ions undergo a staging phenomenon, where they occupy every three layers, then every other layer, and finally, every layer. This is demonstrated in Figure 5. The inter-layer distance has been shown to increase from 3.355 Å to 3.700 Å as the concentration of lithium ions increases from 0% to 100%. Ohzuko et al. [26] measured the thickness change of a graphite pellet as lithium was intercalated into the layered structure and observed that on the first charge cycle, the expansion of the pellet was greater than 10%. While graphite is commonly used in most commercial applications, alternate negative electrode chemistries exhibiting a higher capacity include silicon and tin. One of the challenges associated with alternate chemistries such as silicon and tin are the large volume changes as a result of lithium intercalation. Silicon expands by approximately 400% when fully lithiated, which can cause fracture of the electrode particles and a quick decrease of the negative electrode's ability to store energy [72–74].

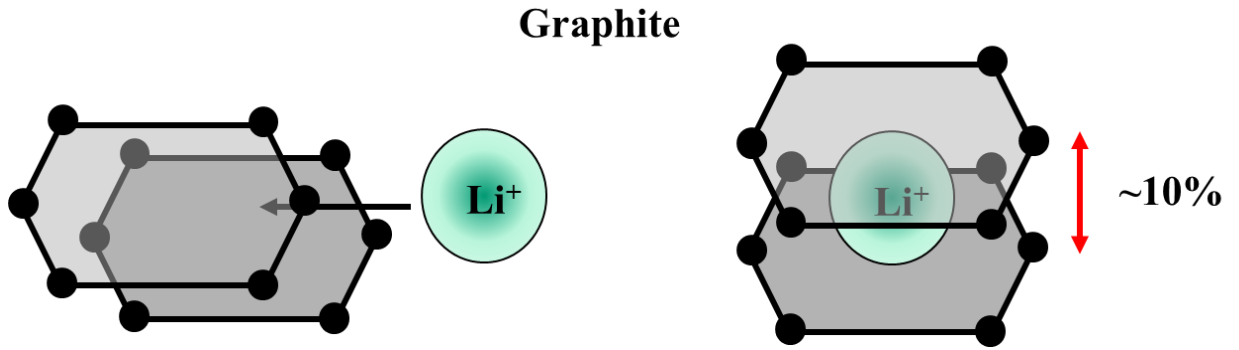


Figure 4: Lithium ion intercalation in graphite and corresponding volume change

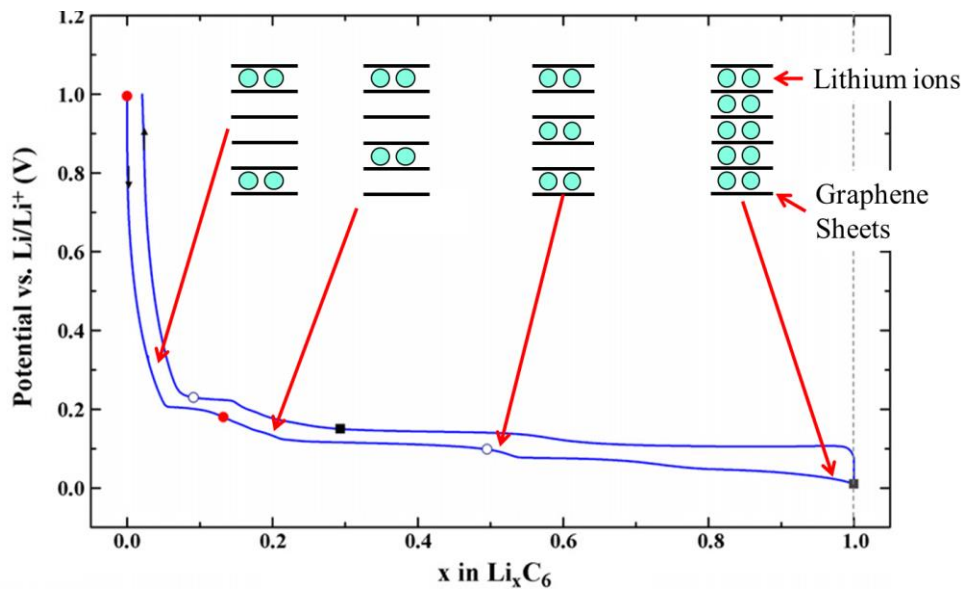


Figure 5: Lithium staging in graphite negative electrode. Modified from [70].

3.2 – Positive Electrode Active Material

The positive electrode usually consists of a mixed metal oxide, such as lithium cobalt oxide (LiCoO_2) or lithium manganese dioxide (LiMn_2O_4) [13]. Lithium iron phosphate (LiFePO_4) is another positive electrode material that is popular for high-rate applications [13, 75]. The positive electrode also operates on an insertion

principle, and mechanical stress and degradation can contribute to the fracture of particles and reduction in battery capacity as described for the negative electrode. Lithium cobalt oxide (LiCoO_2) expands as lithium ions are removed from its structure due to the repulsion of CoO_2 layers [76, 77]. The inter-layer distance increases from 96.7 Å to 98.5 Å when half of the lithium is removed from the electrode. As a result, lithium-ion batteries with both a graphitic negative electrode and a lithium cobalt oxide positive electrode experience a large volumetric expansion due to the concurrent expansion of graphite as lithium ions are inserted and the expansion of lithium cobalt oxide as lithium ions are removed. Variations of doped LiCoO_2 also exhibit this behavior [78]. Alternately, positive electrodes composed of lithium iron phosphate (LiFePO_4) contract by approximately 6.5% as lithium is removed, offsetting the concurrent expansion of the graphite as the battery is charged [75].

The positive electrode is affected by the growth of a CEI layer, but to a lesser extent than the graphite due to the high voltage (i.e., greater than 4.5 V) required to grow a stable film [83, 84]. The positive electrode is also susceptible to thermally driven decomposition, particularly if the cell is overcharged. Under overcharge conditions, the electrolyte becomes unstable [85], which leads to reactions between the electrolyte and positive electrode that can raise the cell's temperature and release oxygen gas [86]. Furthermore, mixed metal oxide positive electrodes have been shown to release oxygen when excess lithium is removed from their crystal structure [79–82]. If this process escalates, catastrophic failure is possible. Overcharging of the positive electrode structure can be observed by either measuring the gas species evolved via gas chromatography and mass spectrometry [86] or through diffraction-

based studies of the electrode structure [87]. However, no models have been developed that can predict gas evolution within the cell as a result of overcharge reactions.

3.3 – Current Collectors

The negative electrode active material is coated onto a copper current collector that is largely unaffected by the operation of the battery. However, the copper can dissolve if the battery is overdischarged [88, 89]. Copper dissolution can lead to the formation of different copper species and deposition on the electrode surfaces. If enough copper dissolves, the possibility of an internal short circuit becomes greater. While overdischarge can be largely avoided through proper battery management, it is still possible in the event of BMS failure, misuse of the battery, or self-discharge during long periods of storage. Copper dissolution will be described in much greater detail in Chapter 4; however, the relationship between the quantity of copper and the likelihood of short circuit has not been suitably quantified.

Alternately, the positive electrode active material is coated onto an aluminum current collector. If the cell is overcharged, the aluminum can corrode [90, 91]. This can lead to a reduction of power or increased resistance. While aluminum pitting corrosion is not a catastrophic failure, overcharge also causes electrode decomposition. The effect of metallic dissolution has not been modeled and related to a TTF.

3.4 – Separator

The separator in a lithium-ion battery is a porous polymer sheet that allows ion transport while preventing internal electrical short circuits between the electrodes. If the integrity of the separator is compromised, the electrodes can make contact, resulting in an internal short circuit that can cause heat generation and potentially lead to full thermal runaway [92]. Typically, electrode contact is due to thermal or mechanical damage to the separator. If metallic particles are present in the battery and puncture the separator, internal short-circuiting can occur. These particles can come from external contamination during assembly, lithium dendrite growth, and/or copper dissolution. Internal short-circuit failure mechanisms are observed as a negative electrode/positive electrode bridge by the particle accompanied by tearing of the separator. Thermal and mechanical damage to the separator can be observed through an SEM. Additionally, melted separator can be seen optically during a cell disassembly procedure and provide some insight into the initiation point of the failure. Researchers have begun investigating the stresses generated in the separator as a result of battery operation and abuse [93–95]. Excessive heating of the polymer past its melting point can result in an inoperable battery or in a catastrophic thermal runaway. As a safety mechanism, the pores of the separator are designed to close to prevent short-circuiting [92, 94]. However, if the battery continues to heat up, the separator could further melt and allow an internal short circuit [92, 94]. Finally, the separator is usually wider than the electrodes to prevent short-circuiting at the edges. However, separator shrinkage when exposed to electrolyte or high temperatures could cause the electrode edges to touch, possibly initiating a thermal runaway [92]. Proper design and selection of the separator can aid in preventing thermal runaway, but

proper manufacturing and screening procedures are required to prevent contaminated cells from entering the supply chain.

3.5 – Electrolyte

An organic solvent and a lithium salt make up the electrolyte of the battery. The electrolyte helps facilitate lithium-ion transport while inhibiting electron transport between the negative electrode and the positive electrode. The most commonly used solvents are organic-based carbonates, such as EC and DMC. The electrolyte can contribute to side reactions with the electrodes that reduce the available capacity of the battery and lead to wearout failure. While the electrolyte most commonly used in lithium-ion batteries has beneficial properties for ion transport, it is highly flammable and unstable outside of a narrow voltage and temperature window. If operated under extreme temperature or voltage conditions, the electrolyte can decompose, cause gas generation, and lead to thermal runaway [85]. Typically, electrolyte decomposition occurs at temperatures above 200 °C, at which point thermal runaway becomes likely. The electrolyte can be analyzed and compared to virgin electrolyte to identify the degradation and decomposition mechanisms occurring within the cell or the electrodes can be studied as previously described to observe decomposition products. Previous studies have utilized NMR [16], FTIR [17], thermogravimetric analysis (TGA) [18], differential scanning calorimetry (DSC) [19], and accelerated rate calorimetry (ARC) [20] to measure electrolyte properties and identify degradation and decomposition pathways for the popular lithium-ion battery solvents. Alternately, researchers have focused on heat

generation and heat dissipation rates [96–98] when modeling thermal abuse that would lead to electrolyte decomposition. Thermal abuse models evaluate the contributions of different sources of heat generation, including short circuits and chemical reactions, to identify a timeline for the initiation of thermal runaway. These models have applications in developing thermal management systems and anomaly detection; however, large-format batteries do not always have a uniform temperature distribution on the surface of the cell. By the time the rise in temperature is detected, it may be difficult to prevent thermal runaway. In addition to developing new methods to detect the internal temperature of the cell, it is important to focus on the root causes of temperature generation and develop models to predict the onset of an internal short circuit or dendrite growth.

3.6 – Cell Terminals and Casing

The cell terminals are responsible for conducting current from the current collectors to the external electric circuit. The terminals are typically connected to the current collectors by spot welding a tab onto the current collector. Poor-quality spot welds or an insufficient number of spot welds could lead to increased resistance to electrical current. Quality control issues with spot welding can be identified visually through optical microscopy, or mechanically through a pull or shear test. Additionally, thermo-mechanical fatigue can cause the connection between the cell terminals and the current collector to degrade and fail. Loss of connectivity or intermittent connectivity could cause the host device to malfunction or fail altogether. Moisture surrounding the terminals on the exterior of the battery can cause short-

circuiting of the cell through corrosion reactions or through formed conductive pathways. In the investigation surrounding the Chevy Volt fire in June 2011, the battery fire was traced back to coolant leakage following a side-impact crash test [99]. The coolant was electrically conductive at high voltages, causing an external short circuit between the battery's terminals. The short circuit generated enough heat for the batteries to undergo thermal runaway. Alternately, moisture can cause corrosion between the battery's terminals, resulting in a slow discharge of the battery or excessive heat generation, and can be modeled using a variety of well-developed models for electronics corrosion [100–103]. The battery can be left inoperable, or excessive heat generation could lead to thermal runaway. Therefore, it is important to not only protect the battery from moisture, but also to predict the risk of corrosion formation under a variety of operating conditions.

Another way that thermal runaway could be induced is through denting or crushing of the cell casing, which causes stress to be transferred to the electrodes and possibly results in a short circuit. Finite element modeling has been performed by [104, 105] to help develop better designed battery packs and predict the onset of catastrophic failure due to mechanical abuse. Simplified analytical models are needed for real-time assessment of mechanical damage to the cell. In the case of an EV accident, first responders need to know the risk of thermal runaway. A full-scale finite element model will not be appropriate for this type of control scenario, therefore, additional investigation into new ways to detect and model battery damage under mechanical loads is required.

3.7 – Summary

Performing an FMMEA is essential to understanding the many ways in which batteries can fail. Further analysis takes into account likelihood and severity of given failure mechanisms occurring to prioritize the most important mechanisms to focus on for a given application and use scenario. In this work, operation at high voltages (overcharge) and low voltages (overdischarge) is emphasized due to the variety of failure mechanisms that can be initiated, the likelihood in which the failure mechanisms can be exacerbated in battery pack applications, and the severity of failure.

Chapter 4: Overdischarge of lithium-ion batteries

4.1 – Literature Review

Overdischarge of lithium-ion batteries can fall into two categories:

Overdischarge to voltages as low as 0 V, or overdischarge to voltages less than 0 V, also referred to as reversal because the positive electrode's potential falls below the negative electrode's potential. Both types of overdischarge can negatively affect battery performance; however, their likelihood of occurrence differs. Overdischarge to 0 V is more likely to occur for batteries in storage at open circuit, whereas overdischarge into reversal requires an external load and is more likely to be handled by a battery management system. Overdischarge to 0 V can occur due to self-discharge of individual cells as well as parasitic BMS loads in battery packs.

M. Zhao et al. [106–109] conducted multiple studies to understand copper dissolution of both uncoated and coated copper foils in lithium-ion battery electrolytes. To assess the stability of bare copper foil in battery electrolytes, the researchers assembled a three-electrode cell with a working electrode consisting of a copper foil connected to a nickel wire, a reference electrode consisting of lithium metal connected to a nickel wire, and an auxiliary electrode of platinum wire for cyclic voltammetry and controlled-potential electrolysis experiments. When cyclic voltammetry scans were conducted at a variety of sweep rates, a sharp increase in current above 3.4 V vs. Li/Li⁺ was attributed to oxidation of copper, and a reduction peak around 3.4 V vs. Li/Li⁺ was seen on the reverse scan. When controlled-potential electrolysis was performed, the mass loss of the copper foil electrode was measured for a number of electrolysis potentials. At 3.5-3.6 V vs. Li/Li⁺, the electrode lost

approximately 4 – 8% of mass in 1.5 hours. A voltage of 3.4-3.6 V vs. Li/Li⁺ for copper is relevant to a full lithium-ion battery because it represents an overall cell voltage of approximately 0.3 – 0.5 V when paired with typical mixed metal oxide positive electrodes. In [106], the stability of copper foil in the electrolyte was studied by placing copper foils in sealed vials of electrolyte. The effect of impurities (H₂O and HF) in the electrolyte were studied and flame atomic absorption spectroscopy was utilized to quantify the amount of copper dissolved into solution. In fresh electrolyte, the concentration of copper plateaued at approximately 50ppm after 14 weeks. Using cyclic voltammetry, it was determined that the copper was in a Cu²⁺ state in the electrolyte solution. Furthermore, the total amount of copper that was dissolved was independent of the volume of the electrolyte solutions. Electrolyte impurities can enhance copper dissolution initially due to oxidation of the copper by impurities. When the copper foil was coated with graphite, some suppression of the copper dissolution was observed in [108–109]. In [108], a three-electrode beaker cell was used with a graphite coated copper working electrode, lithium-metal reference electrode, and a platinum auxiliary electrode to conduct cyclic voltammetry and bulk electrolysis experiments, similarly to the bare copper foil in [106]. An oxidation peak did not appear until a voltage of approximately 3.65 V vs. Li/Li⁺ was reached, which corresponds to an approximate 50 mV positive shift compared to the bare copper foil. In the bulk electrolysis experiments, initially a lower current indicated that copper dissolution was inhibited; however, sudden increases in the oxidation current corresponded with delamination of the electrode from the copper current collector. Once the electrode exposed the copper foil, significant amounts of copper dissolution

were observed. In [109], graphite-coated copper foils were stored in an electrolyte for over 14 weeks and copper concentration was measured using flame atomic absorption spectroscopy. The presence of the graphite coating significantly reduced the amount of copper dissolved, with copper measurements approximately 1ppm after 14 weeks compared to 50ppm for bare copper.

In [110], failure of repeatedly overdischarged cells into full reversal was observed. The cells were either repeatedly discharged by an additional 10% or 20%, which corresponded to a cell voltage below 0 V. Micro shorts were observed in the cells which were unable to be charged after 1 cycle (-20% SOC) and 10 cycles (-10% SOC). The cells were disassembled in a glovebox and studied using SEM/EDX. Even for a cell cycled between 0% and 100% SOC, aluminum was detected on the electrodes, suggesting that the separator was coated with alumina for safety purposes. Further study of the separators via X-ray diffraction (XRD) confirmed that aluminum was embedded in the separator from the start, and that overdischarge led to the formation of metallic aluminum and short circuit. This suggests that additional failure mechanisms besides copper dissolution could emerge as new additives are included in separators to improve the safety performance. It is also unclear whether dissolved copper contributed to this failure mechanism.

The interaction between the positive electrode and negative electrode during overdischarge and overcharge was elucidated by Kasnatscheew et al.[111] when a cell was overdischarged into reversal (cell voltage less than 0 V). A 3-electrode cell was constructed using nickel manganese cobalt dioxide ($\text{Ni}_{0.33}\text{Mn}_{0.33}\text{Co}_{0.33}\text{O}_2$ or NMC111) for the positive electrode, graphite for the negative electrode, and lithium

metal as the reference electrode. When overdischarging at a constant current, oxidation was observed on the negative electrode, suggesting copper dissolution. After about an hour of copper dissolution, a change in slope of the positive electrode was observed that was attributed to reduction of copper ions on the surface of the positive electrode to form metallic copper. The presence of copper on the positive electrode was confirmed with SEM/EDX.

Fear et al. [112] used commercial 18650 cells to study overdischarge into reversal (-100% SOC). Cells were overdischarged at a constant current until the cell was at -100% SOC and disassembled. Furthermore, half-cells were constructed with harvested electrodes, lithium nickel cobalt aluminum dioxide (NCA) positive electrode and graphite negative electrode. SEM and EDX analysis were employed to confirm the presence of copper on both electrodes and results from the half-cell studies were used to propose mechanisms for the copper dissolution and plating. The overdischarge procedure was split into 4 stages, during which SEI decomposition, oxidation of the copper current collector, reduction of the copper ions on the positive electrode, and continuous dissolution of copper from the current collector occur, respectively. When cells were disassembled, copper dissolution was evident due to poor adhesion of the negative electrode to the current collector. The presence of copper on the positive electrode was observed via SEM/EDX, and plating of copper was supported by adhesion of the separator to the positive electrode surface. The authors determined that a short circuit was present, and that overdischarge in and of itself will not necessarily cause thermal runaway; however, safety concerns could arise when an overdischarged cell is recharged.

The authors in [113] performed overdischarge testing on commercial 18650 lithium iron phosphate (LiFePO₄)/graphite cells. The cells were opened and a reference electrode was inserted into the electrode winding before immersing the entire assembly in electrolyte in a beaker. Cells were then overdischarged to various levels (-5%, -10%, -15%, and -20% SOC) and the potential of each electrode with respect to the lithium metal was measured. Furthermore, cyclic voltammetry measurements of pure copper electrodes in a matching electrolyte solution were performed to identify the oxidation and reduction potentials required for copper dissolution. The oxidation currents were 3.92 V vs Li/Li⁺ to oxidize the bare copper from Cu to Cu⁺ and 4.17 V vs Li/Li⁺ to further oxidize to Cu²⁺. Reduction occurred at 3.28 V and 3.19 V vs. Li/Li⁺ for reduction of Cu²⁺ to Cu⁺ and Cu, respectively. These values are different than reported elsewhere [106, 108]; however, differences in electrolyte and ambient conditions could play a role in these limits. Furthermore, the experiments used to characterize these limits were different and oxidation could occur closer to the 3.1-3.6 V vs. Li/Li⁺ limit previously reported by others. The authors used SEM/EDX to confirm the presence of copper on the electrodes and separator. Failure in the full cells was attributed to internal short circuiting due to copper dendrites.

In Guo et al. [114], overdischarge into full reversal is conducted, whereby the cell is discharged below 0 volts. This scenario can arise when multiple cells are connected together in series and discharge of the whole string results in one or more cells being overdischarged. In this study, the researchers overdischarged a cell to -100% SOC and noted three distinct phases in the voltage response. In phase 1, the cell is discharged to -11% SOC, which occurred around -2.19 V for their cell. From -

11% to -20% SOC, the cell is in phase 2, during which, the cell voltage slightly increases to -1 V. Stage 3 consists of the remaining overdischarge to -100% SOC. The authors noted a slight plateau of the voltage curve in stage 1 near 1 V, which is attributed to SEI layer breakdown. When testing was terminated during this stage, they demonstrated recoverable capacity and no discernable changes in performance. In stage 2, results were more variable because of the formation of a mild internal short circuit, whereas in stage 3, the cells could not be recovered due to severe internal short circuiting. SEM and XRD were conducted to examine the electrode morphology and the structural characteristics of the internal short circuit. As the cell was overdischarged from 0% to -13% to -20%, peaks associated with Cu became more pronounced with increasing levels of overdischarge. The growth of XRD peaks associated with Cu as the cell was overdischarged from 0% SOC to -20% SOC grew in intensity suggesting that copper dissolution and deposition is a continuous process during overdischarge into voltage reversal.

H. Maleki and J. Howard [115] demonstrated copper dissolution in lithium-ion cells by discharging the cells to either 2.0, 1.5, 1.0, 0.5 or 0 V and holding for 72 hours. The cells were then recharged and cycled 5 times before repeating the overdischarge and 72 hour voltage hold procedure again. The authors found that 2.0 and 1.5 V overdischarge had minimal effect on cycle-life, 0.5 and 1.0 V overdischarge had significant capacity loss, and 0 V overdischarge was extremely erratic. Some 0 V cells cycled but quickly lost capacity, while others immediately experienced an internal short circuit. EDX analysis performed on both sides of the separator of one of the 0 V cells showed clear migration of copper ions through the

separator, with a higher concentration on the negative electrode side than the positive electrode side; however, 2 of the other 0 V cells did not exhibit copper dissolution.

Crompton and Landi [116] investigated copper dissolution thresholds in 3-electrode pouch cells and explored pre-lithiation strategies for 0 V storage of lithium-ion batteries. Storing a battery at 0 V without copper dissolution would be advantageous for a number of situations including shipping and long term storage; however, changes to cell chemistry or manufacturing and processing are required. The 3-electrode pouch cell used in this study consisted of a mesocarbon microbead (MSMB) graphite negative electrode, a lithium cobalt dioxide (LiCoO_2) positive electrode, and a lithium metal reference electrode. The reference electrode enabled the measurement of negative electrode and positive electrode potential independently with respect to Li/Li^+ . A fixed resistance of 2.5 k Ω was applied to the cell once it was at 0% SOC (full cell voltage of 3 V) and held for 3 days. The negative electrode's potential with respect to lithium metal increased rapidly to above 3.1 V vs. Li/Li^+ after 10 hours. Direct measurement of the dissolved copper was not conducted in the study, but a linear sweep voltammogram was conducted to identify the negative electrode potential with respect to lithium metal that resulted in an oxidative current. The authors found that an negative electrode potential of 3.1 V vs. Li/Li^+ resulted in a small oxidative current, with higher voltages leading to increased currents. While this value is lower than the 3.4-3.6 V vs. Li/Li^+ reported elsewhere [106, 108], the authors attributed this to ambient conditions, electrolyte composition, and non-faradaic processes. A more conservative threshold of 3.1 V may be ideal for applications requiring high levels of safety.

Fuentevilla et al. [117, 118] presented X-ray photoelectron spectroscopy results from large-format (>30 Ah) cylindrical cells experiencing overdischarge. Some of the cells had naturally overdischarged to voltages less than 1 V, whereas some of the cells remained at a healthy voltage above 3 V. The cells were disassembled in a glovebox with <1 ppm O₂ and samples were collected from multiple locations of the negative electrode and positive electrode. The samples were mounted onto a platen and transferred to a Physical Electronics 5400 X-ray photoelectron spectrometer in an air-tight transfer vessel. The samples were never exposed to air during the process. Survey and multiplex scans were conducted, and copper was detected on both electrodes from cells that were stored at less than 0.5 V, whereas no copper was observed on cells 0.5 V and above. This is consistent with literature, although the exact dissolution threshold is dependent on a number of factors including the positive electrode to negative electrode active material ratio.

Li et al. [119] overdischarged LiCoO₂ cells to voltages between 0 and 3 V and studied copper deposition on the positive electrode using inductively coupled plasma (ICP) analysis. Furthermore, the thickness of the cells and the gas composition was studied. Overdischarge to 0 V led to the generation of gases, most notably CO₂, and the performance was significantly affected. ICP analysis showed that more than 4 times the amount of copper was found in 0 V cells compared to cells discharged to 0.4 and 1 V. For this particular cell, a 3-electrode test using a lithium metal reference electrode showed that a full cell voltage of approximately 0.2 – 0.3 V would result in copper dissolution.

In K. Kumai et al. [120], gas generation as a result of repeated overdischarge was observed. The overdischarge was performed by cycling the batteries with a lower voltage limit shifted by 10% of the nominal cell capacity. A significant amount of gas was generated, primarily composed of CO₂ and CH₄. The authors hypothesized that the copper current collector had dissolved and plated the positive electrode. Accelerated electrolyte decomposition took place due to inhibited intercalation, and as a result produced hydrocarbons, CO₂, and CO. Direct measurement of the copper dissolution was not conducted and the actual lower voltage of the cell was not provided.

Love and Gaskins [121] overdischarged pouch cells with a LiCoO₂ positive electrode and graphite negative electrode. Their report primarily focuses on swelling due to gas generation and reduction in charge/discharge cycles. When a cell was repeatedly overdischarged to 1.2 V, the thickness increased by over 3.5 mm after 200 cycles. Furthermore the cells reached 20% capacity loss within 57 cycles, which is at least 4 times less than the same cells operated in their normal cycling range. Copper analysis was not performed, and may not have occurred based on the voltage ranges tested. Instead, SEI layer decomposition, reformation, and gas generation may have consumed lithium, resulting in a reduced cell capacity.

4.2 – Research Gaps

Much of the research into copper dissolution can be separated by the type of overdischarge scenario employed, notably, overdischarge into reversal and overdischarge to voltages greater than 0 V. Overdischarge into reversal is primarily a

concern with large battery packs containing many cells in parallel and series configurations. If cells become imbalanced in a series string, one or more cells could experience reversal while the overall string voltage still appears to be healthy. Alternatively, overdischarge to voltages greater than 0 V represents storage scenarios in which the cell or battery self-discharges to a voltage below the manufacturer's recommended voltage cutoff, but does not enter into reversal. The former has been shown to lead to copper plating on the positive electrode as the cell is forced and held in reversal. Eventually a copper dendrite grows and initiates a hard short circuit and the cell can no longer be used. For cells overdischarged without reversal, the failure mechanism needs to be further elucidated. The dissolution of copper can occur at low cell voltages (~0.5 Volts and below); however, the cell can usually be recovered and subsequently cycled. The ability to recover a cell overdischarged to extremely low voltages is advantageous, especially for large, expensive battery packs. However, the safety and performance implications are not well known. The experiments described in this section provide additional information on the nature of copper dissolution under overdischarge scenarios that do not result in voltage reversal.

4.3 – Experimental

The cells used in this study are large-format cylindrical lithium-ion cells with a nominal capacity of 52 Ampere-hours (Ah) at a C/5 rate (10.4 A). The cells are 208 mm long and 54 mm diameter and weigh 1 kg. The cells have a carbon-based negative electrode and a nickel cobalt aluminum (NCA) oxide positive electrode and are operated between 2.5 V and 4.1 V. A picture of the cell can be seen in Figure 6. The cells were obtained from battery packs containing 9 cells connected in series with

the majority of the cells (>75%) exhibiting voltages within the cell's operating limits. The remainder of the cells experienced some level of overdischarge and exhibited voltages from 0 to 2.5 V. The packs had been in storage, suggesting that the battery management system and internal cell impedance caused the cells to discharge to varying levels. Cells with voltages above 2.5 V were cycled using a Maccor programmable battery tester at a C/5 rate (10.4 Amps) and exhibited capacities matching the nominal capacity of 52 Ah. These cells are considered healthy and are used as a baseline comparison. Thirty (30) of the healthy cells were selected for an overdischarge study, and the remaining healthy cells were used for cell disassemblies, overcharge testing, and high temperature exposure testing.



Figure 6: Large format cylindrical cell with positive and negative terminals on top.

4.3.1 – Overdischarge procedure

Cells selected for the overdischarge study were separated into 3 groups of 10 cells each. The first group was overdischarged to 0 V, the next group was

overdischarged to 0.25 V, and the final group was overdischarged to 0.5 V. Control samples were chosen from the cells exhibiting voltages within the range of 2.5 V to 4.1 V. The study is summarized in the diagram shown in Figure 7.

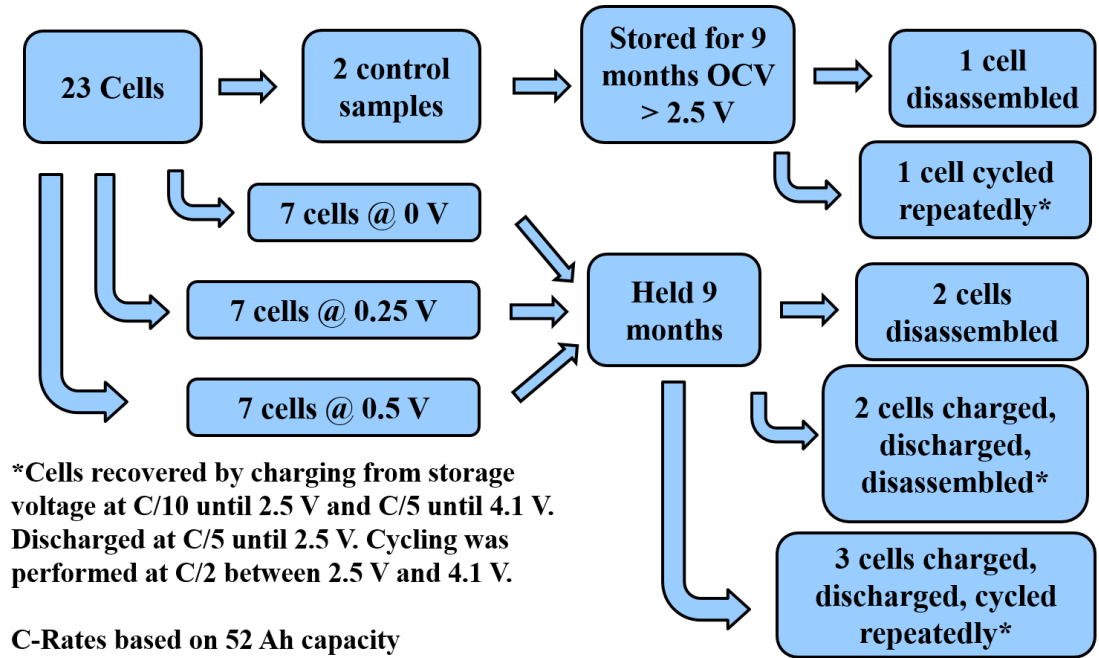


Figure 7: Overview of overdischarge study

To perform the overdischarge, each of the cells' voltage was first reduced to 0.5 V at a current of 5.2 A (C-Rate of C/10) using a Maccor programmable battery tester. The cells were then connected to a separate circuit used to individually maintain their voltage to within approximately 10 mV. For 0 V cells, the cells were simply shorted through a resistive load of 1 Ohm. All cells were tested in a room with ambient temperature of approximately 25°C and held in the various overdischarged states for 9 months. Following storage, the cells were either disassembled in the overdischarged state, recharged and then disassembled, or repeatedly cycled prior to disassembly.

To recharge the cells, the cells were charged at a C/10 rate (5.2 A) until the cell's voltage reached 2.5 V. The charging current was then increased to a C/5 rate (10.4 A) until the cell reached 4.1 V. The cell was charged at a constant voltage of 4.1 V until the current reduced to 250 mA. The cell was discharged to 2.5 V at a C/5 rate (10.4 A) until the cell reached 2.5 V.

To cycle the cells following overdischarge, the recharge procedure is conducted as described above, except the upper voltage limit is set to 3.6 V, representing approximately 50% SOC. An impedance scan is taken using a 200 mA AC perturbation current with a measurement frequency range of 10 mHz to 10 kHz. As long as the impedance has not significantly changed, cycling is conducted at a C/2 rate (26 A) between 2.5 V and 4.1 V. Every 10 cycles, the cell is stopped and monitored for self-discharge, recharged to 3.6 V, and another impedance scan is taken. This is to ensure that any potential safety concerns are detected in advance. Cycling is continued to demonstrate the effect of overdischarge on capacity fade and cell impedance.

4.3.2 – Cell disassembly procedure

Destructive physical analyses (DPA) along with Computed Tomography (CT) scans provided information about the internal structure of the cells. A CT scan of the cell can be seen in Figure 8 showing the wound jelly-roll with current collector extending from the bottom of the jelly-roll to make contact with the cell casing and another current collector from the top of the jelly-roll that was attached to a bus bar that connected to one of the terminals at the top of the cell. The cell was case-positive, indicating that the current collector attached directly to the case was the

positive electrode's aluminum foil, and the current collector attached to the terminal at the top of the cell was the negative electrode's copper foil.

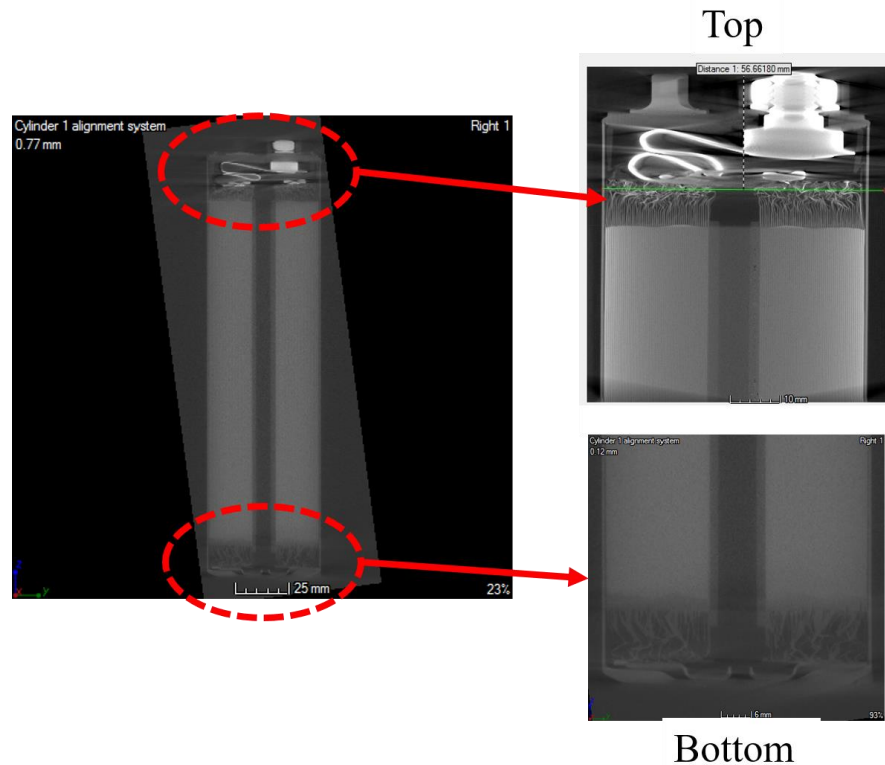


Figure 8: CT scan of cell showing top current collector and connection to terminal via busbar and bottom current collector connected directly to casing

Preliminary cell disassembly procedures were conducted on cells that had naturally overdischarged to 0 V. This allowed for the confirmation of safe-to-cut zones and provided practice to determine the amount of pressure to apply with the cutting tool. The cutting tool was a Dremel rotary tool with a non-conductive circular blade. The cells are marked $\frac{1}{4}$ " from both the top and bottom to ensure that the rotary tool does not cut into the jelly-roll structure and inadvertently short circuit adjacent layers. A thermocouple mounted to the side of the battery monitors the external cell temperature and cell disassembly is stopped if the temperature begins rising

unexpectedly. Cells are transferred into a glovebox filled with Argon gas prior to disassembly. The glovebox is maintained at $< 1\text{ ppm O}_2$ to preserve sample integrity. The cell undergoing disassembly is held above a large bell jar filled with Drierite with one hand while using the rotary tool to first cut into the bottom of the cell below the marked line. The cell is rotated to cut around the entire circumference of the cell and the bottom end cap is pulled off to expose the aluminum current collector. The cutting process is repeated at the top of the cell and the top end cap is pulled off to expose the copper current collector. The cell is placed in the bell jar and vacuum is pulled for 24 hours to remove excess electrolyte from the jelly-roll. After the 24 hour stand-down, the bell jar is opened in the glovebox and the rotary tool is used to carefully score a line down the length of the cell. During this stage of the disassembly, extra care is taken to avoid cutting directly through the cell casing and into the jelly-roll. Once the score mark is made, the rotary tool is used to slowly cut deeper into the cell casing. Periodically, a non-conductive tool will be used to try to break the cell casing along the cut line starting from the top of the cell and working towards the bottom of the cell. The cell casing can then be peeled away and the jelly-roll extracted.

The jelly-roll is then prepared for sample collection by removing the tape used to keep the jelly-roll wound and mounting the jelly-roll onto a glass rod suspended with angle brackets as seen in Figure 9. The separator is peeled away until the beginning of the electrode winding is reached. The two electrodes are separated and taped to cylinders on either side of the jelly-roll. The two electrode rollers are connected together and rotated simultaneously to wind the individual electrodes separately on their own roller as seen in Figure 10.



Figure 9: Jelly-roll with glass rod through center mandrel and elevated over cutting board end view (left) and top view (right)



Figure 10: Negative electrode and positive electrode separated and wound onto separate rollers. The negative electrode is on the left and the positive electrode on the right.

The jelly-roll is unwound until a sample is collected for further analysis. In this instance, samples were collected from the outermost portion of the jelly-roll (exterior), the innermost portion of the jelly-roll (interior) and halfway between the two (middle). Samples were collected for scanning electron microscopy (SEM), X-ray photoelectron spectroscopy (XPS), and X-ray absorption fine structure (XAFS)

analysis. For SEM and XPS, two roughly ½” diameter circles were punched from the electrode sheet away from the edges. For XAFS, a large, approximately 2”x2” square of electrode was cut nearby to the punched samples. The electrode sheets with the punched samples can be seen in Figure 11. After removing the samples from the electrode sheets, the jelly-roll is unwound further until the center mandrel is reached. All samples are placed into clamshell cases and remained in the glovebox until it was time to conduct additional measurements.



Figure 11: Samples removed from electrode sheets

4.3.3 – Scanning Electron Microscopy

Scanning electron microscopy (SEM) analysis was performed on a Hitachi SU6600 located at the Naval Surface Warfare Center Carderock Division (NSWCCD). The equipment utilizes a ZrO/W schottky emission electron gun with a resolution of 1.2 nm at 30 kV with a working distance of 5 mm or a resolution of 3.0 nm at 1kV with a working distance of 4 mm. Samples were mounted onto the SEM stage with conductive tape and introduced into the SEM through a vacuum port. The

focus was adjusted and SEM micrographs were taken at multiple magnification states to observe the morphology of the electrodes.

4.3.4 – X-ray Photoelectron Spectroscopy

X-ray photoelectron spectroscopy was conducted on a Physical Electronics VersaProbeII Scanning X-ray Photoelectron Spectroscopy Microprobe located at the Naval Surface Warfare Center Carderock Division (NSWCCD). The VersaProbe is equipped with a monochromatic Al-K α X-ray source that can provide a narrow, focused beam for sample analysis with spatial resolution near 10 microns. The monochromatic Al-K α radiation is achieved through the use of a diffracting quartz monochromator to focus the X-rays and eliminate the broad range of Bremsstrahlung X-rays (1-12 keV) that can hit the sample when a non-monochromatic source is used. The use of a monochromatic X-ray source allows for improved interpretation of XPS peaks due to a better resolution and lower background counts associated with unfiltered X-rays. XPS is a surface sensitive technique and the depth of interaction is typically around 5 nm.

Samples are transferred into the XPS ultrahigh vacuum chamber through an intro chamber that is pumped down to 4×10^{-4} Pa. The intro chamber allows for the introduction of air-sensitive samples through an additional transfer vessel. For all of the electrodes studied, this transfer vessel method was employed. The sample platen is prepared by placing double-sided tape on the top of the platen. A portion of the ½” diameter sample is cut (~1/4 of the sample) and adhered to the tape on the platen surface. Approximately 3-4 samples are placed on the platen in this manner to

increase the throughput of samples. The platen is loaded into the transfer vessel inside of a glovebox and the transfer vessel is closed to prevent contamination with air. The transfer vessel can then be removed from the glovebox and placed on the XPS intro chamber and pumped while the sample is still sealed within. Once the vacuum level reaches 4×10^{-4} Pa, the transfer vessel is opened to continue pumping down the sample without ever exposing it to air. The sample platen is loaded onto a magnetic fork and the valve between the intro chamber and the analysis chamber is opened to move the sample platen onto the analysis stage. The magnetic fork is retracted and the valve closes again and the analysis chamber is able to achieve its ultrahigh vacuum of $\sim 2 \times 10^{-8}$ Pa again.

A picture of the sample platen is captured to identify analysis regions and associate the analysis locations with X and Y coordinates. A z-alignment procedure maximizes the signal intensity by varying the sample height. XPS data collection can commence when the ultrahigh vacuum analysis chamber reaches $\sim 2 \times 10^{-7}$ Pa and all of the analysis locations are selected z-aligned. Survey and multiplex scans were performed on all of the samples to identify regions of interest and provide well resolved XPS spectra of regions of interest. Survey scans were taken across the full range of X-ray energies (0 eV to 1486.7 eV) with a pass energy of 117.4 eV, providing a resolution of 1.76 eV. A series of 5 cycles were performed and averaged together to maximize the signal to noise ratio and resolve the XPS peaks. Two different types of multiplex scans were conducted for each of the samples. A quick multiplex scan focused exclusively on C1s, O1s, and F1s orbitals and was conducted prior to and following a longer multiplex scan. The two quick multiplex scans will

show whether the long multiplex scan introduces any X-ray damage to the samples. The long multiplex scans of the negative electrodes focus on Li1s, C1s, O1s, F1s, P2p, and Cu2p3 orbitals, and the positive electrode scans additionally include Co2p and Ni2p orbitals. Scans are taken over a 200 μm x 1000 μm area with an electron take-off angle of 45°. The X-ray source operated at 15 kV and a power of 50 W producing a 200-micron beam, which is electronically rastered to minimize X-ray damage of the samples. The analyzer pass energy was set 23.5 eV for multiplex spectra, which enabled a finer resolution of 0.35 eV.

A low energy Argon ion beam and an electron beam are concurrently used to strike the analysis area during XPS analysis to reduce surface charging that can complicate interpretation of the collected spectra. This is particularly useful for lithium-ion batteries with composite electrodes consisting of both metallic and insulating materials that can differentially charge. Final calibration of the spectra was made by assigning the binding energy of the hydrocarbon signal to 284.8 eV. XPS spectra are obtained by striking the sample with incident X-rays and measuring the kinetic energy of the ejected electrons. The binding energy, BE, can then be calculated based upon the following equation:

$$\text{BE} = h\nu - \frac{1}{2}mv^2 - \phi$$

Where h is Planck's constant, ν is the X-ray frequency, m is the mass of the ejected electron, v is the velocity, and ϕ is the work function associated with the spectrometer. The work function is a known quantity through calibration of standards on a given piece of XPS equipment. The energy associated with the incident X-rays is known, and the kinetic energy is measured with a hemispherical analyzer. Thus, it is

possible to plot the binding energy vs. the intensity of the ejected photoelectrons (given as counts/second). Peaks in the spectra are associated with different element orbitals and provides information about the nature of the chemical bonds present in the sample. Additional analysis can be performed by fitting Gaussian or non-Gaussian curves to the peaks to identify the location and the full-width at half maximum (FWHM) of the peak for identifying compounds in an unknown sample through comparison with known standards.

Battery electrode samples were studied for three collected locations (exterior, middle, and interior) for cells overdischarged to 0 V, 0.25 V, and 0.5 V. Samples collected from a healthy cell discharged to 2.5 V were also measured as a control sample. In addition to analyzing the battery electrodes, reference samples were studied using the XPS to aid in the analysis of the negative electrode and positive electrode samples. Powders for CuF_2 , Cu_2O , CuO , $\text{Cu}(\text{OH})_2$, carbon black, polyvinylidene fluoride, NCA, and graphite were mounted on platens with double-sided tape. Most samples did not require special preparation, however, $\text{Cu}(\text{OH})_2$ is extremely sensitive to moisture. $\text{Cu}(\text{OH})_2$ powder was ground in a mortar and pestle inside of a glovebox and transferred to the XPS analysis chamber with the aid of the air-tight transfer vessel.

4.3.5 – X-ray Absorption Fine Structure

X-ray absorption fine structure (XAFS) measurements were conducted at Argonne National Laboratory's Advanced Photon Source (APS). The APS is a synchrotron radiation facility that consists of a linear accelerator, a booster synchrotron, and a storage ring. The linear accelerator accelerates electrons to

relativistic speeds at an energy of 450 MeV. The booster synchrotron further increases the energy of the electrons to 7 GeV in less than a second, at which point they are injected into an 1100 m circumference storage ring where they can be used for experiments in either insertion device or bending magnet beamlines. Beamline 5-BM-D uses bending magnets to direct X-rays at the samples located within the beam's path. Beamline 5-BM-D was operated under a general user proposal submitted for studying copper dissolution in lithium-ion batteries. XAFS is a bulk sensitive technique and complements the XPS analysis nicely to provide an overall picture of the surface and bulk chemistry. A plan view of the APS is given in Figure 12 and a schematic of the measurement setup is shown in Figure 13.

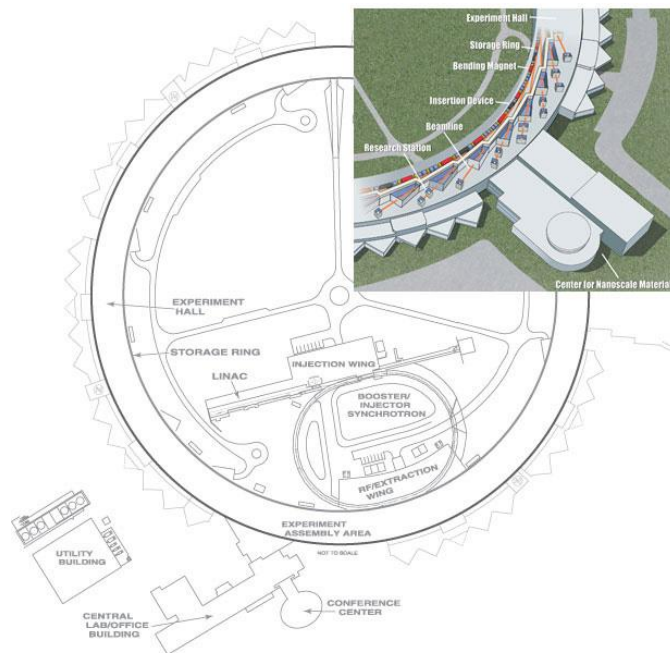


Figure 12: Plan view of the APS facilities showing the linear accelerator (LINAC), the booster/injector synchrotron, and the main storage ring [122]

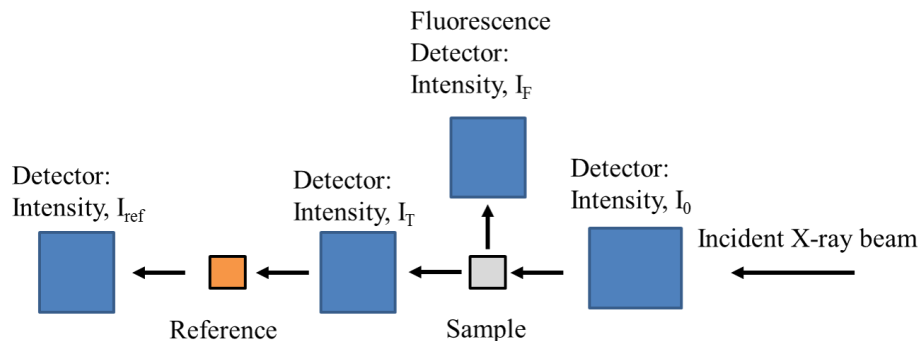


Figure 13: Schematic of 5-BM-D XAFS setup. The incident X-ray beam passes through a detector measuring the initial intensity of the X-rays. The X-rays strike the sample and a fraction pass through to be measured at the transmission detector. The remaining X-rays pass through a reference foil before their intensity is measured again. A fluorescence detector placed perpendicular to the transmission detectors can measure fluoresced X-rays.

X-ray absorption spectra can be measured in three different ways:

transmission, fluorescence, and electron yield. The transmission mode was used to collect the absorption at the Ni and Co K-edges of the positive electrode active material (NCA) by taking the natural logarithm of the ratio of incident X-rays, I_0 , and transmitted X-rays, I_T . The incident and transmitted intensities were measured using ionization chambers filled with appropriate mixture of Ar and N_2 gases. The fluorescence mode was used to calculate the absorption of dissolved copper present in the negative electrode by taking the ratio of the fluoresced X-rays, I_F , and the incident X-rays, I_0 . The fluorescence signal was measured using a Passivated implanted planar silicon (PIPS) detector manufactured by Canberra. The electron yield mode, which calculates the absorption by taking the ratio of measured total electron current ejected from the sample surface and the incident X-ray intensity, I_0 was not used in this investigation. The use of a reference foil and a third X-ray detector (ionization chamber) enables energy calibration of the spectra from multiple samples for comparison purposes. To investigate the chemistry of dissolved copper in the

negative electrode, a Cu foil was utilized for the monochromator energy calibration. To study the effect of overdischarge on the positive electrode active material (LiNiCoAlO₂), two separate measurements at the Ni and Co K-edges were taken with Ni and Co foils used for monochromator calibration, respectively. The X-ray cross section was approximately 1mm x 7mm, and samples were cut in excess of this cross section. For samples overdischarged to 0 or 0.25 V, flakes of graphite easily separated from the underlying current collector as seen in the disassembly picture in Figure 14. This delamination was attributed to reduced adhesion between the electrode and the current collector and allows for XAFS measurements of copper without contributions from the copper current collector itself. For other samples, a piece of Scotch tape was used to peel the electrode off of the current collector. This is illustrated in .Samples were mounted onto a plastic tray and placed in the line with the detectors either at a 90° or 45° angle for transmission and fluorescence measurements, respectively. Figure 16 shows multiple graphite flakes mounted onto a tray that is controlled by motors. The sample is centered with respect to the X-ray beam by scanning the sample to locate the maximum (fluorescence) or minimum (transmission) signal. The analysis locations are saved in a queue for multiple samples, which allowed unattended XAFS data collection under computer control.



Figure 14: Delamination of negative electrode from copper current collector.

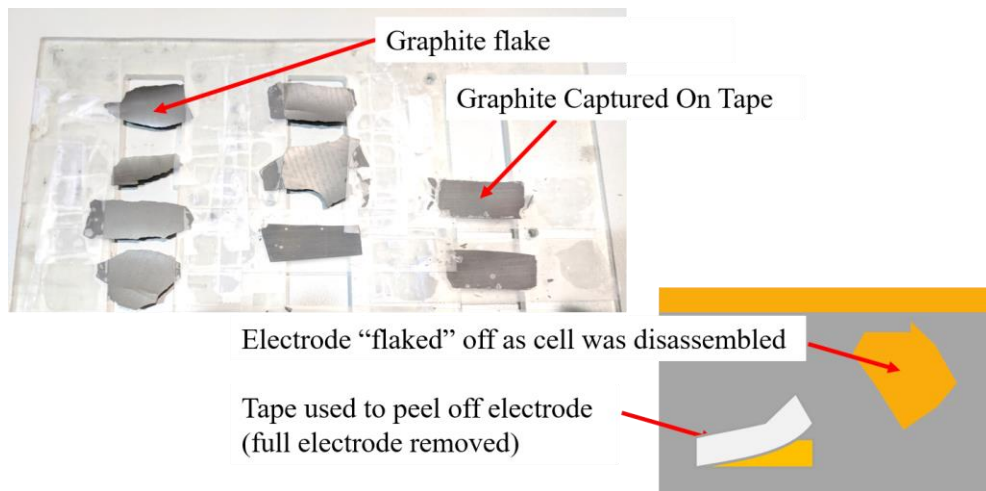


Figure 15: Image of graphite flake and graphite samples captured on tape

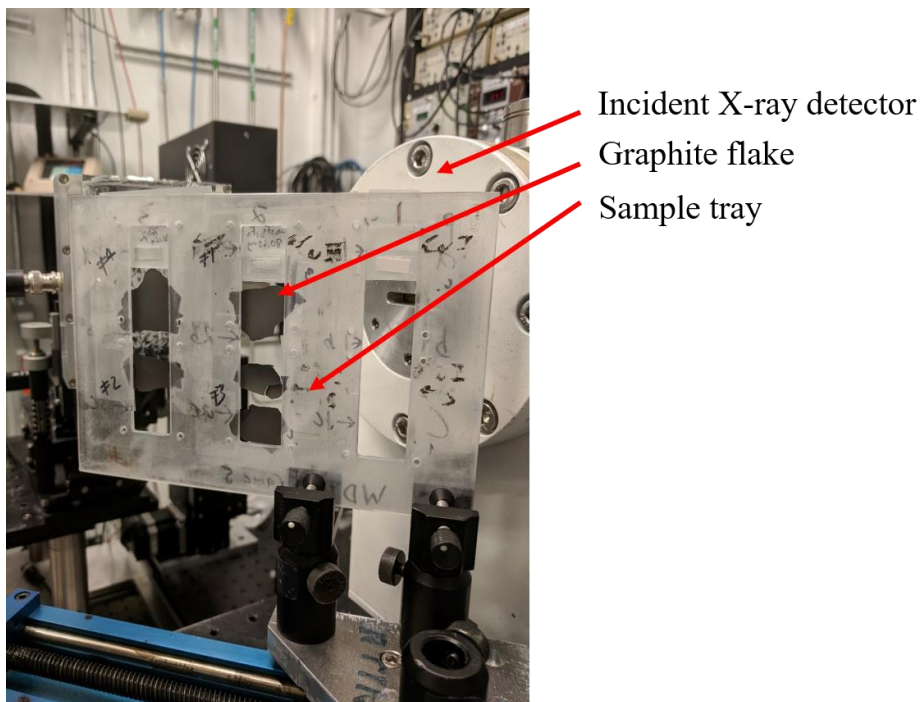


Figure 16: X-ray sample holder mounted on motorized stage. Flakes of graphite from the negative electrode are taped to the holder and positioned in the X-ray path for XAFS measurements.

XAFS measurements rely on the interaction of the incident X-rays with the sample. This is achieved by varying the energy of the incoming X-ray to locate the K-edge of the element under study. In the case of Cu, the K-edge is located at approximately 8979 eV, and it represents the point where the incoming X-rays have sufficient energy to eject inner s-shell electrons from copper atoms. Below the K-edge, no excitation occurs and the plot of absorption vs. X-ray energy is flat. Once the X-ray energy reaches the K-edge and above, a sharp jump in absorption is observed, known as the K-edge step. The probability of X-rays ejecting s-shell electrons has increased and manifests as increased absorption. As the incoming X-ray energy is increased further above the K-edge energy, oscillations in the absorption can be seen in Figure 17. This is due to constructive and destructive interference between scattering of the emitted photoelectrons by nearby atoms in the sample. The range of

energies in close proximity to the K-edge jump are termed the X-ray Absorption Near Edge Structure (XANES) and the energies above the K-edge are the Extended X-ray Absorption Fine Structure (EXAFS).

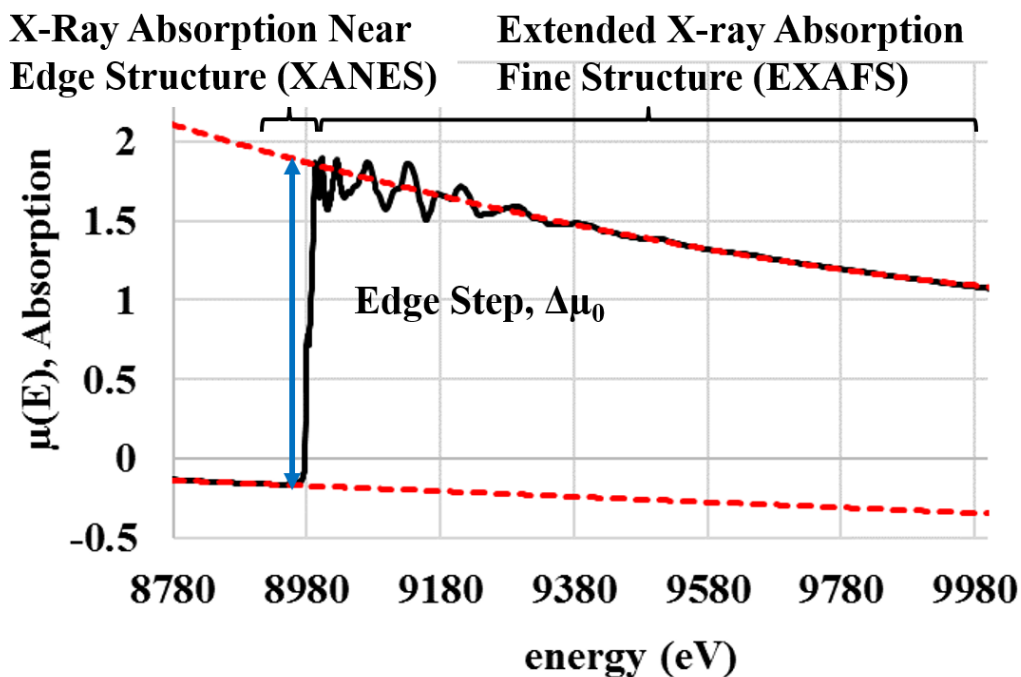


Figure 17: K-edge step for reference Cu foil.

Scans for the Cu K-edge were performed between 8779 eV and 10079 keV with 5 eV steps in the pre-edge region (-200 to -30 eV relative to edge energy), 0.5 eV steps in the XANES region (-30 to 60 eV relative to edge energy), and 0.05 Å⁻¹ in the EXAFS region (above 60 eV relative to edge energy). Scans were performed with the same pre-edge, XANES, and EXAFS step settings for the Ni K-edge between 8133 eV and 9433 eV, and scans for the Co K-edge were performed between 7509 eV and 8809 eV using the same criteria used to define the regions for Cu.

Electrode samples (negative electrode and positive electrode) were scanned from three locations (exterior, middle, interior) of 0 V, 0.25 V, 0.5 V, and 2.5 V (healthy) cells. Transmission data were collected for every experiment; however, fluorescence

signal was only measured for negative electrode samples but not the positive electrode samples due to the fact that copper in the positive electrode could not be resolved due to the overwhelming Ni and Co fluorescence signal from the active material.

Additionally, reference samples were prepared in advance by using a mortar and pestle to manually grind the powder. Powders were ultrasonically sifted to isolate particles less than 20 μm in diameter. The reference powder was mixed with boron nitride using a magnetic stir rod in ratios that would produce a K-edge step of about 1. Approximately 80mg of this mixture was compressed inside of a 12 mm x 5 mm pellet press using a force of 1.5 metric tons. After pressing the sample, a rectangular pellet was removed and sandwiched between Scotch tape to prevent contamination. The Scotch tape was investigated prior to use to ensure that it did not contain trace impurities of the metals of interest. Pellets of $\text{Cu}(\text{OH})_2$, Cu_2O , CuO , CuF_2 , and NCA ($\text{LiNi}_{0.8}\text{Co}_{0.15}\text{Al}_{0.05}\text{O}_2$) were brought to the beamline. The choice of reference samples included possible copper compounds that could be created in addition to positive electrode active materials matching the cell under study.

4.3.6 – Three-electrode cell

To observe the individual electrode voltages with respect to Lithium when a cell is overdischarged, three-electrode pouch cells are constructed according to Figure 18. The pouch cell is assembled inside of an Argon-filled glovebox and removed once electrolyte has been injected into the cell and the cell is sealed. The electrodes are harvested from a disassembled large-format lithium-ion cell that was stored at a voltage above 2.5 V. This is the same type of cell used for the rest of the study.

Roughly 25 mm x 38 mm rectangular pieces are cut from both the positive and negative electrodes and rinsed with dimethyl carbonate (DMC). Nickel tabs are ultrasonically welded to the exposed current collector and a piece of 25 μm thick PP/PE/PP tri-layer Celgard separator is taped to each of the electrodes with Kapton tape. The electrodes are then taped together as seen in Figure 19. The reference electrode is constructed by welding nickel mesh to a nickel tab, and a piece of lithium metal is mechanically pressed into the nickel mesh as seen in Figure 20. The pouch is folded on one edge, welded with the positive and negative electrode tabs at the top, and welded with the lithium reference electrode on the side. The bottom of the pouch is left open and a syringe filled with 2mL electrolyte (1 M LiPF_6 in EC:EMC (3:7 by volume)) was injected into the pouch. The bottom is sealed and the pouch cell is removed from the glovebox for cycling.

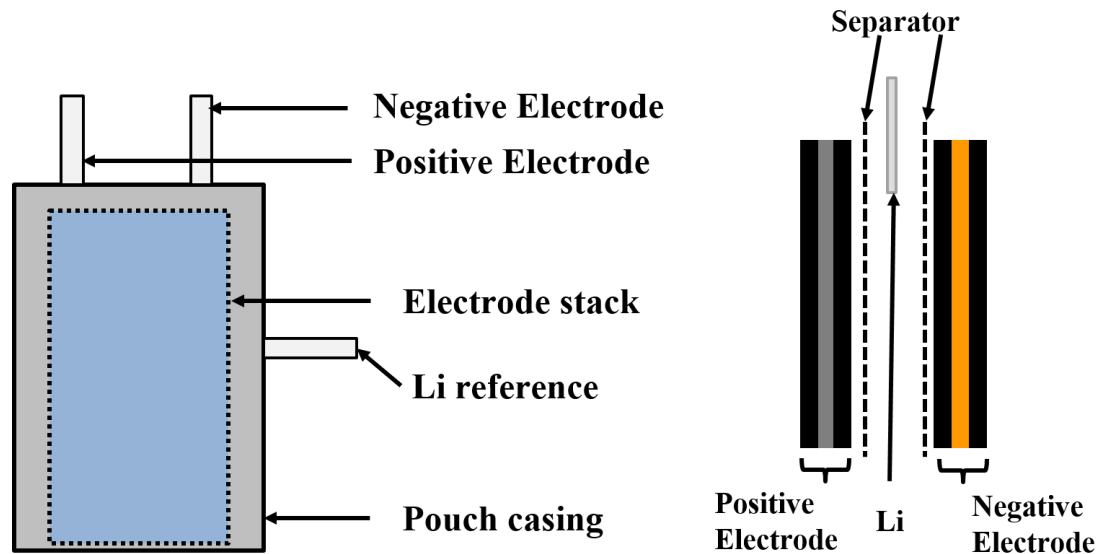


Figure 18: Three-electrode assembly

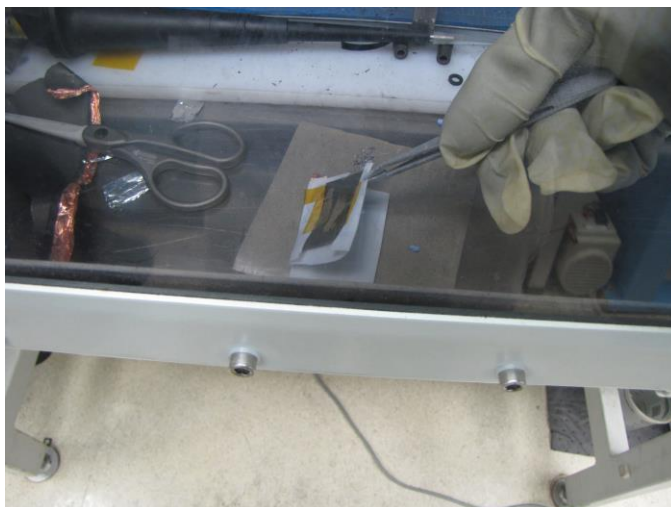


Figure 19: Electrode stack assembly



Figure 20: Lithium reference electrode

Cycling is conducted using a Gamry Interface 1010E Potentionstat/Galvanostat/ZRA to charge and discharge the positive and negative electrodes. An Agilent 34970A data acquisition unit is used to monitor the full cell voltage between the positive and negative electrodes, the half-cell voltage between the positive and Li reference electrodes, and the half-cell voltage between the negative and Li reference electrodes. The cell is charged at a rate of 2 mA until the full cell voltage reaches 4.1 V. The cell

is allowed to rest for 1 hour at open circuit to observe any anomalous behavior, and then it is discharged at 2 mA until the full cell voltage reaches 0 V.

4.3.7 – Coin cell

Electrodes were harvested from one of the control samples that did not undergo overdischarge and assembled into full coin cells with an NCA positive electrode and a graphite negative electrode. Disks 15 mm in diameter were punched from the electrode sheets towards the edge of the electrode with exposed current collector. The current collector was folded behind the electrode as shown in Figure 21 to make contact with the coin cell casing. The coin cell consisted of a positive CR2032 case, a negative CR2032 case with gasket, 2 500 μm spacers, a spring, the positive electrode, the negative electrode, and a Celgard separator, and 225 μL of 1 M LiPF₆ in 3:7 EC:EMC electrolyte. Assembly was conducted inside of a glovebox with oxygen content < 1 ppm according to the schematic outlined in Figure 22. One of the spacers was placed in the positive section of the coin cell case, followed by the positive electrode. 75 μL of electrolyte was used to wet the electrode surface, and the separator was placed on top after being soaked in electrolyte for 5 minutes. 150 μL of electrolyte was dispensed into the cell and the negative electrode was placed face down on the separator. Another spacer and the spring were placed on top of the negative electrode, followed by the negative section of the coin cell case. The coin cell was crimped and removed from the glovebox for testing.



Figure 21: Negative electrode with current collector folded over.

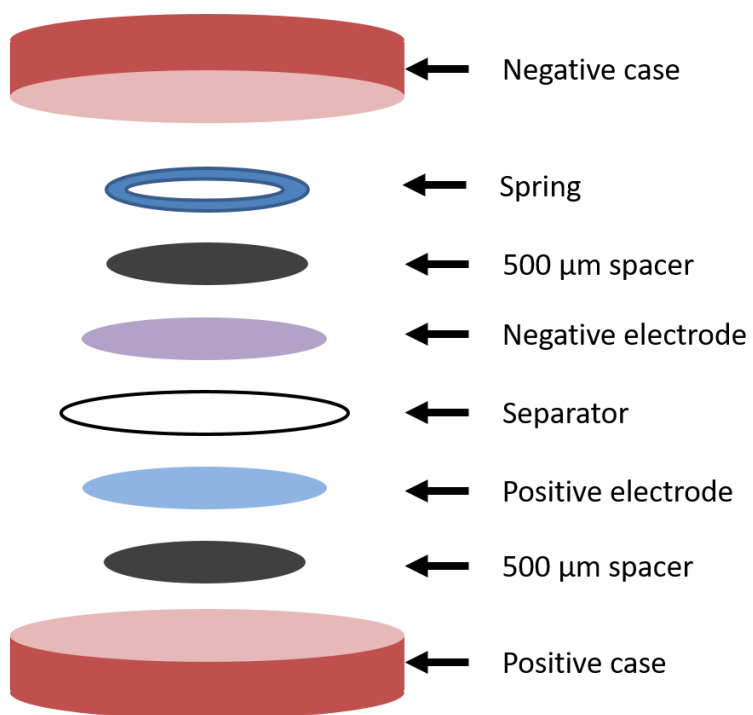


Figure 22: Coin cell schematic

Cycling was conducted on an Arbin LBT21084 commercial battery cycler in a temperature chamber at a constant 25°C. Two coin cells were charged to 4.1 V at a rate of 0.35 mA (approximately C/10 C-Rate), allowed to rest for 1 hour, and

discharged at a rate of 0.35 mA to 0 V. The cell was held at 0 V for 48 hours, and then recharged to 2.5 V at a rate of 0.35 mA. The cells were then cycled between 2.5 V and 4.1 V at a rate of 1.75 mA (approximately C/2 C-Rate) 10 times and then disassembled in the charged state and examined via XPS analysis in the same manner as previously discussed in 4.3.4.

4.4 – Results and Discussion

4.4.1 – SEM

SEM images for a healthy cell that was discharged to 2.5 V can be seen for the negative electrode in Figure 23 and Figure 24. The negative electrode looks like a typical graphite electrode from a lithium-ion battery with a graphite flakes and carbon black conductive additives.

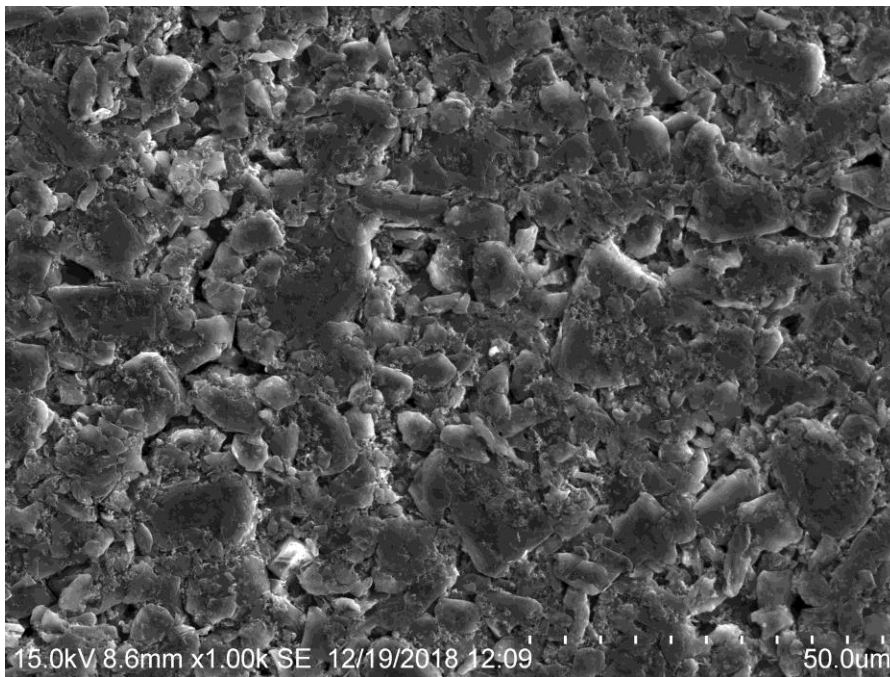


Figure 23: SEM micrograph of negative electrode from a healthy cell.

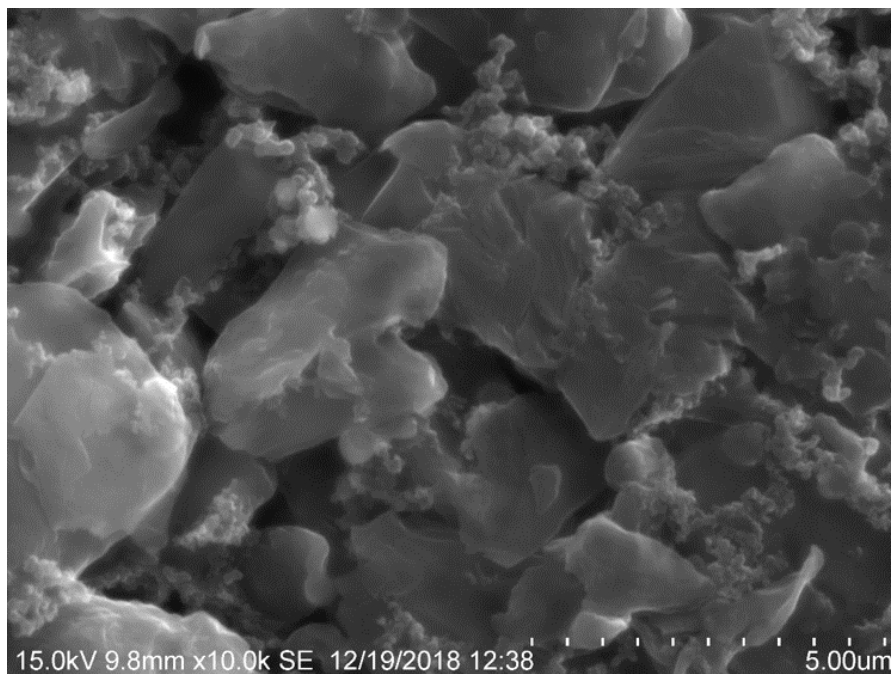


Figure 24: SEM micrograph of negative electrode from a healthy cell at 10,000x magnification.

Similarly, the positive electrode seen in Figure 25 and Figure 26 shows an agglomeration of sub-micron active material particles without any abnormalities.

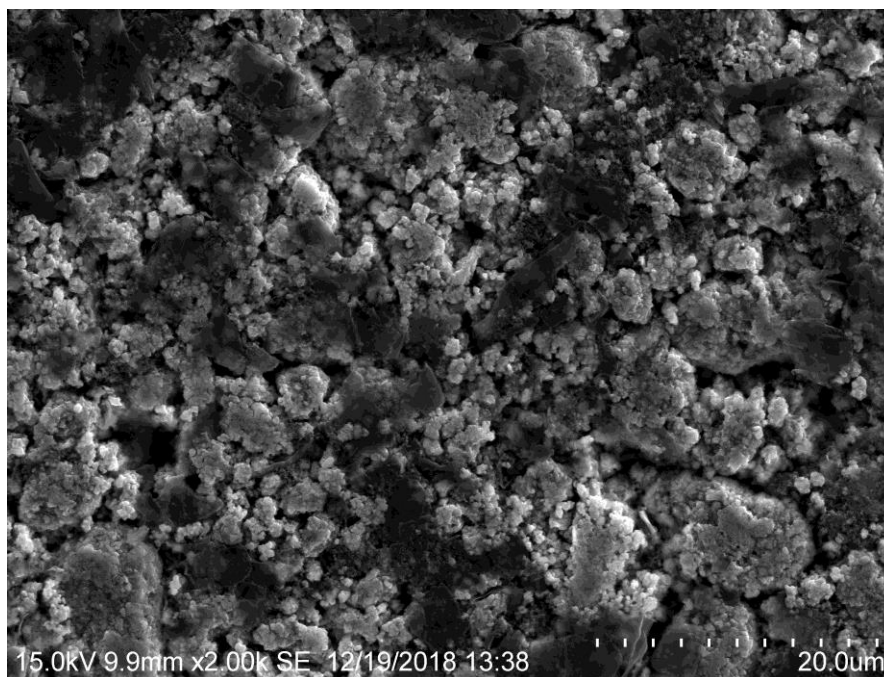


Figure 25: SEM micrograph of positive electrode from a healthy cell.

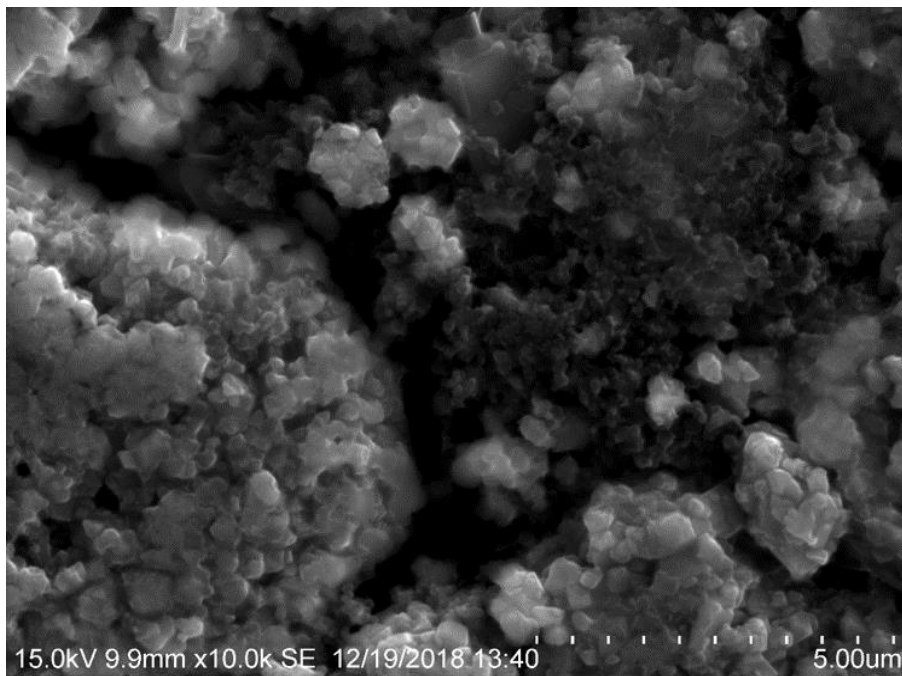


Figure 26: SEM micrograph of positive electrode from a healthy cell at 10,000x magnification.

In contrast, deposits on the surface of the negative electrode are seen for both the 0 V and 0.25 V cells shown in Figure 27 and Figure 28. Well dispersed deposits on the surface of the graphite particles in the overdischarged cells are observed, and the deposits do not fully coat the surface of the particle.

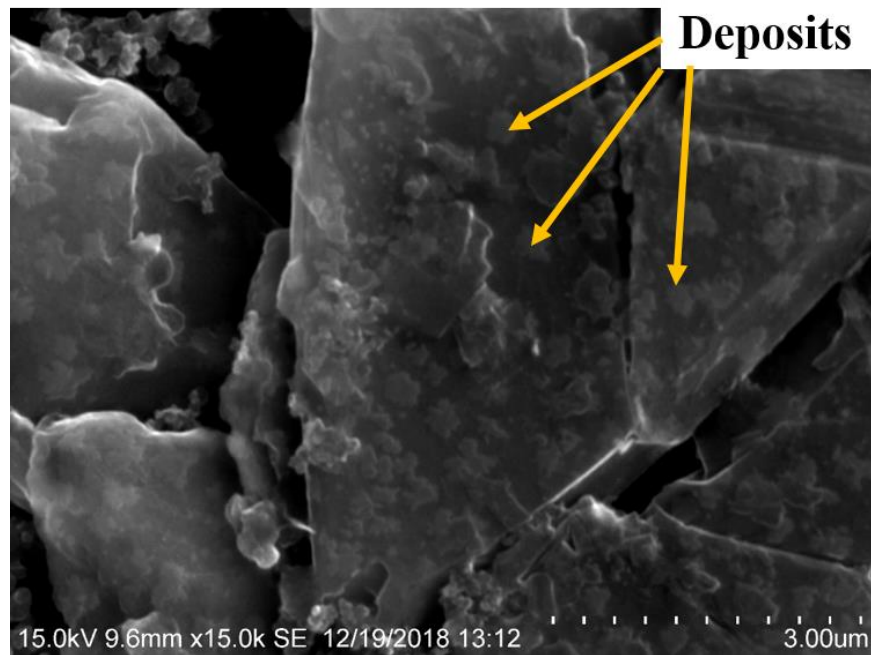


Figure 27: SEM micrograph of graphite particle in a cell overdischarged to 0 V. Deposits on the surface of the particle can be clearly observed at 15,000x magnification.

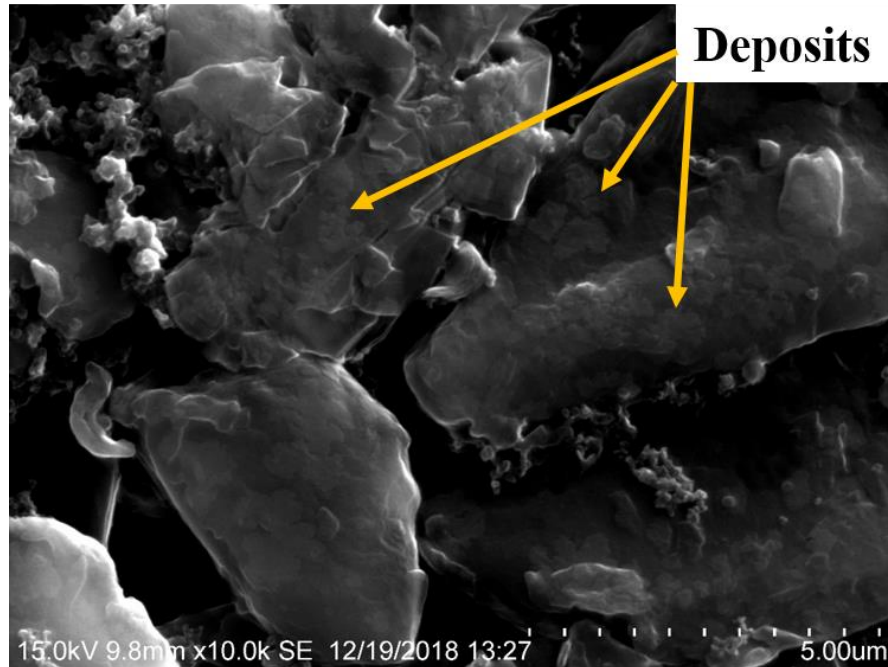


Figure 28: SEM micrograph of graphite particle in a cell overdischarged to 0.25 V. Deposits on the surface of the particle can be clearly observed at 10,000x magnification.

The positive electrodes from the 0 V and 0.25 V overdischarged cells did not exhibit damage or the presence of deposits on the electrode surface. Figure 29 and Figure 30 show the surface of the cathode for the 0 V and 0.25 V cells, respectively.

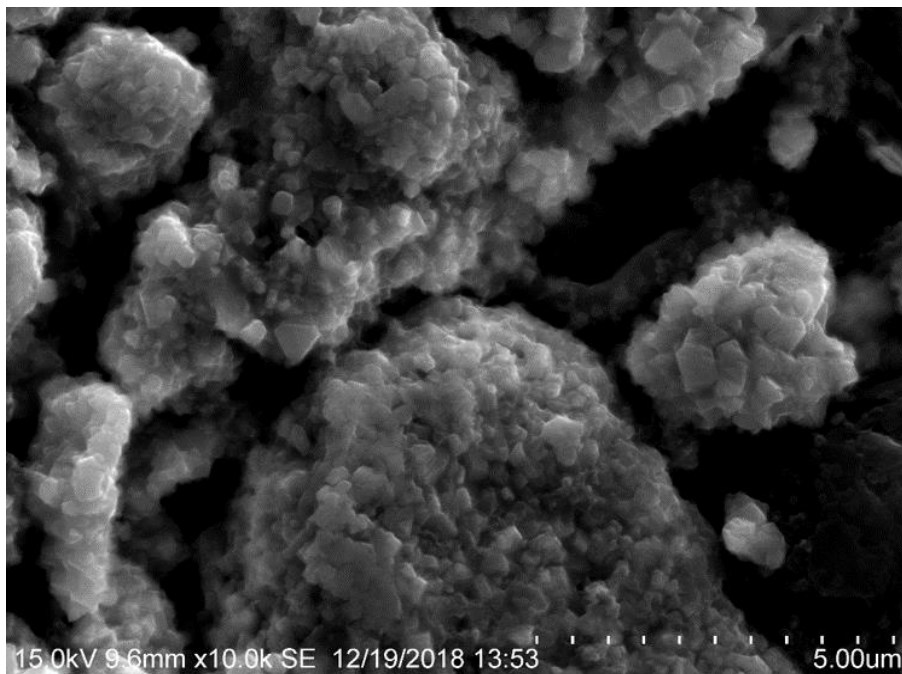


Figure 29: SEM micrograph of cathode particle in a cell overdischarged to 0 V

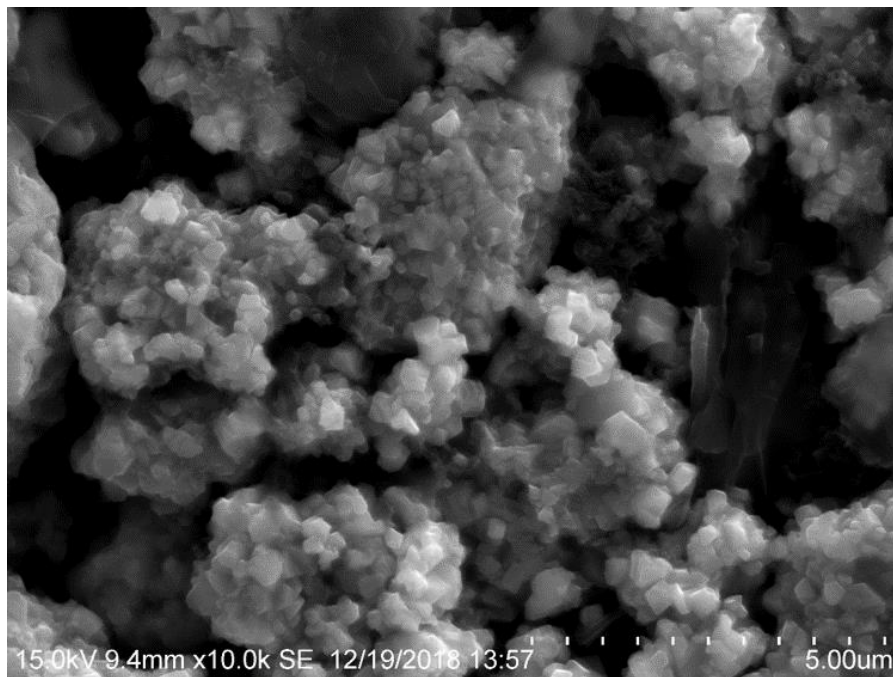


Figure 30: SEM micrograph of cathode particle in a cell overdischarged to 0.25 V

Scans taken with an EDS show that a low concentration of copper is found on the surface of the 0 V overdischarged cell as seen in Figure 32, but the same peak is not

detected in the healthy cell shown in Figure 31. The presence of copper in overdischarged cells indicate that dissolution of the negative electrode's copper current collector is possible when a cell is overdischarged at low as 0 V. The SEM and EDS results, however, cannot provide any information about the risk of short circuit from the copper. To determine the risk of short circuit in cells overdischarged to voltages as low as 0 V, it is necessary to understand whether the copper exists in a conductive or non-conductive state. The use of XPS and XAFS to determine the chemical state of the copper is presented in sections 4.4.4 and 4.4.5.

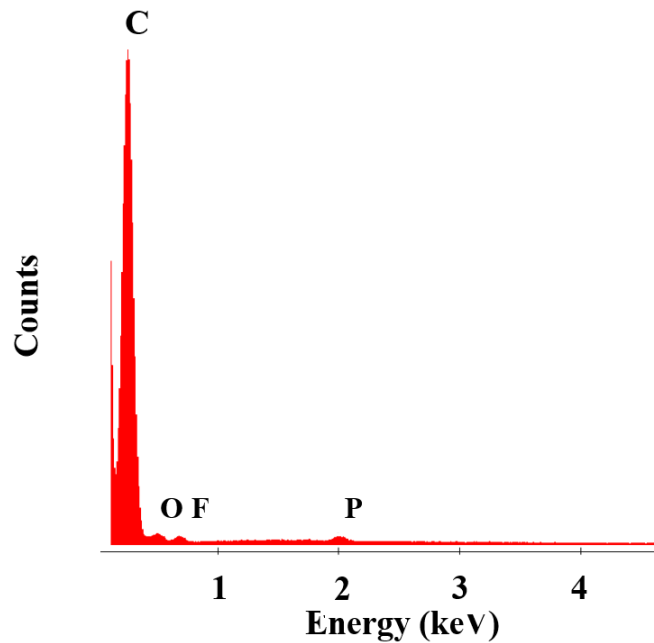


Figure 31: EDS spectra for a negative electrode from a healthy cell

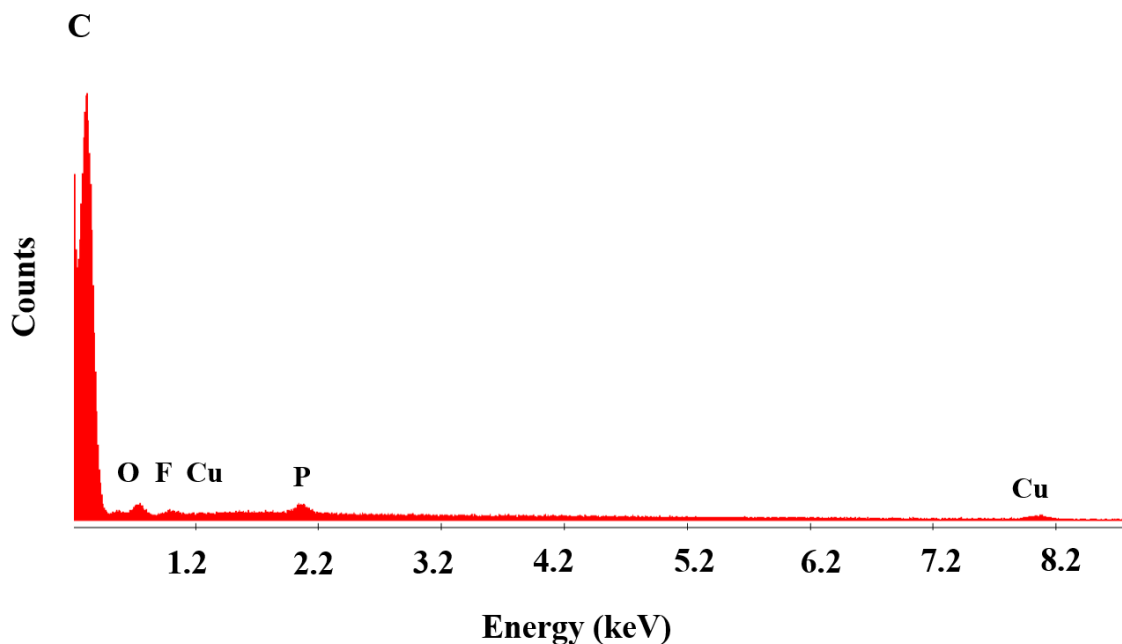


Figure 32: EDS spectra for a negative electrode from a cell overdischarged to 0 V.

4.4.2 – Three-electrode measurements

Electrochemical testing of electrodes harvested from a healthy cell is conducted in a three-electrode configuration with a reference lithium metal electrode. The full cell voltage (NCA and Graphite) as well as the positive electrode half cell (NCA and Li) and the negative electrode half cell (Graphite and Li) are all plotted in Figure 33. The potential of each individual electrode with respect to Li/Li^+ are given in Table 2 for the relevant full cell voltages tested in the overdischarge study. It is clear that full cell voltages of 0 V and 0.25 V result in a negative electrode potential reaching the copper dissolution limits reported in literature of approximately 3.1 – 3.6 V vs. Li/Li^+ .

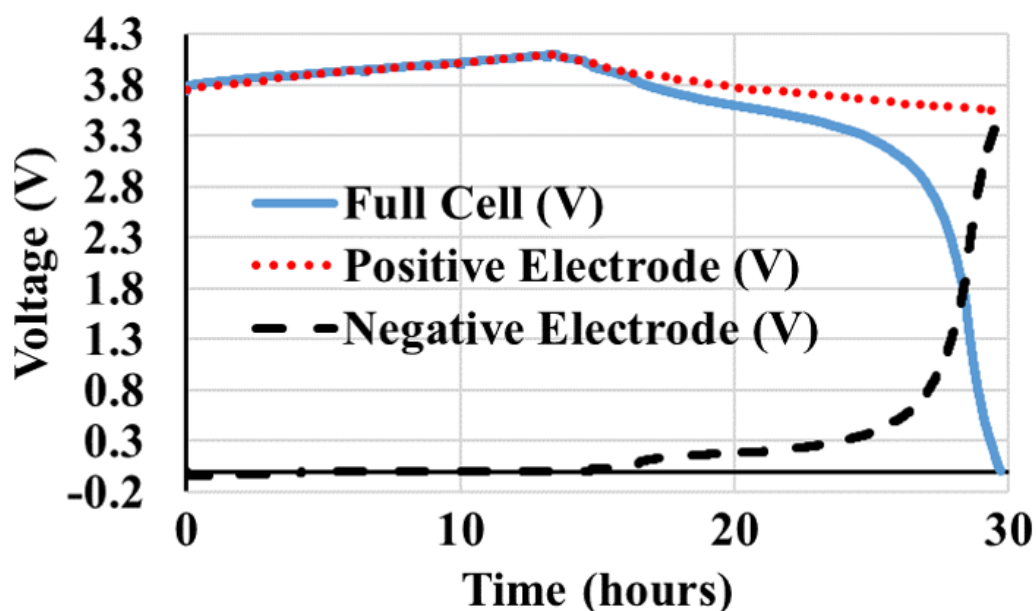


Figure 33: Overdischarge of three-electrode pouch cell to 0 V.

Table 2: Full cell voltage and the voltage of each electrode with respect to Li/Li⁺

Full Cell Voltage	Positive Electrode vs Li/Li ⁺	Negative Electrode vs Li/Li ⁺
2.5	3.58	1.08
0.5	3.55	3.05
0.25	3.55	3.3
0	3.54	3.54

4.4.3 – Cycling comparison

Cells are cycled following overdischarge to observe the effects of overdischarge on cell performance. After the single overdischarge event, the cells are cycled within their operational voltage limits of 2.5 V and 4.1 V. The cells are then compared to “healthy” cells that never experienced overdischarge. The mean capacity fade of overdischarged cells is given in Figure 34 and compared to a healthy cell. The mean for each of the overdischarge voltages was taken over 3 different cells, and the error bars represent the standard deviation.

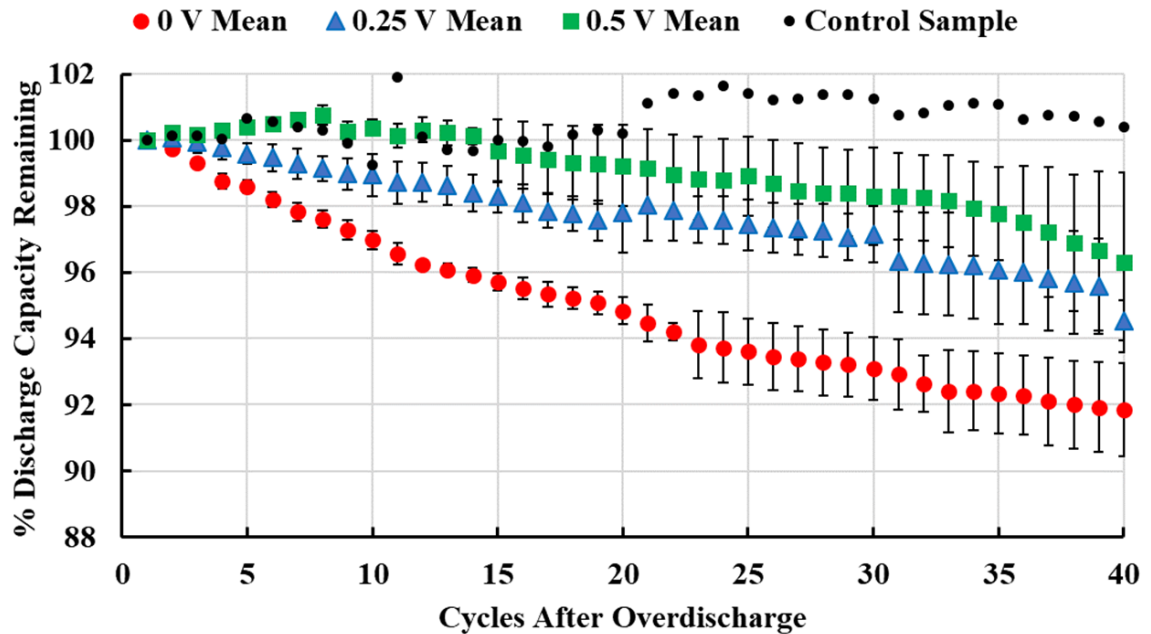


Figure 34: Cycling following a single overdischarge event

Overdischarged cells below 0.5 V display a more rapid capacity fade than cells maintained at a voltage within the battery’s operating range. Over the course of 40 cycles, the capacity of the overdischarged cell decreases by as much as 10%, whereas the healthy cell does not decrease at all. Capacity fade for 0.5 V, 0.25 V, and 0 V cells are shown separately in Figure 35, Figure 36, Figure 37, respectively. The capacity fade observed in cells overdischarged exhibits variability; however, the variability is greatest for the three cells overdischarged to 0.5 V. Over 40 cycles, one cell exhibited approximately 7% degradation in capacity and another cell experienced less than 1% degradation.

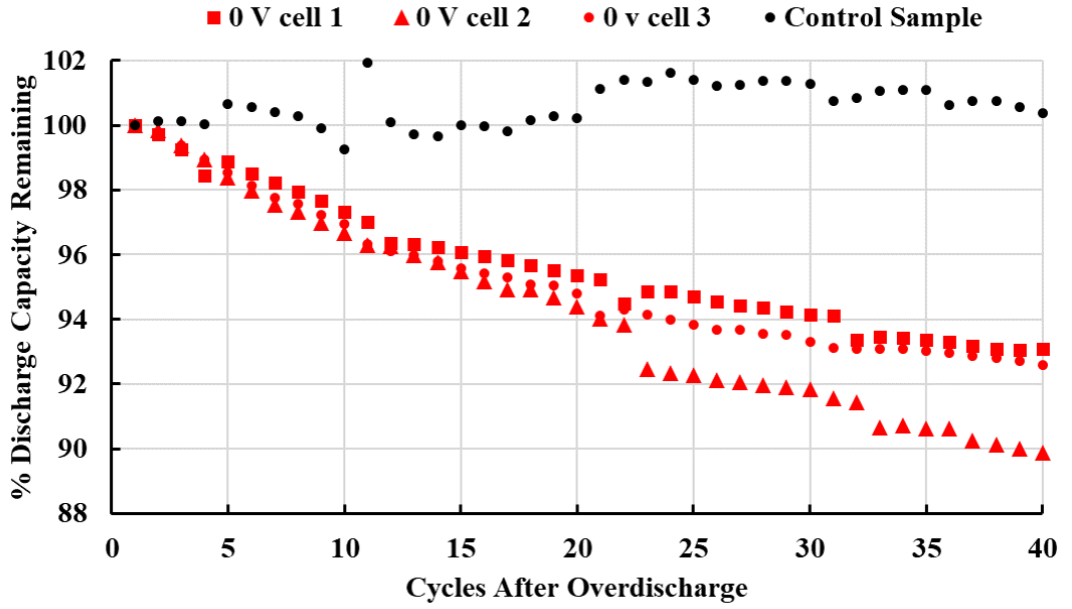


Figure 35: Capacity fade for 3 cells overdischarged to 0 V and then cycled within nominal voltage range of 2.5 V to 4.1 V.

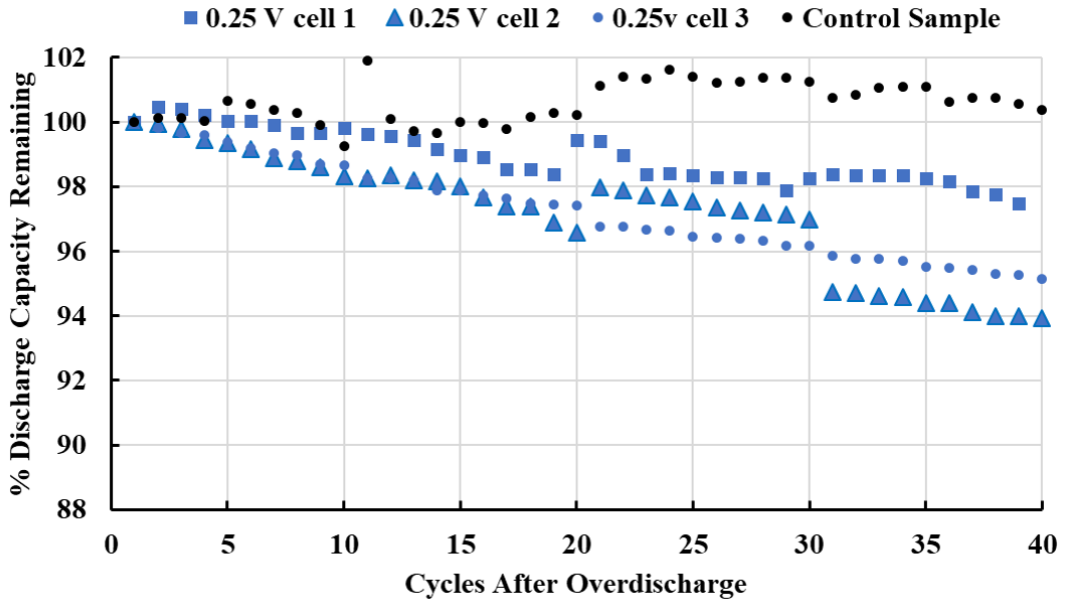


Figure 36: Capacity fade for 3 cells overdischarged to 0.25 V and then cycled within nominal voltage range of 2.5 V to 4.1 V.

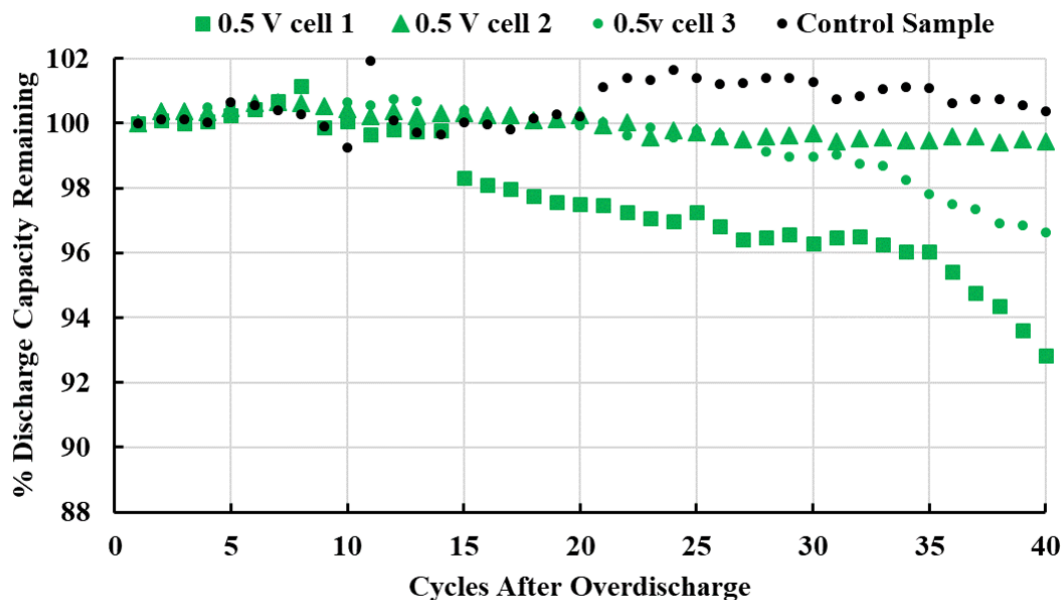


Figure 37: Capacity fade for 3 cells overdischarged to 0.5 V and then cycled within nominal voltage range of 2.5 V to 4.1 V.

Similarly, impedance plots taken at the beginning of cycling and at the end of cycling are shown in Figure 38 and Figure 39, respectively. The impedance of the cells overdischarged to voltages less than 0.5 V are at least twice as large as the healthy cell and one of the 0.5 V cells. After 40 cycles, all cells except for the 0 V cells have impedances matching the healthy cell.

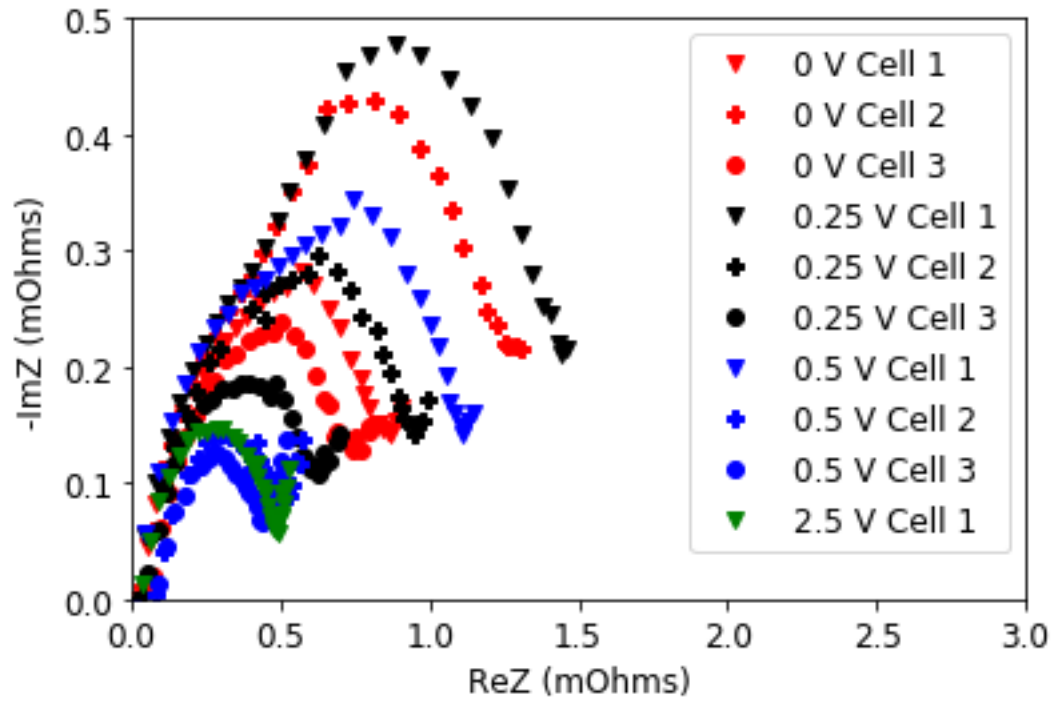


Figure 38: Impedance prior to cycling

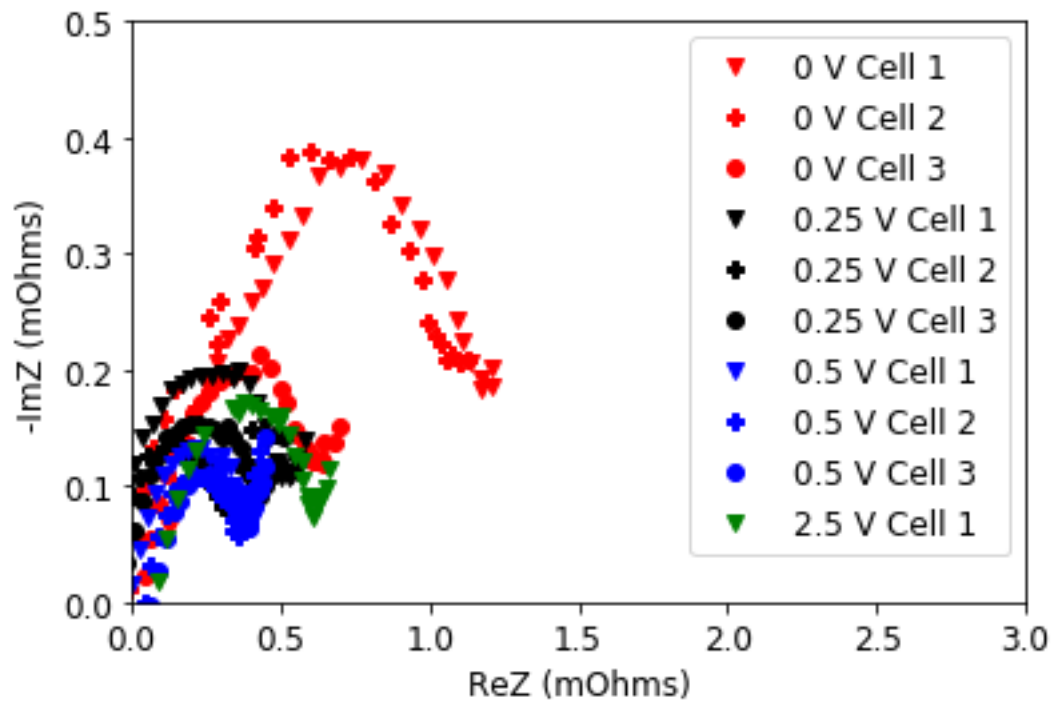


Figure 39: Impedance after 40 cycles

Impedance trends for each of the overdischarged cells illustrate that a decrease of impedance is observed after the first 10 cycles and continues to decrease for 0.25 V and 0.5 V cells. The 0.25 V cell impedance reduction over 40 cycles can be seen in Figure 40, Figure 41, and Figure 42, and the 0.5 V cell impedance reduction can be seen in Figure 43, Figure 44, and Figure 45.

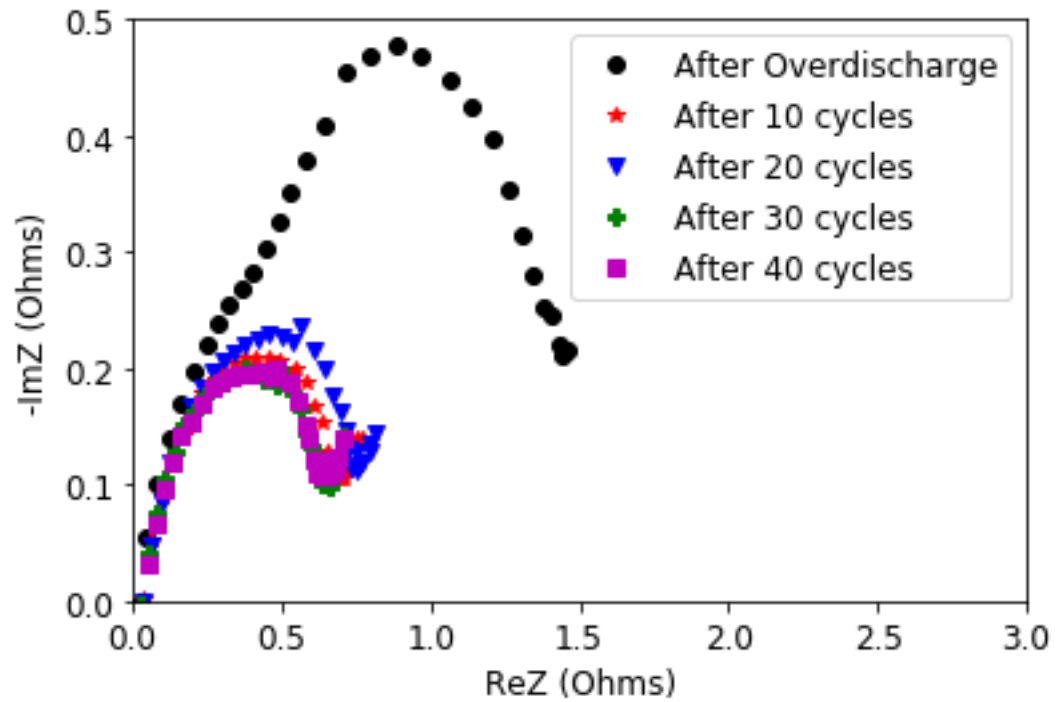


Figure 40: 0.25 V cell 1 impedance

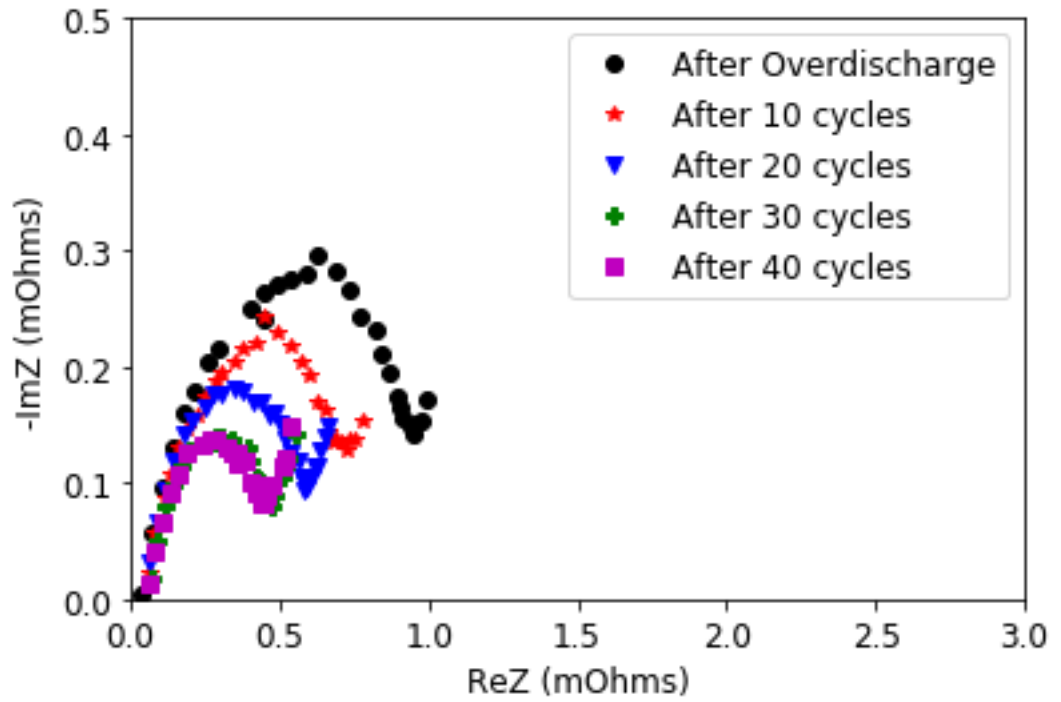


Figure 41: 0.25 V cell 2 impedance

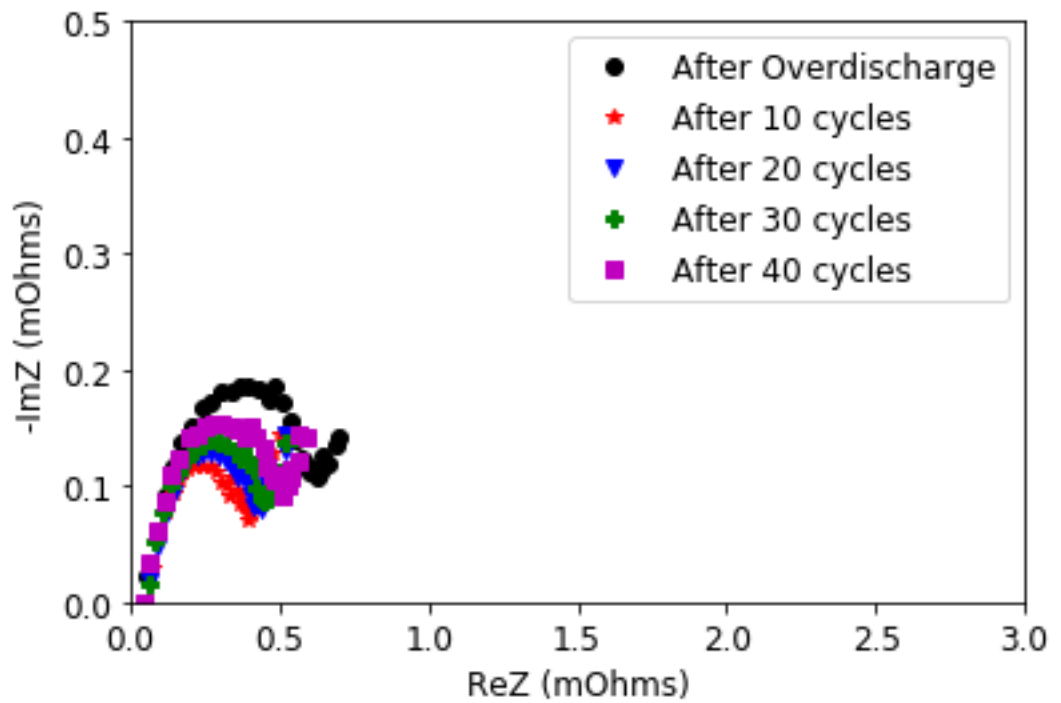


Figure 42: 0.25 V cell 3 impedance

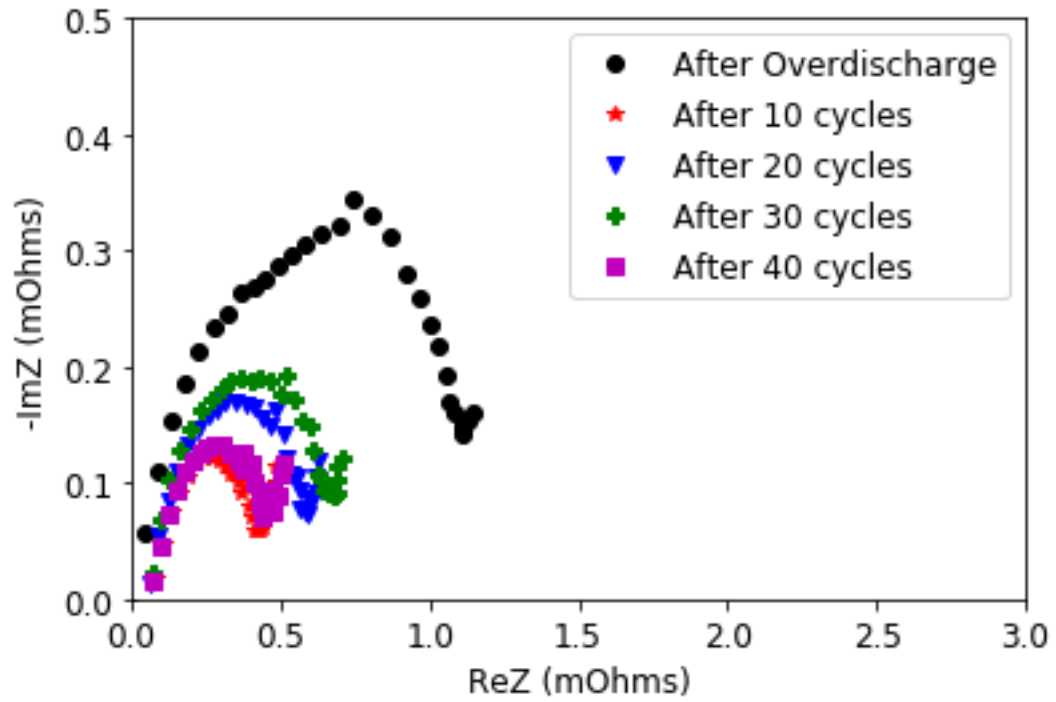


Figure 43: 0.5 V cell 1 impedance

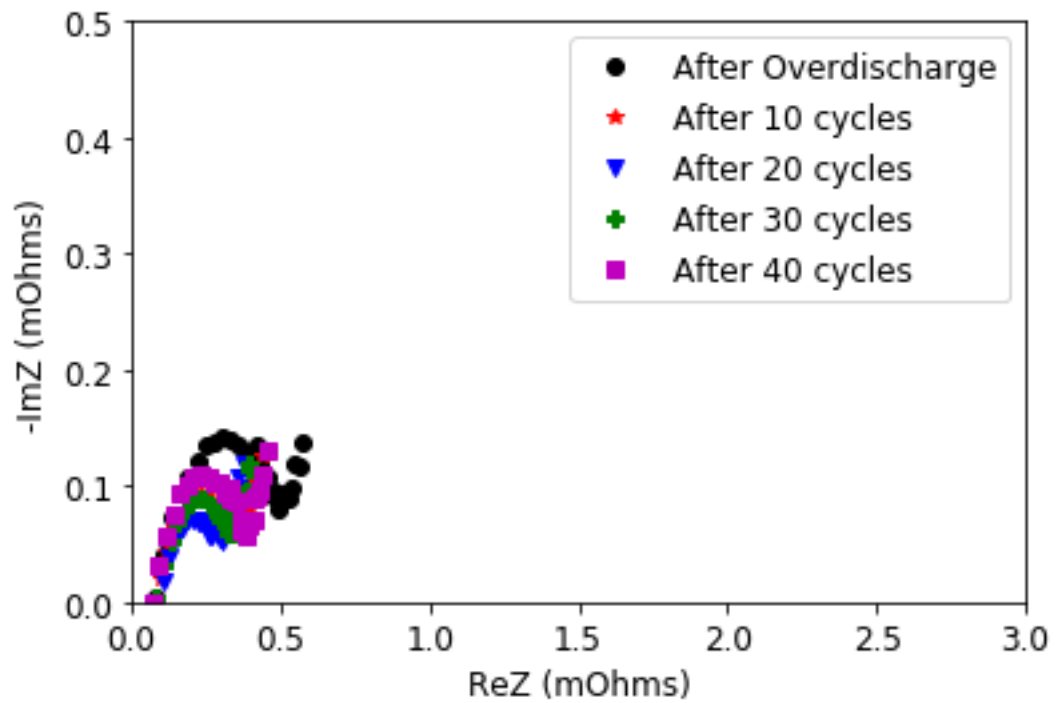


Figure 44: 0.5 V cell 2 impedance

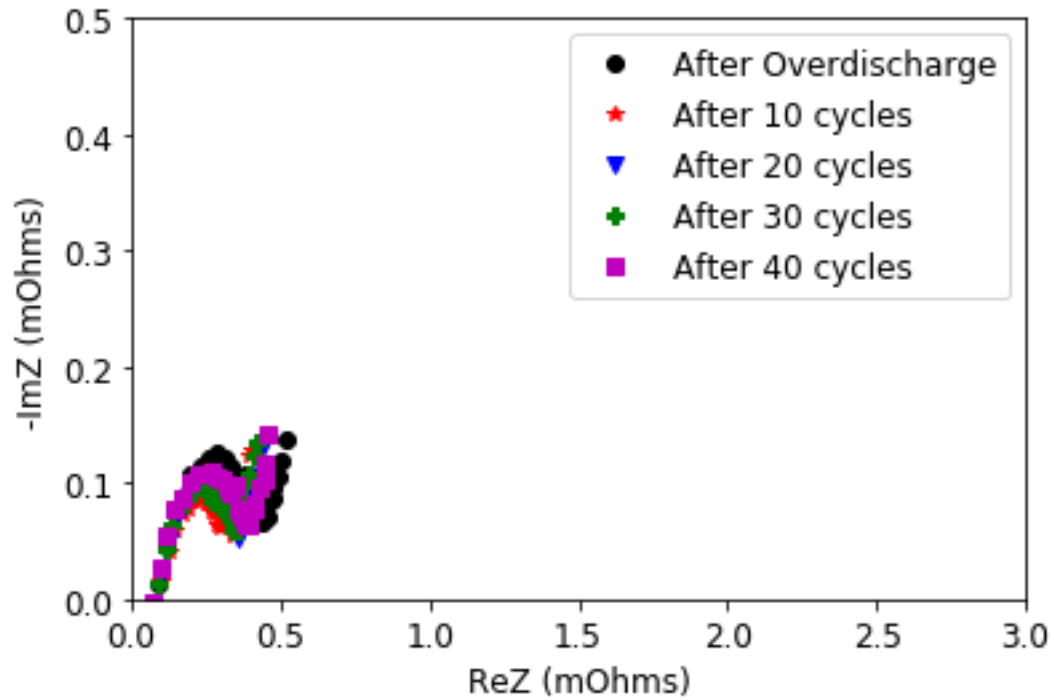


Figure 45: 0.5 V cell 3 impedance

Alternatively, the 0 V cells show an initial decrease in impedance following by an increase, as illustrated in Figure 46, Figure 47, and Figure 48. These cells also exhibited the worst capacity fade behavior. Clearly the degree of overdischarge plays a significant role on the subsequent stability of the cell if recovered. A more severe overdischarge will lead to greater copper dissolution and greater performance degradation as a result.

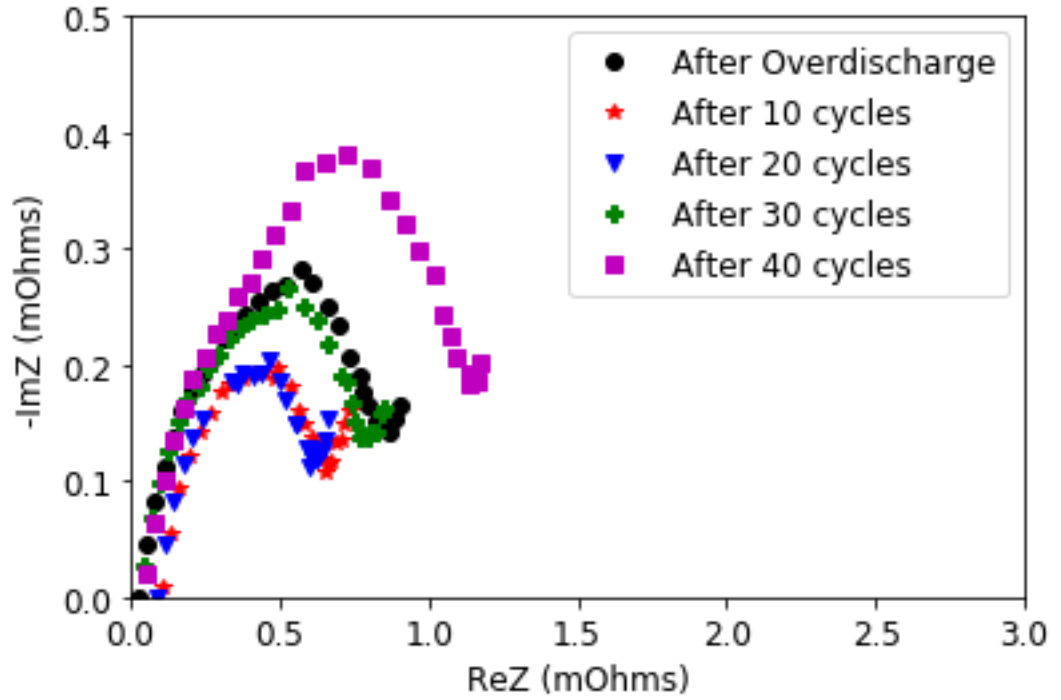


Figure 46: 0 V cell 1 impedance

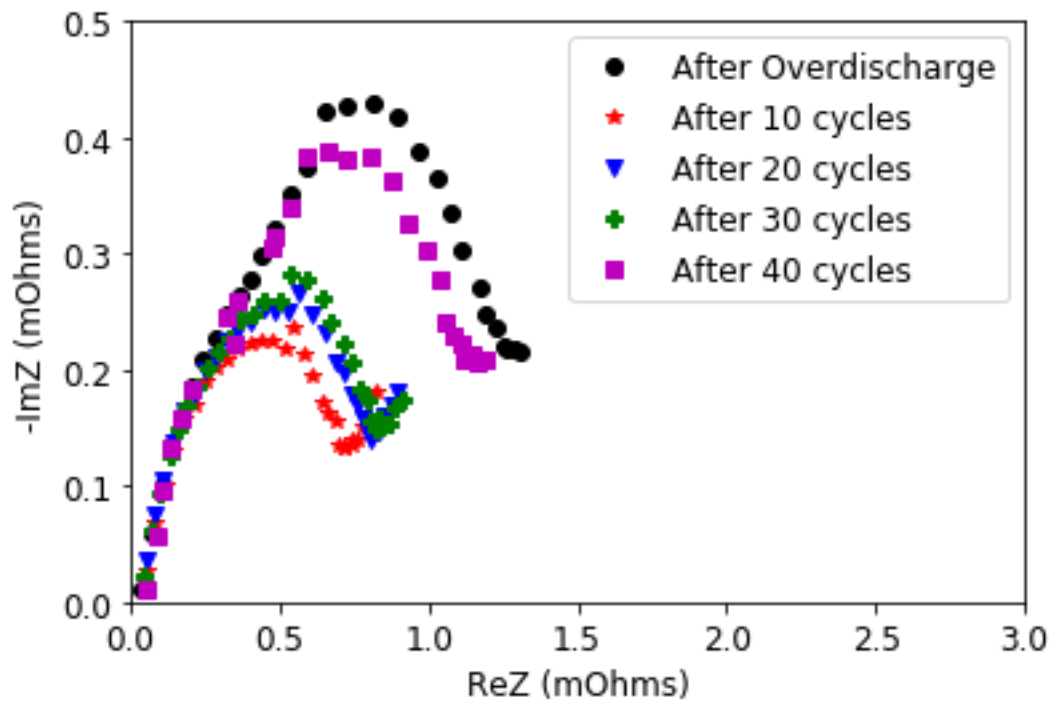


Figure 47: 0 V cell 2 impedance

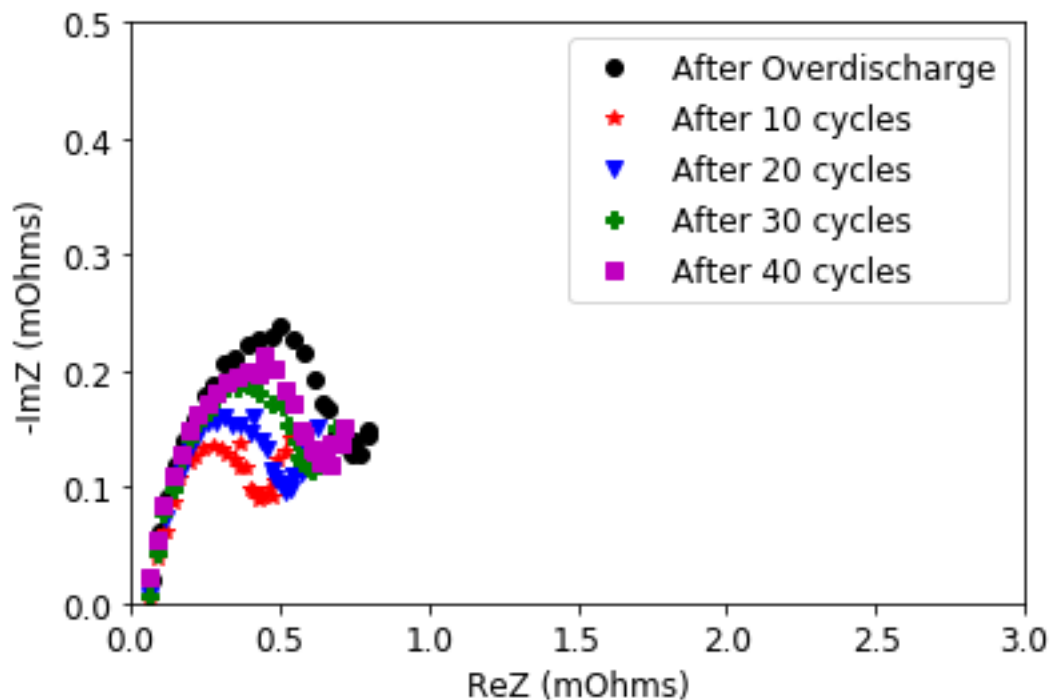


Figure 48: 0 V cell 3 impedance

4.4.4 – XPS

XPS data analysis is conducted using Physical Electronics' MultiPak software, version 9.8. Analysis of the reference sample spectra provides a basis for identifying chemical state of unknown compounds in the composite electrode samples. XPS is used to look at the top ~5 nm of the sample surface, making it ideally suited for studying surface contamination

The Cu_{2p_{3/2}} spectra for the potential copper compounds are plotted in Figure 49. The spectra are aligned using the C1s hydrocarbon peak at 284.8 eV, and are decomposed with a Gaussian-Lorentzian function and Iterative Shirley background correction. A summary of the binding energy and FWHM for the reference samples is included in Table 3.

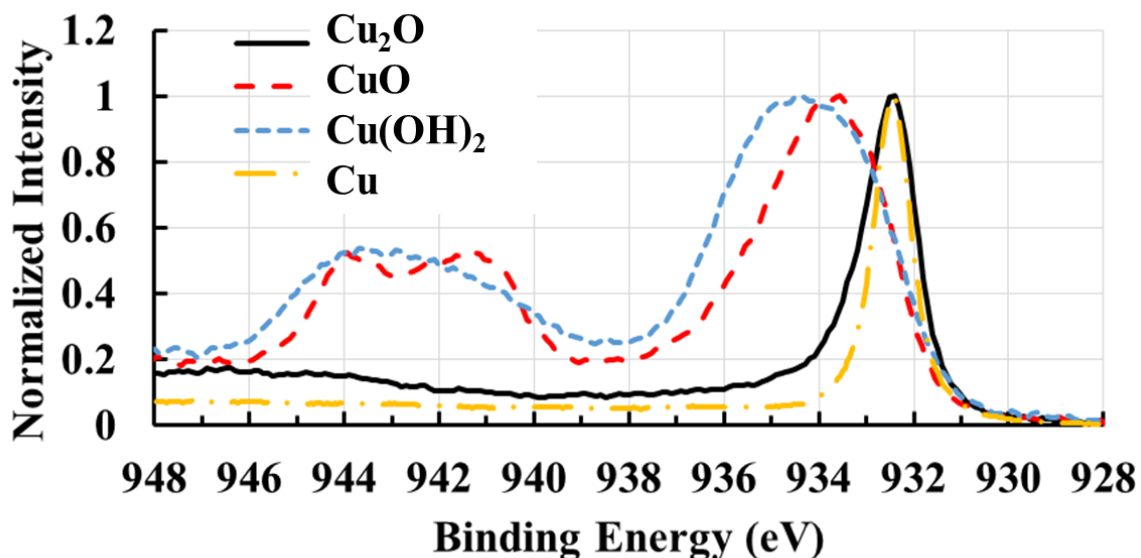


Figure 49: Copper reference samples, Cu_{2p_{3/2}} region

Table 3: Summary of copper reference sample fit parameters

Sample	eV	FWHM
Cu	932.4	0.96
Cu(OH) ₂	933.0	2.45
	934.9	2.23
Cu ₂ O	932.6	1.35
CuO	933.4	2.26
	935.0	3.03
	941.4	2.65
	943.9	1.78

A summary of the average atomic percentages of each element measured in the negative electrode and positive electrode samples are listed in Table 4 and Table 5, respectively. Atomic percentages were calculated using the multiplex scans in which greater resolution is obtained. The survey scan taken prior to multiplex scans confirmed that the predominant elements represented in each sample are Li, C, O, F, P, and Cu.

No copper is detected in the 2.5 V control sample on either the negative electrode or positive electrode, which is within expectations. During typical operation of a lithium-ion battery, the potential of the negative electrode vs. Li/Li⁺ should not reach the dissolution limit. The 0.5 V overdischarge case exhibits a small amount of copper on the negative electrode side; however, only one of the samples showed the presence of copper as seen in Figure 50. It is unlikely that significant copper dissolution occurs at 0.5 V; however, it may be near the dissolution threshold.

Table 4: Average elemental atomic percentage in negative electrode samples

Sample	Voltage	Recharge?	Atm%					
			Li1s	C1s	O1s	F1s	P2p	Cu2p3
1	0	N	8.9	40.5	29.4	14.6	3.6	3.1
2	0	Y	19.3	34.6	21.6	20.8	3.1	0.6
3	0.25	N	13.8	40.2	23.4	18.0	3.7	0.9
4	0.25	N	15.3	37.4	23.6	19.1	3.4	1.1
5	0.25	Y	16.4	36.6	21.5	21.8	2.6	1.1
6	0.5	N	16.1	39.9	19.1	21.0	3.8	0.04
7	2.5	N	18.0	39.6	24.0	15.7	2.7	0.0

Table 5: Average elemental atomic percentage in positive electrode samples

Sample	Voltage	Recharge?	Atm%							
			Li1s	C1s	O1s	F1s	P2p	Co2p	Ni2p	Cu2p3
1	0	N	11.0	43.3	12.8	28.0	1.6	0.0	2.8	0.5
2	0	Y	16.4	37.2	12.5	28.8	1.8	0.0	3.0	0.3
3	0.25	N	13.9	39.9	12.8	28.4	1.7	0.0	3.0	0.3
4	0.25	N	10.2	42.8	12.5	29.6	1.3	0.0	3.1	0.6

5	0.25	Y	10.5	43.8	12.9	27.7	1.6	0.0	2.9	0.5
6	0.5	N	16.4	38.4	10.2	31.8	1.3	0.1	1.8	0.0
7	2.5	N	12.8	40.9	13.1	28.5	1.4	0.0	3.4	0.0

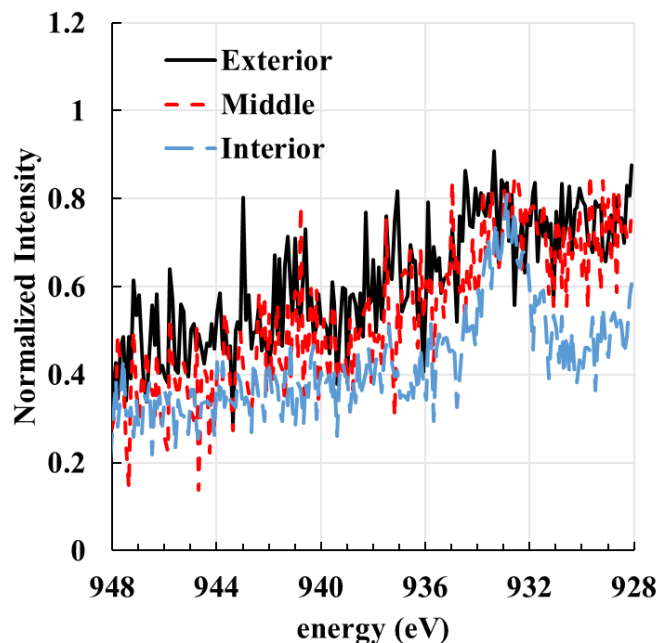


Figure 50: Cu $2p_{3/2}$ region of 0.5 Volt cell negative electrode. Slight copper peak with binding energy around 933 eV is observed.

Negative electrode samples can contain amorphous and graphitic carbon with slightly lower binding energy relative to the C1s hydrocarbon signal. Negative and positive electrode spectra are aligned using the C1s hydrocarbon peak at 284.8 eV. C1s (top) and Cu $2p_{3/2}$ (bottom) plots for samples 1, 2, 3, and 5 can be seen in Figure 51. All of the Cu $2p_{3/2}$ spectra from the samples illustrate the presence of both Cu $_2$ O and Cu(OH) $_2$ occurring around approximately 933 eV and 935 eV. Differences in the relative concentration of Cu $_2$ O to Cu(OH) $_2$ in each of the samples can be seen both in the intensity of the primary peaks, as well as the presence of the satellite structure between 939 eV and 946 eV. Both of the 0 V cells seem to contain a greater relative

concentration of $\text{Cu}(\text{OH})_2$ compared to the 0.25 V cells as illustrated with the more prominent satellite structure and the stronger peak occurring around 935 eV. Similar trends can be seen for the positive electrode in Figure 52, albeit shifted to a slightly higher binding energy. This discrepancy can be attributed to the lower concentration of copper on the positive electrode, leading to a noisy signal. Calibration and alignment of the peaks will have more error in this instance; however, it is clear that the $\text{Cu}2p_{3/2}$ peaks correspond to Cu_2O and $\text{Cu}(\text{OH})_2$.

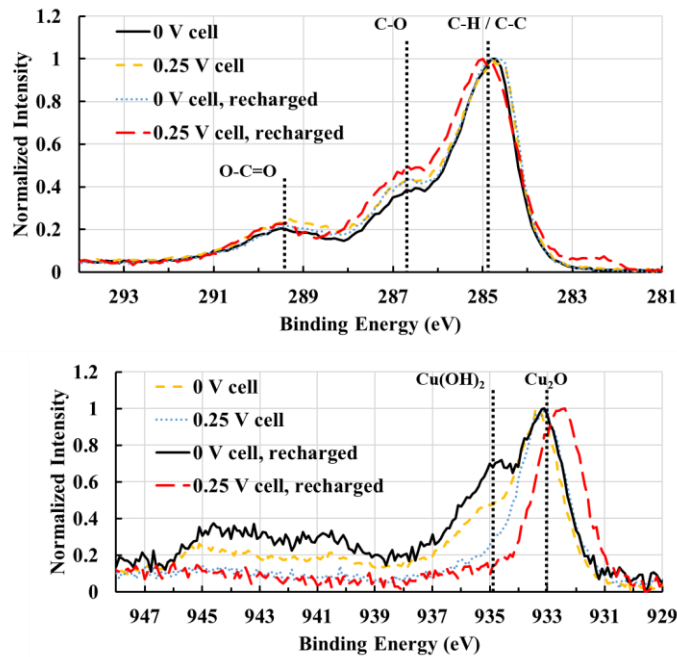


Figure 51: C1s (top) and Cu2p_{3/2} (bottom) spectra for negative electrodes from samples 1, 2, 3, and 5.

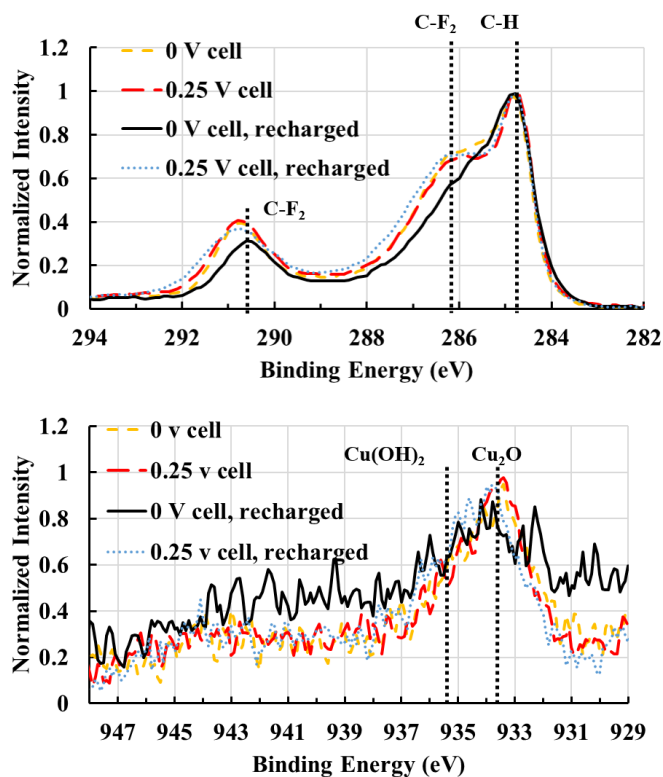


Figure 52: C1s (top) and Cu2p_{3/2} (bottom) spectra for positive electrodes from samples 1, 2, 3, and 5.

XPS analysis was performed on the negative electrode from a 0.25 V cell repeatedly cycled for 40 cycles. The initial scan revealed very little copper, with a 0.04 atm % relative concentration. Sputtering with a 3 kV Argon ion gun allowed for the removal of surface layers of the sample at a rate equivalent to the removal of 8 nm of SiO₂/minute. Because of the heterogeneous nature of the SEI layer and the electrode of a lithium-ion battery, it was not possible to specify a sputtering rate with respect to the SEI layer components. Sputtering was conducted in 15 second intervals followed by a scan of the C1s and Cu2p_{3/2} peaks to observe changes in the chemical state of the newly revealed surface. Figure 53 and Figure 54 show the progression of the C1s and Cu2p_{3/2} signal, respectively. The spectra are offset for clarity, but otherwise unaltered. The copper signal continues to grow in strength relative to the

C1s signal, and the C1s spectra begins to show a peak around 282.5 eV, consistent with intercalated graphite.

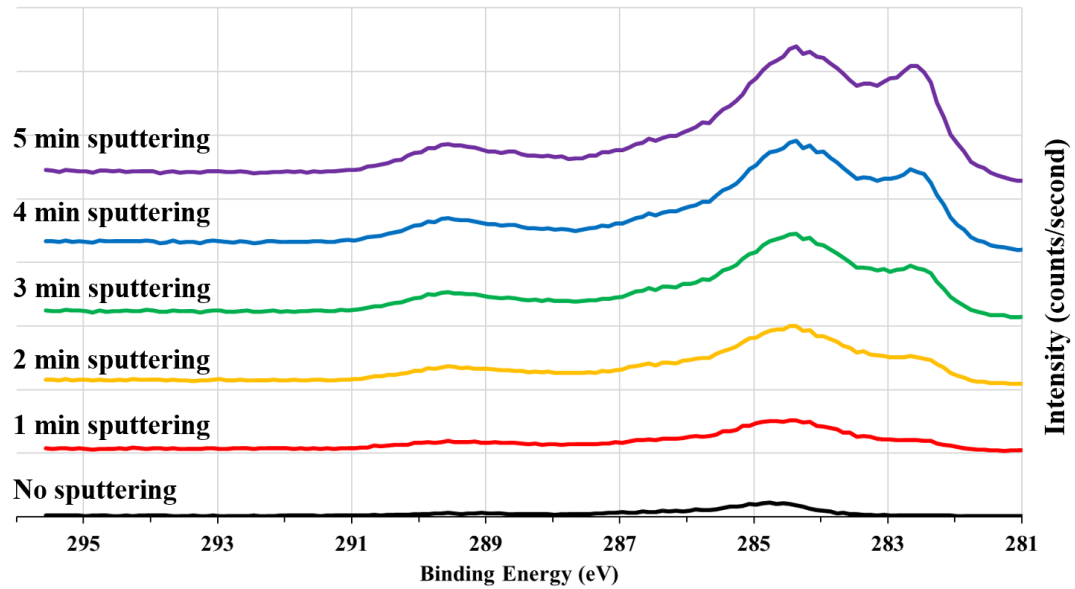


Figure 53: C1s spectra during Argon ion sputtering. Each minute of sputtering is equivalent to the removal of 8 nm of SiO₂.

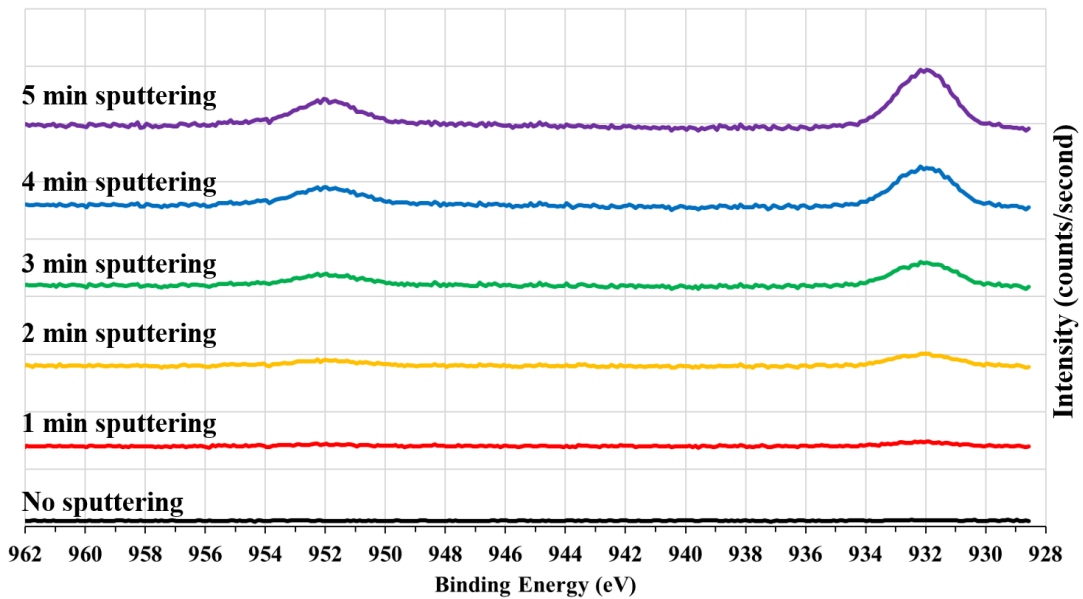


Figure 54: Cu2p_{3/2} spectra during Argon ion sputtering. Each minute of sputtering is equivalent to the removal of 8 nm of SiO₂.

A closer examination of the spectra of C1s and Cu2p_{3/2} is given in Figure 55 and Figure 56, respectively. The location and full width at half maximum of the Cu2p_{3/2} peak is consistent with Cu₂O seen in previous samples; however, a strong Cu(OH)₂ peak is not seen. This is consistent with the other 0.25 V cells examined.

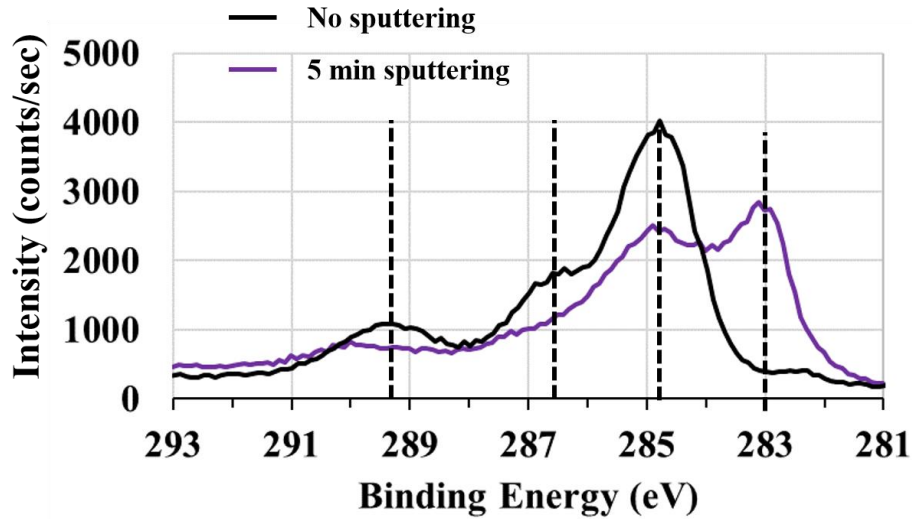


Figure 55: C1s spectra before and after sputtering.

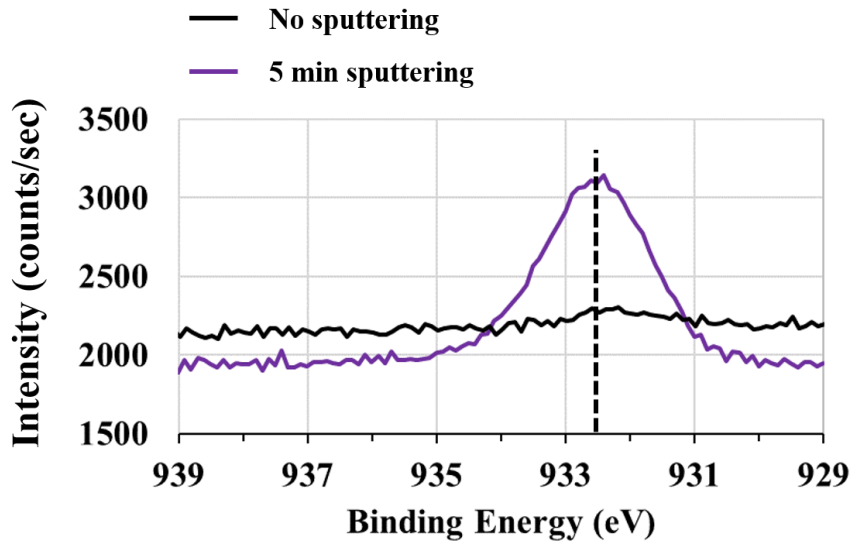


Figure 56: Cu2p_{3/2} spectra before and after sputtering.

XPS measurements were taken on negative electrodes collected from full coin cells described in section 4.3.7. The purpose of this measurement was to identify whether the copper changed chemical state as a result of recharge. The C1s and Cu2p_{3/2} spectra are shown in Figure 57 and Figure 58, respectively. As seen in the figures, a copper peak occurs around 932.2 eV with a full width at half maximum of 1.6 eV. While this occurs at a slightly lower binding energy than before, the lack of satellite peaks rules out CuO or Cu(OH)₂, and the full width at half maximum is more consistent with Cu₂O than Cu.

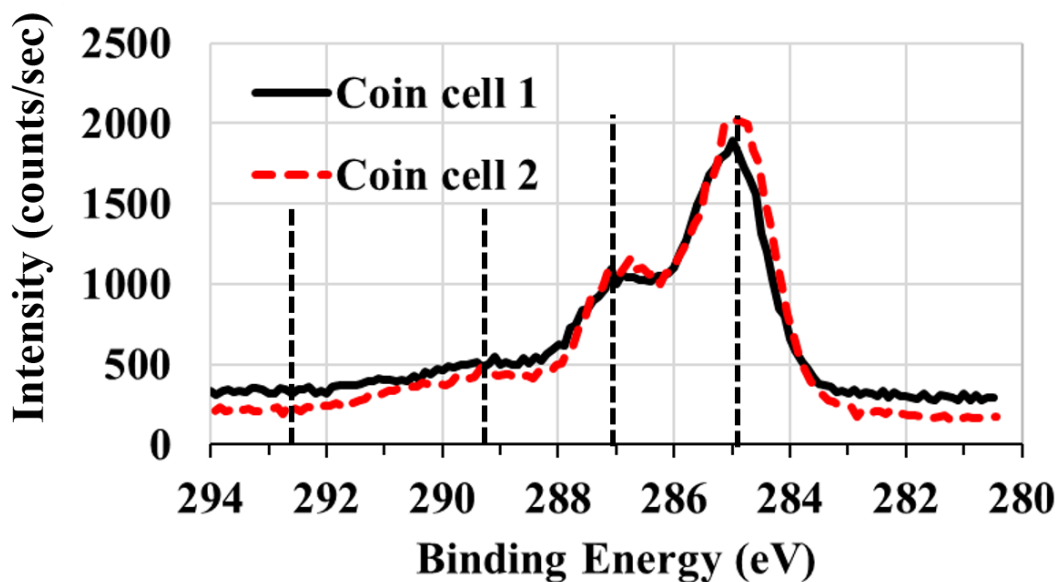


Figure 57: C1s spectra from a charged negative electrode

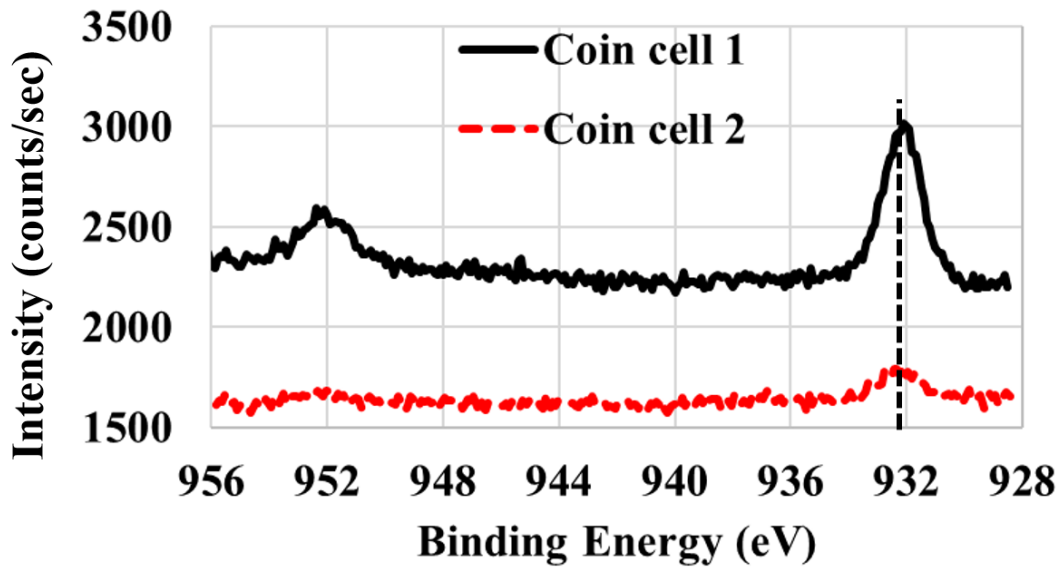


Figure 58: Cu_{2p3/2} spectra from a charged negative electrode

4.4.5 – XAFS

Data analysis is performed on the XAFS data using the Athena and Artemis programs within the Demeter software package [123]. The Athena program enables importing the raw data from the XAFS experiment, pre-edge and post-edge background subtractions, energy scale alignment, and calibration based on the reference foil spectra. The Artemis program allows for simulations of electron scattering within the sample to simulate the extended x-ray absorption fine structure. Analysis focused on both the X-ray absorption near edge structure (XANES) and the extended X-ray absorption fine structure (EXAFS).

The XANES spectra for potential copper compounds is given in Figure 59. The XANES region consisted of the energies immediately adjacent to the K-Edge jump. Clear differences in the XANES region are evident in the plot and can be used to aid in species identification. Figure 60 contains the normalized XANES data for

the overdischarged cells and illustrates slight differences in the features preceding the edge jump. The differences between the samples are minimal, suggesting that the samples contain the same copper compounds in different concentrations. For both of the 0.25 V samples, the XANES data overlapped and future plots will only feature one of the 0.25 V cells for clarity. For each sample, 3 XAFS measurements were conducted on the different locations within the cell (exterior, middle, interior). The spectra were averaged together for all analyses; however, the measurements were repeatable as illustrated in Figure 61. The separate spectra are nearly identical suggesting that the sample is sufficiently homogenous when examining the bulk over a large cross section. Even cells that were recharged exhibited nearly consistent XANES spectra, although some variations are evident in Figure 62.

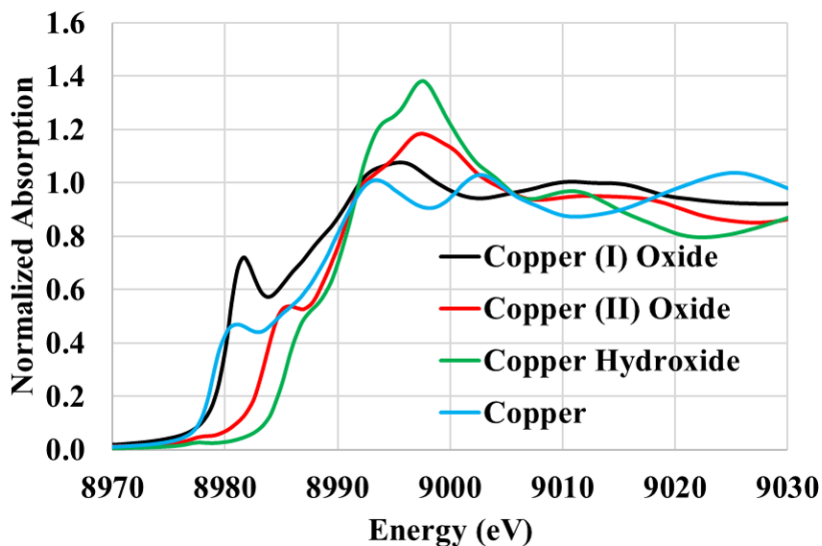


Figure 59: XANES spectra for relevant copper compounds.

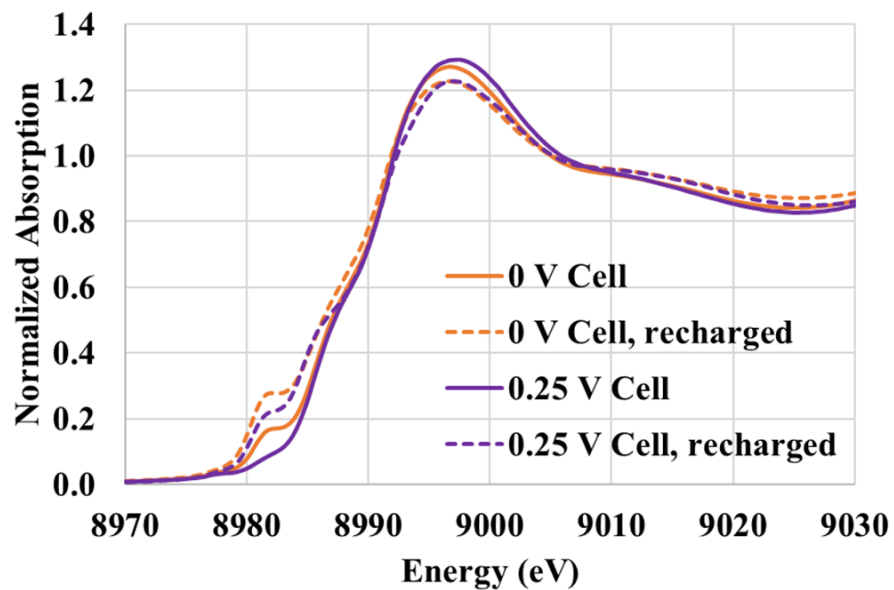


Figure 60: X-ray absorption near edge structure for overdischarged cells

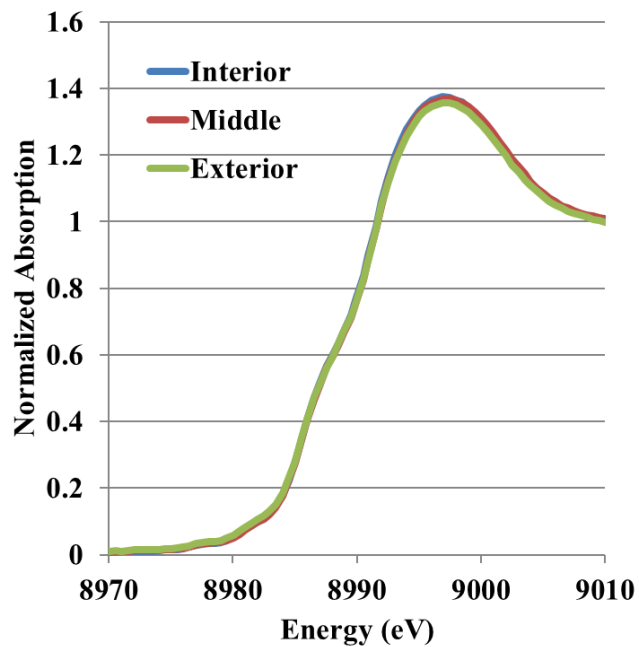


Figure 61: XANES spectra for multiple locations within a cell overdischarged to 0.25V

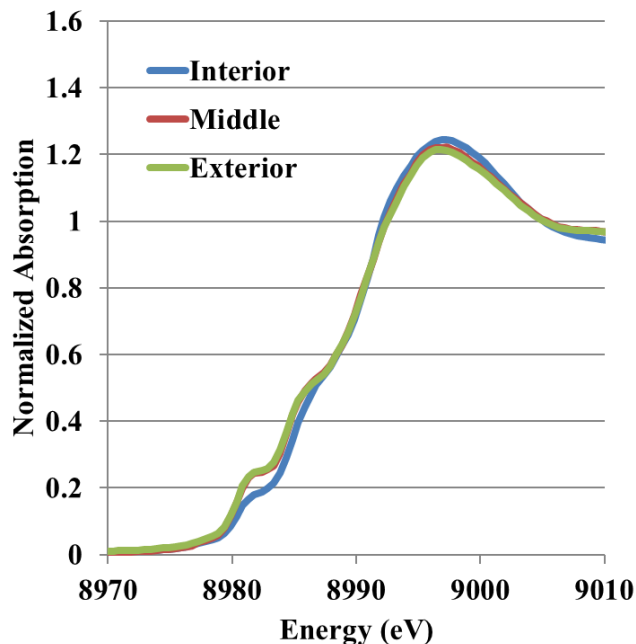


Figure 62: XANES spectra for multiple locations within a cell overdischarged to 0.25 V and recharged prior to disassembly.

The transmission data can also be used to ascertain the relative loading of copper in the samples by comparing the magnitude of the edge step. Table 6 illustrates that the transmission edge step increases in magnitude as the voltage decreases. A reference healthy cell (2.5 V) and the cells overdischarged to 0.5 V had transmission edge steps several orders of magnitude less than the cells overdischarged to either 0.25 or 0 V. This observation furthers the XPS observations that 0 V cells exhibited increased relative concentrations of copper.

Table 6: Transmission edge steps of the cell samples

Cell #	Voltage	Recharged?	Edge Step
1	0	N	0.0722
2	0	Y	0.0873
3	0.25	N	0.0165
4	0.25	N	0.0131
5	0.25	Y	0.0169
6	0.5	Y	0.0002
7	2.5	N/A	0.00002

Comparing the spectra from Cell 1 (0 V overdischarge) to the reference samples of Cu_2O and $\text{Cu}(\text{OH})_2$ illustrate that the sample exhibits traits of both species. In the left plot in

Figure 63, the pre-edge shoulder labeled “A” mirrors the same feature seen in Cu_2O . Furthermore, the right plot is the 1st derivative of absorption, which more clearly demonstrates contributions from $\text{Cu}(\text{OH})_2$ in the peaks labeled “B” and “C.”

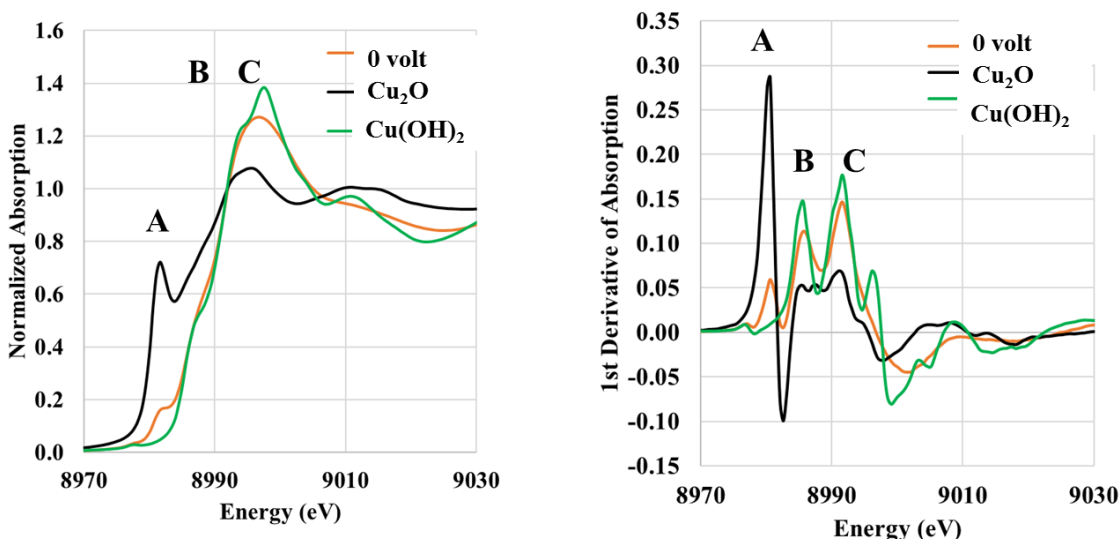


Figure 63: Comparison of sample from 0 V cell to the reference spectra of Cu_2O and $\text{Cu}(\text{OH})_2$. Peaks labeled “A” through “C” on the left (XANES) and right (1st Derivative of XANES) are associated with peaks in the reference compounds.

In addition to the XANES data, observations of the EXAFS data are consistent with the presence of Cu_2O and $\text{Cu}(\text{OH})_2$ as well. In Figure 64, the 0 volt cell is compared to the reference compounds of Cu_2O and $\text{Cu}(\text{OH})_2$. The main peak located at approximately 1.5\AA corresponds with $\text{Cu}(\text{OH})_2$, however, Cu_2O overlaps quite a bit for the other peaks. Further analysis is required to understand the degree to which Cu_2O is present compared to $\text{Cu}(\text{OH})_2$.

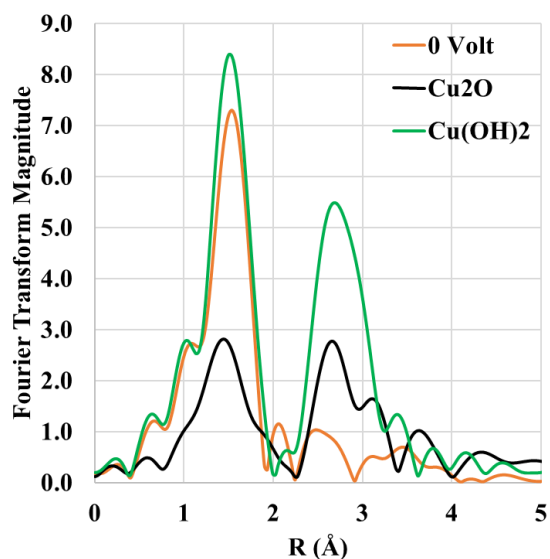


Figure 64: Fourier transform of EXAFS data. All samples exhibit similar traits, with differences in the peak magnitudes. Comparing a sample (0 V) to the reference EXAFS of Cu₂O and Cu(OH)₂.

To further support this hypothesis, model fitting was performed in the Artemis software package [123]. The EXAFS model equation is given as:

$$\chi(k) = S_o^2 \sum_i N_i \left(\frac{f_i(k)}{kR_i^2} \right) e^{-\frac{2R_i}{\lambda(k)}} e^{-2k^2\sigma^2} \sin(2kR_i + \delta_i(k))$$

with S_o^2 representing the many body amplitude reduction factor, N representing the coordination number, R representing the distance to neighboring atoms, and σ representing disorder. Scattering paths for Cu₂O and Cu(OH)₂ were considered to be the main contributors to the copper signal observed in the samples. The model assumes that all samples contain the same two copper compounds in varying concentrations. This assumption is consistent with results seen in both the XANES and EXAFS spectra. Feff, a scattering path calculation tool within the Artemis package, was employed by inputting crystal structure data for Cu(OH)₂ and Cu₂O

[125, 129]. A summary of the crystal structure data can be found in Table 7. The contribution from Cu₂O is limited to the first shell which consists of 2 oxygen atoms at a distance of 1.83 Å and the contribution from Cu(OH)₂ was limited to 4 oxygen atoms at 1.96 Å and one oxygen atom at 2.36 Å. The many body amplitude reduction factor was constrained to the value derived from fitting the Cu reference data, and it was assumed that the disorder and distance between atoms for the Cu₂O and Cu(OH)₂ phases are the same for all the electrode samples. The only parameters that were allowed to vary from sample to sample were the fraction of copper attributed to Cu₂O and the fraction attributed to Cu(OH)₂ while constraining the total fraction to 1.0. The model agreed quite well with the experimental data as seen in Figure 65, and supports the assumption that Cu₂O and Cu(OH)₂ are sufficient to explain the overall negative electrode sample response. The fitting parameters for all of the samples can be seen in Table 8. The fraction of copper in Cu₂O and Cu(OH)₂ was converted to mole fraction and is given in

Table 9.

Table 7: Crystallographic data for Cu₂O and Cu(OH)₂ used for simulations in Artemis

	Space Group	a	b	c	α	β	γ		X	Y	Z
Cu ₂ O	P m -3	4.217	4.217	4.217	90	90	90	Cu	0.25	0.25	0.25
								O	0	0	0
Cu(OH) ₂	C m c 21	2.947	10.59	5.256	90	90	90	Cu	0.5	0.682	0.25
								O	0	0.558	0.253
								O	0	0.799	0.197

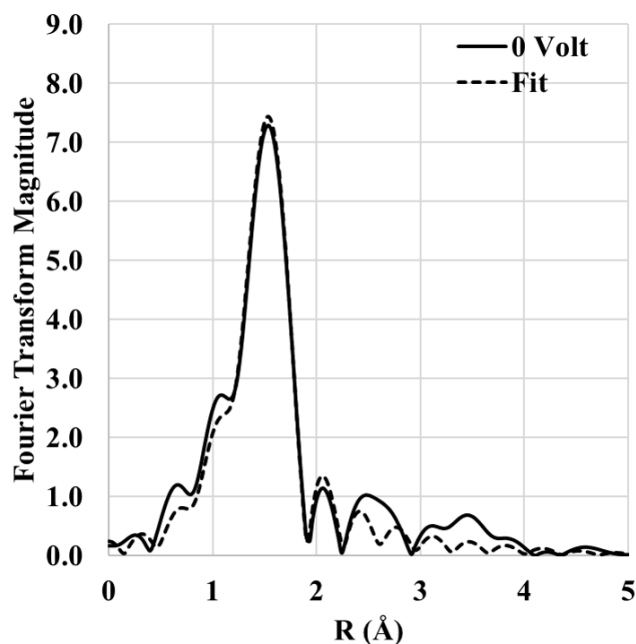


Figure 65: Model fit comparison to a 0 V cell. Close agreement between the experimental and model data indicate that it is sufficient to model the spectra as a linear combination of Cu_2O and $\text{Cu}(\text{OH})_2$

Table 8: Local structure parameters calculated from simulated Fourier transforms of EXAFS spectra for 0.25 V cell (uncertainties reported in parentheses).

	S_0^2	N	R (Å)	σ^2 (Å ²)	E_0 (eV)
Cu(OH)₂	0.86	4	1.939 (0.004)	0.0031(0.0010)	0.5(0.4)
		1	2.335 (0.004)	0.036(0.018)	
Cu₂O		2	1.805 (0.004)	0.0028(0.0014)	

Table 9: Mole fraction of Cu_2O and $\text{Cu}(\text{OH})_2$ for varying storage conditions

Storage Condition	Mole Fraction ($\text{Cu}(\text{OH})_2$)	Mole Fraction (Cu_2O)	R-Factor
0 V	0.869(0.08)	0.131(0.08)	0.0018
0.25 V	0.93(0.11)	0.07(0.11)	0.014
0 V, recharged	0.778(0.07)	0.222(0.07)	0.0020
0.25 V, recharged	0.843(0.09)	0.157(0.09)	0.032

Differences in the mole fraction of $\text{Cu}(\text{OH})_2$ and Cu_2O can be readily observed in the model fitting results. All fits have a low R-factor, which is an

indicator of goodness of fit. Without further samples, it is difficult to definitively say that differences in the mole fraction are a function of the overdischarge level as well as whether or not the cell was recharged. The uncertainties in the mole fractions do overlap; however, the mole fraction of $\text{Cu}(\text{OH})_2$ was consistently higher in 0.25V cells, both between different cells as well as between different locations within a given cell.

It was not possible to resolve the fluorescence data in the positive electrode samples due to the overwhelming fluorescence signal from Ni and Co in the positive electrode. As a result, copper state was not identified via XAFS in the positive electrodes. However, observations of the Ni and Co K-edges allows for the assessment of positive electrode structure changes as a result of overdischarge. Therefore, it is possible to determine whether overdischarge has an effect on the structure and oxidation state of the positive electrode. Figure 66 and Figure 67 show the Co and Ni K-edges, respectively. No changes to the K-edge were observed for overdischarged cells. Significant shifts in the XAFS spectra would indicate a change in oxidation state of the positive electrode active material. Although copper could not be measured on the positive electrode using XAFS, XPS data clearly shows the presence of copper. Rather than affecting the oxidation state of the positive electrode, overdischarge primarily leads to deposition of copper species on the positive electrode.

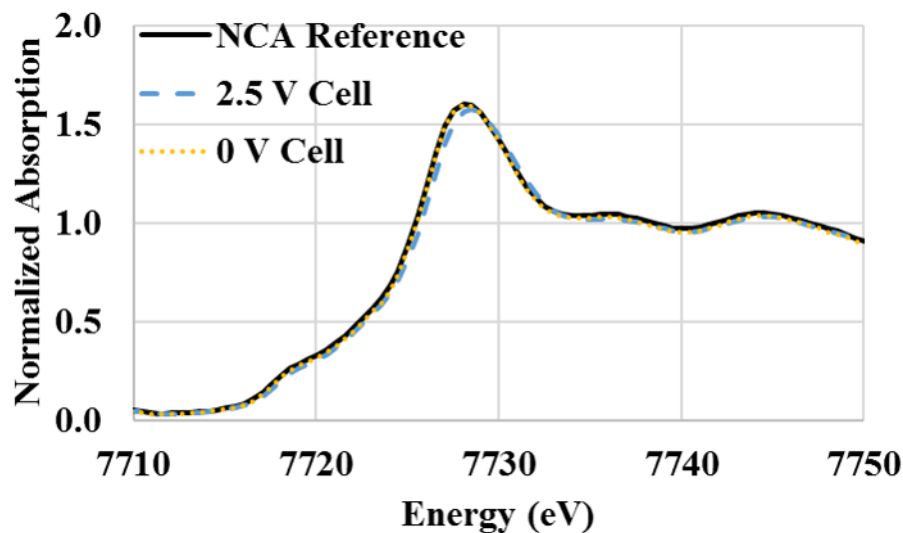


Figure 66: Cobalt K-edge XANES data for a 0 V cell, 2.5 V cell, and the reference NCA powder.

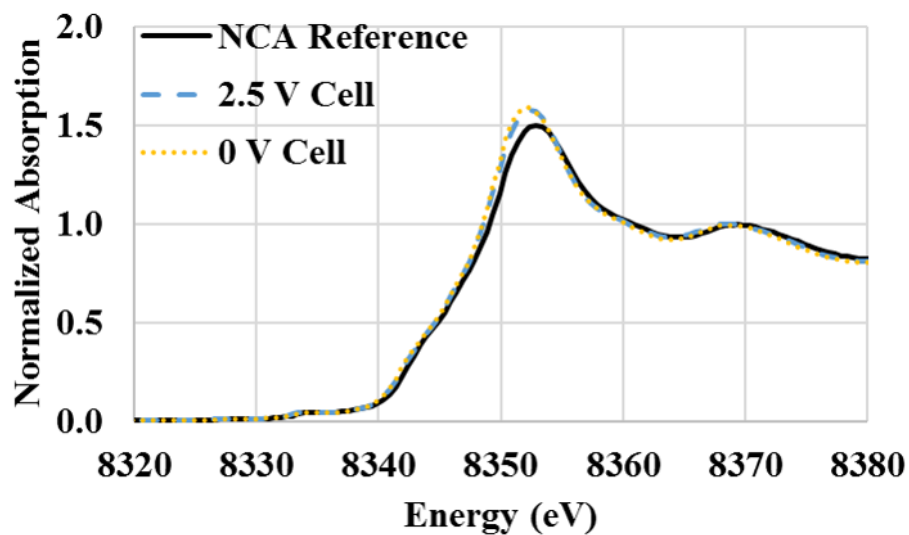


Figure 67: Nickel K-edge XANES data for a 0 V cell, 2.5 V cell, and the reference NCA powder.

4.4.6 – Discussion

The use of multiple analytical techniques to detect and characterize copper dissolution in cells held at low voltages for an extended period of time has allowed

for the identification of copper species and provides greater insight into the likelihood and risk of safety challenges associated with overdischarge of lithium-ion batteries.

For extended periods of storage at low voltages, copper dissolution can occur, and the amount of copper dissolved is a function of the voltage. Cells held at lower voltages tended to exhibit greater concentrations of copper species as determined by XPS and XAS analysis. This is not altogether surprising, as cyclic voltammetry experiments have shown that as the potential of the negative electrode increases, the oxidation current associated with copper dissolution increases as well, leading to higher rates of copper dissolution [106–109]. As a result, any performance or safety implications arising from copper dissolution will be exacerbated at higher negative electrode potentials, and thus at low full cell voltages.

The presence of copper as determined by EDS, XPS, and XAFS on the positive electrode and negative electrode will at best reduce the usable capacity of the cell at a faster rate. This is consistent with literature in which repeated overdischarge leads to a more rapid capacity fade. The most striking observation is that even a single overdischarge event followed by cycling results in accelerated capacity fade. This limits the performance of the cell and can lead to greater self-heating due to the increased impedance.

The copper dissolution can affect the usable capacity in a number of ways. Firstly, the presence of copper can cause accelerated electrolyte decomposition due to inhibited lithium diffusion into the electrodes. Reducing the overall area of the electrode that can participate in intercalation reactions will lead to an apparent loss of capacity. Furthermore, loss of connectivity between the negative electrode and the

copper current collector can reduce the available capacity of the battery and increase cell impedance. Full delamination of the electrode is unlikely due to the electrode stack pressure, however, cyclic stresses caused by repeated intercalation and de-intercalation can lead to isolation between parts of the negative electrode and the current collector. If electronic conductivity is not maintained between sections of the negative electrode and the current collector, a reduced capacity will be observed due to the inability to perform charge transfer reactions. It is difficult to determine the contribution of each of these failure mechanisms and is likely a combination of the two that contribute to the overall capacity reduction. From the XPS sputtering analysis, it is clear that the electrode surface is coated, likely due to SEI formation and electrolyte decomposition. At lower voltages, in which the quantity of copper dissolved is greater, overall capacity fade is greater. The amount of copper dissolved leads to varying degrees of capacity fade. Furthermore, it was qualitatively observed that low voltage cells exhibited reduced adhesion between the electrode and the copper current collector. Delamination of the electrodes from the current collector was apparent during cell disassembly for overdischarged cells. The degree to which this impacts capacity fade cannot be determined at present and warrants further study.

The safety implications of overdischarge, copper dissolution, and copper species deposition relate to increased cell heating and potential for a copper induced short circuit. With a higher cell impedance, ohmic heating during charge and discharge will be exacerbated, potentially placing the cell in greater danger for initiation of thermal runaway. For cells overdischarged to 0 V, higher levels of copper dissolution led to higher rates of capacity fade and increased impedance. Especially

for actions requiring high rate pulse charge and discharge loads, the increased impedance could potentially lead to the cell heating to the point where SEI layer decomposition reactions are initiated ($\sim 90^{\circ}\text{C}$). If SEI layer decomposition reactions are initiated, it is possible for the cell to enter into thermal runaway when the heat generation cannot be dissipated sufficiently.

While overdischarge into reversal has been shown to cause metallic copper plating on the positive electrode, the cell is at a significantly low state of charge to prevent initiation of thermal runaway, and researchers have shown that cells will cease to function and temperatures may rise; however, thermal runaway has not been reported. Short-circuiting at a low state of charge will likely not result in enough heat to cause an escalation in the heat generation. A potential scenario that could result in significant heat generation and thermal runaway involves the formation of conductive copper species while the cell is at a high state of charge. This would occur if the dissolved copper were reduced upon recharge to form metallic copper. While this possibility cannot be completely eliminated by the research conducted in this study, it does not appear to be a high probability failure mechanism; however, the severity of a copper short circuit warrants caution with recovery of overdischarged cells. XPS and XAS analysis of all samples never revealed metallic copper under the tested conditions. While XAS did involve air exposure, XPS was conducted under inert gas protection at all stages of disassembly, transport, and sample transfer. The glovebox environment was consistently at less than 1 ppm O_2 during disassembly and sample preparation. While the copper likely exists as nano-sized particles, oxidation in the glovebox environment would not preclude the detection of metallic copper, especially

for a bulk analysis technique such as XAS. The surface of copper nanophase particles will readily oxidize; however, analytical techniques such as XAFS and XRD will still detect metallic copper. In [126] the in-situ XAFS measurements are performed on a sealed optical electrochemical cell that utilizes copper fluoride as a conversion material cathode. In this electrochemical system, copper fluoride undergoes a conversion reaction to form nanophase metallic copper. While this measurement takes place for a sealed cell, the seal is not perfectly airtight and leakage of electrolyte is observed during the experiment. The environment inside of the cells cannot be more pure than a glovebox environment, and metallic copper is still detected via XAFS. In [127], nanophase copper particles were recovered from copper-containing waste etchants and studied using a variety of analytical techniques including XAFS, XPS, and XRD. The existence of both Cu(0) and Cu(I) was shown. In [128], a technique for removing the oxide coating of copper nanoparticles is proposed. Powder x-ray diffraction (PXRD) analysis detected both copper metal and cupric oxide before any surface modification was performed. If metallic copper is present in the overdischarged cell samples, it should have been detected by XAS analysis; however, the presence of Cu^{2+} and Cu^+ ions in the electrolyte of overdischarged lithium-ion batteries still presents the possibility for the formation of metallic copper and safety concerns cannot be dismissed without further investigation and assessment of risk acceptance levels.

Chapter 5: Overcharge of lithium-ion batteries

5.1 – Literature Review

Overcharge of lithium-ion batteries leads to a number of failure mechanisms detailed in Chapter 3. For mixed metal oxide and spinel positive electrodes (i.e. LCO, NCA, NMC), overcharge leads to destabilization of the crystal lattice and release of oxygen gas. Olivine positive electrodes (i.e. LFP) do not release oxygen when overcharged, but experience the same effects that other chemistries exhibit, including decomposition of the electrolyte, heat generation, SEI layer decomposition, and reactions between the electrodes and the electrolyte. When sufficient gas is generated, the internal pressure of the cell will rise and eventually either a vent will burst or the cell casing will be breached. The introduction of aerosolized electrolyte and combustible gases into the environment can then result in a catastrophic failure. The literature on the overcharge mechanism primarily focuses on the gas species released after a cell's casing has been breached. The progression of gas generation and pressure build-up as a cell is overcharged has not been reported.

Kong et al. [86] assembled cells with LiCoO_2 , LiMn_2O_4 , and LiFePO_4 positive electrodes and examined differences in gas generation under normal and abusive operating conditions. The negative electrodes were all graphite-based, and the cells were encased in a flexible pouch. The cells were then put into a rigid casing with a hole drilled in the top for extraction of the gas species. The cells underwent an initial formation charge cycle and then were cycled 3 more times in the standard operating range. Afterwards, some cells were overcharged, while the remainder rested at their maximum voltage level. The gases formed during battery operation were collected

using a syringe, and the composition of the gases was determined using gas chromatography and mass spectroscopy. Under normal operating conditions, the composition of gases was the same regardless of the positive electrode chemistry. However, under overcharge conditions, the different positive electrodes produced a larger variety of gases. The study did not look at quantifying the amount of gas generation, but identified that LiCoO_2 is the most unstable positive electrode and LiFePO_4 is the most stable.

Kumai et al. [120] measured the volume of gas generated when a LiCoO_2 positive electrode and graphite negative electrode cell was cycled within its standard operating voltage range, when the battery was overcharged, and when the battery was overdischarged. After the cycling tests, the battery was placed in an apparatus where the top of the cell was penetrated with a needle and the volume and composition of the gas could be measured. Cells cycled in the nominal range for a total of 2000-3000 cycles exhibited a reduction in capacity of 50%. For these cells, the total gas volume varied between 1.7-2.8 mL. Mostly methane gas was detected, but other hydrocarbon based gases were also present in smaller quantities. This indicated that electrolyte decomposition does occur even under normal operating conditions. The overcharged cell produced 10.57 mL of gas, with a larger quantity of oxygen and carbon dioxide was present as a result of the positive electrode decomposition. The overdischarged cell produced 40.21 mL of gas, and was attributed to the electrolyte decomposition at low cell potentials. The overcharge and overdischarge tests were only performed on 1 cell each; therefore, variation in gas volume and gas species is unknown.

Ohsaki et al. [133] overcharged lithium-ion cells and extracted gas at 5 different stages of overcharge. The amount of gas generated initially was small (< 1 mL). As the state of charge and the temperature increased, gas volume increased (~ 20 mL). Gas generation and composition was measured at discrete times on different cells due to the cell sampling methodology.

Leising et al. [134] performed abuse testing of lithium-ion batteries, and measured the thickness change of the batteries after significant swelling occurred. They overcharged a 1.5Ah LiCoO₂ positive electrode and graphite negative electrode cell at 1.5 Amps and observed cell rupturing after the battery rapidly increased from 5.5 Volts to 12 Volts. At charge rates less than 0.3 Amps, the cells swelled significantly, but did not rupture. Thickness measurements were taken at the most swollen region of the cell, and a thickness increase of 1.04 cm (an 80% increase) was observed. This thickness increase was related to an internal pressure of over 300 psi through additional hydrostatic pressure tests on empty cell casings.

Roth et al. [135] performed overcharge, short circuit, and elevated temperature tests and found that reactions between the solvent, lithium salt, and electrodes were the main contributors to gas generation. They estimated a total release of 12–30 mL of gas through measurements of gas pressure either after the cell vented or by puncturing cells that did not vent. No continuous pressure measurement was conducted.

Fernandes et al. [136] overcharged 26650 form factor LFP cells inside of a custom enclosure that allowed for gas sampling following venting or bursting of the cell. The study focused primarily on gas analysis using either FTIR or gas

chromatography with a thermal conductivity detector (TCD). The overcharge tests showed repeatable behavior of the cell's voltage indicating an initial increase in the cell voltage to 5.5 V, followed by a decrease to approximately 4.75 V. The voltage then increases to match the overcharge power supply when failure occurs. The researchers found that the overall volume of gas released during the tests was on average 645.8 mL, which is significantly larger than other researchers. The authors attribute this difference to the nature of their test setup (air was continuously replenished in the vessel) and the outcome of the test (complete thermal runaway and combustion).

Belov [137], overcharged lithium-ion cells at several rates, however, the voltage and temperature profiles were the only observations made during testing. Overcharge rate did not significantly affect the state of charge at which the cell failed, with failure occurring at approximately 205% SOC for 1C C-Rate, 203% SOC for 2C C-Rate, and 201% SOC for 3C C-Rate. During the overcharge abuse, the voltage first increases before reaching a local maxima. The voltage slightly decreases and plateaus before rapidly increasing as the battery enters into failure. No measurement of gas species or gas pressure was reported.

A large number of studies focus on thermal abuse of lithium-ion batteries; however, the failure mechanisms will be different than overcharge abuse. In thermal abuse, the oxygen generating reactions as a result of crystal lattice instability will not occur, and the first heat generation side reactions will be the breakdown of the SEI layer. Similarly, any pressure or gas species measurements occur after the cell has already vented [138–141]. Coman et al. [143, 144] only reference a single instance of

continuous pressure measurements during a thermal abuse test performed by Ottaway [145], but there are no experimental details contained in the presentation slide detailing the data.

5.2 – Research Gaps

Previous research into the overcharge mechanism of lithium-ion batteries has proposed mechanisms for oxygen release from the destabilized positive electrode, reactions between the electrolyte and the cell components, and decomposition of the electrolyte due to operation outside of its voltage stability window. The collection and measurement of gases is a point-measurement and provides limited information about the rate of gas generation in a cell as it is overcharged. Thus it is impossible to understand the full progression of gas generation and pressure buildup within a cell without a continuous measurement process. By puncturing commercial cells and monitoring internal pressure directly, a continuous pressure profile can be measured and used for modeling purposes or correlated with non-invasive measurements of strain for diagnostics and prognostics purposes. The research in this chapter develops a methodology for an airtight puncture of a cylindrical cell, pressure measurement, and gas sampling capabilities. Stages of pressure increase are identified and correlated with the voltage and temperature profiles of the overcharged cell. The pressure increase is then related back to the failure mechanisms responsible for gas generation in the cell.

5.3 – Experimental

5.3.1 – Cell Puncturing

As described in 4.3.2, CT-scans and destructive physical analyses (DPAs) were conducted and highlighted a region of the cell that was safe to breach without risk of causing a short circuit. This is illustrated schematically in Figure 68. The cell is constructed in such a way that the bottom $\sim 1/2$ " consists of only the positive current collector, which is connected directly to the casing, making the cell case positive. As a result, it is possible to puncture the cell in this region without short circuiting adjacent electrode layers.

A line is marked approximately $1/4$ " from the bottom of the cell and an aluminum collar is placed on the bottom of the cell as illustrated in Figure 69 and Figure 70. The aluminum collar has an inner diameter matching the cell's outer diameter, a chamfered side, and it has a $1/8$ " threaded hole on the chamfered side. Two bolts pass through the collar and are used to clamp the collar onto the cell. A Viton O-ring is placed inside of the threaded hole, and a commercial plumbing saddle valve is wrapped with PTFE tape, threaded into the hole, and tightened until the O-ring compresses against the cell's body. This creates an air-tight seal between the fitting and the cell body. The puncturing mechanism is modular and can be attached to any type of fitting with Swagelok-type connectors. Figure 69 illustrates a setup where gas sampling is possible through a remotely activated solenoid valve. This enables the collection of gases at various points during overcharge, albeit at the expense of potentially influencing subsequent gas pressure and species measurements. Alternatively, Figure 70 is used to measure the internal gas pressure

more precisely with a lower added free volume. In both illustrations, an Omega general purpose PX302 pressure transducer is shown.

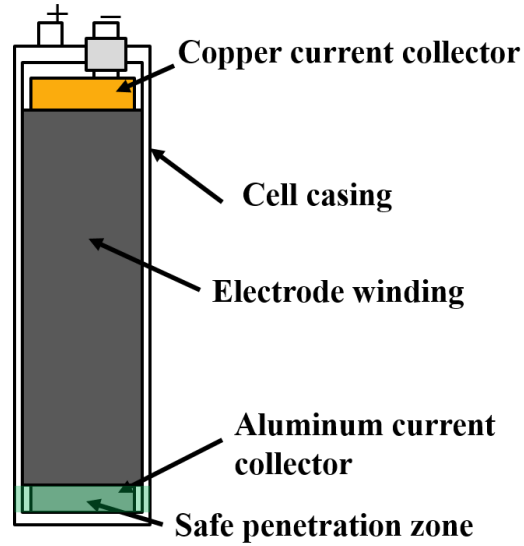


Figure 68: Schematic of cell cross section showing a "safe penetration zone" at the bottom of the cell. The cell is case positive and the only current collector present at the bottom of the cell is also the positive electrode.

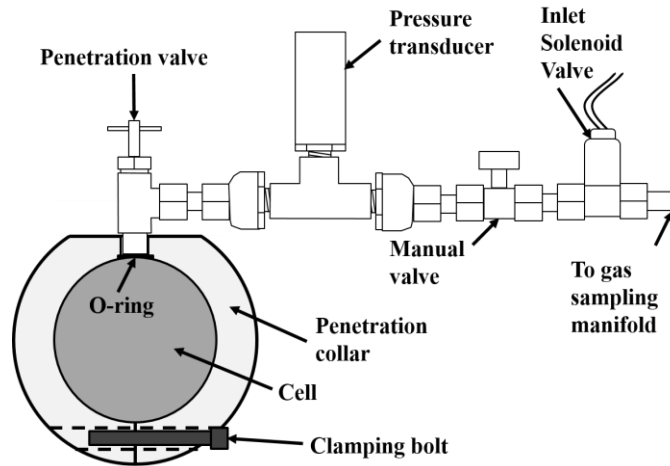


Figure 69: Cell puncturing assembly with option of gas sampling

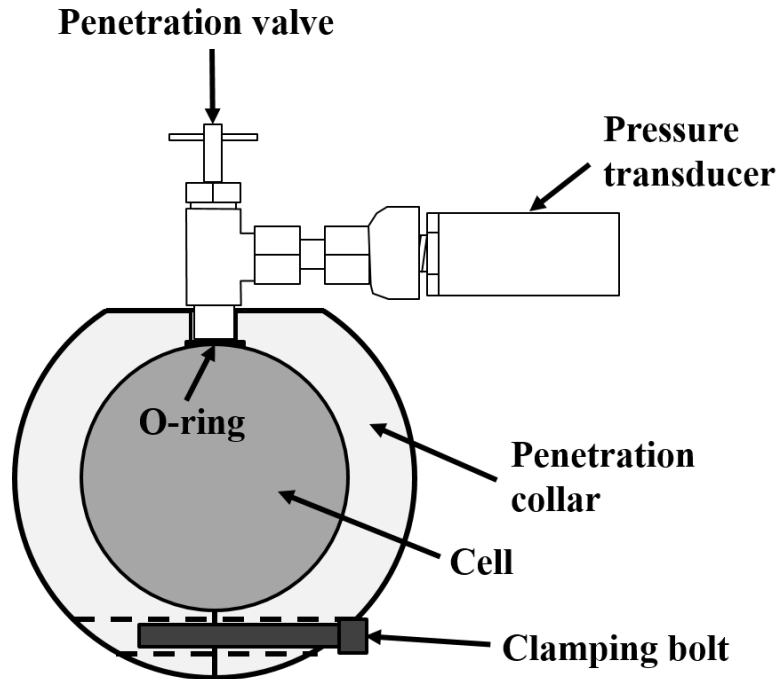


Figure 70: Cell puncturing assembly with limited added free volume

Prior to the beginning of testing, the cell is punctured with the needle by turning the handle on the penetration valve. Puncturing and testing is performed inside of a steel abusive test box located at Naval Surface Warfare Center Carderock Division, measuring 8’x8’x16’ with gas-tight doors and ventilation to the exterior of the building. The cell’s voltage, pressure, and temperature are monitored at a 10 Hz rate to capture sudden changes in any of the quantities. The needle is forced through the cell casing by rotating the handle clockwise and retracted by rotating counterclockwise. The abusive test box is then sealed for testing.

5.3.2 – Overcharge Test

Overcharge testing was conducted on a cell charged to 4.1 V, which corresponds to 100% SOC per the manufacturer. The cell was taped to a cinder block in a horizontal position with glass-fiber tape at the top and bottom of the cell.

Thermocouples were taped to the side of the battery and at the bottom end cap, and an ambient temperature thermocouple was located away from the cell. The cell's current, voltage, internal pressure, and thermocouples were monitored remotely through an Agilent 34970A data acquisition unit at a 1 Hz sampling rate. The cell's charging current was controlled with a power supply capable of charging at up to 30 Amps. The overcharge current was measured through a 20 A/50 mV shunt located between the negative cell terminal and the negative side of the power supply. A 24 V relay was placed between the positive side of the power supply and the positive cell terminal to prevent inadvertent charging during setup. The pressure transducer is a 200 psi/100 mV transducer that is powered with a 10 V power supply.

Overcharge was conducted at a variety of constant current rates to induce a continuous loss of oxygen from the destabilized positive electrode. The power supply was set to a high upper voltage (12 V) and the current was set to either 26 A (C/2 C-rate) or 10.4 A (C/5 C-rate). The overcharge profile is pictured in Figure 71. The voltage of the cell does not monotonically increase during the overcharge procedure due to the initiation of side reactions. Once the cell's temperature is sufficiently high, cell failure is marked by a sudden increase in the measured voltage, corresponding to loss of cell voltage and the Agilent measuring the power supply voltage directly. Once the cell fails, the power supplies are turned off and an overnight stand-down is implemented to allow gases to evacuate.

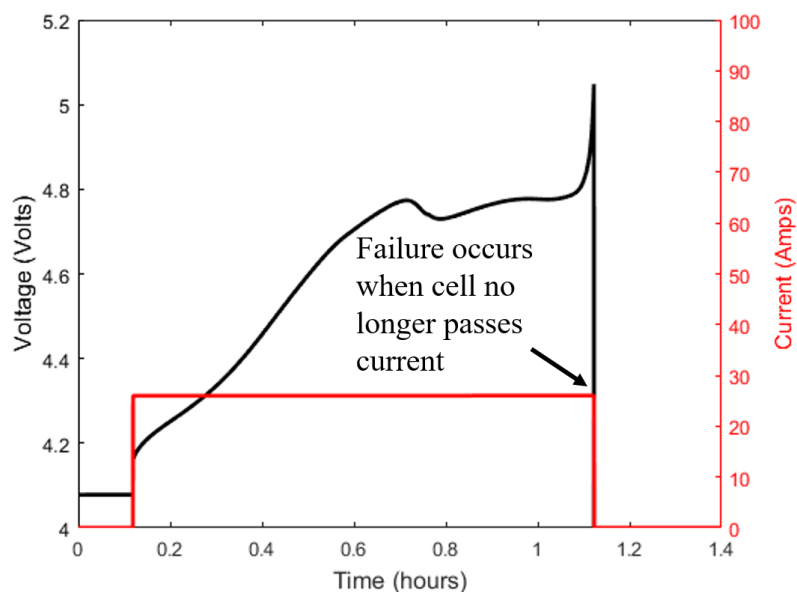


Figure 71: Constant current overcharge test

5.3.3 – Gas Sampling

In experiments where gas sampling was conducted, a gas capture manifold was connected to the penetration valve assembly through a ¼” stainless steel tube. The tube was wrapped in resistively heated tape and held at a temperature of 60°C to prevent condensation of the gases. A picture of the gas collection manifold is given in Figure 72. Each of the sample volumes has an independent solenoid valve and manual valve. All of the sample volumes branch off of the same central junction with one side connected to the cell and the other side connected to a vacuum pump through a solenoid valve. Prior to testing, the main junction is evacuated by opening the solenoid to the pump. This removes air from the system up to the cell’s solenoid valve. The cell’s solenoid valve is opened to remove any background gases. This can be done either before the cell is punctured or after. Next, the individual sample volume solenoids are opened one-by-one to evacuate the rest of the sampling manifold.

Once testing begins, gas builds up within the cell up to the first solenoid valve. When a gas sample is required, the sampling volume solenoid is first opened and vacuum is confirmed. Then the cell's solenoid is opened to draw the gas to the sampling volume. The cell solenoid is then closed, followed by the sampling volume solenoid. Finally, the manifold is evacuated with the pump to create a vacuum for the next sample, if desired. Once the test and overnight standdown is complete, the manual valves are closed and the sampling volumes removed from the assembly for analysis.

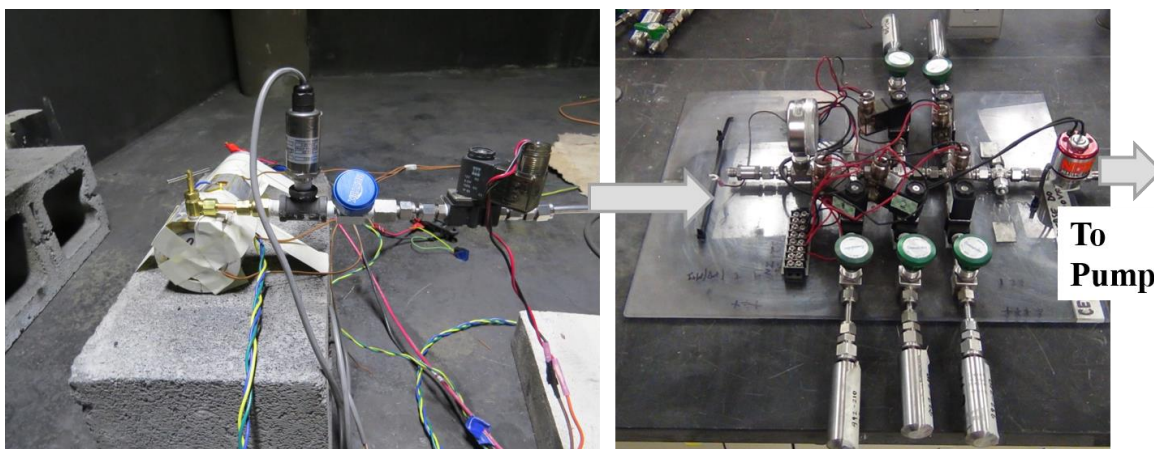


Figure 72: Cell with puncturing mechanism, pressure transducer, and solenoid valve (left) and gas sampling manifold (right)

5.3.4 – Gas Analysis

Gas analysis was conducted at Naval Surface Warfare Center Indian Head Explosive Ordnance Disposal (EOD) Technology Division using their Agilent gas chromatography/mass spectrometry (Agilent 7890A GC and 5975C MS). Gas chromatography (GC) utilized an HP-PLOT Q column, which is a bonded polystyrene-divinylbenzene (DVB) column that specializes in separation of hydrocarbons, CO₂, air, and solvents. This tube is particularly well-suited for

studying lithium-ion batteries because of the diversity of gases reported in the literature that fit into these categories. The gas samples were manually injected into the GC and the carrier gas was Helium. The GC column is housed within a programmable oven. The oven is set to start at 40°C, increase at 10°C/minute until a temperature of 200°C is reached, held at 200°C for 1 minute, and then increased at 15°C/minute until a temperature of 250°C is reached, and held at 250°C for 8 minutes. Once the carrier gas and the gas sample travel through the column, the gases interact with the stationary phase, causing the different gases to elute at different times. The combination of the column coating and a programmed heating profile allows for sufficient separation of gas species to resolve the separate gas peaks in a chromatogram. At the end of the column, the gases are sent into a mass spectrometer (MS). The samples are ionized and sorted by mass to charge ratio. The combination of GC/MS allows for the identification of unknown compounds and their relative abundance in mixed gas samples.

To preserve the integrity of the samples and avoid contamination with air, the sample containers were attached to the apparatus seen in Figure 73. The upper part of the apparatus contains an argon purge line with a ball valve, a vacuum line with a ball valve, and a septum sample port for transferring samples to the GC/MS equipment. At the bottom, each sample container is connected to this apparatus. Once the sample is connected to the apparatus, argon gas is fed into the upper portion of the apparatus. The argon valve is closed, and the vacuum valve is opened so that the upper portion of the apparatus is evacuated. This process is repeated 3 times to ensure that no air is present in the system. Prior to opening the sample valve, the upper portion of the

apparatus is evacuated, and both the argon and vacuum valves are closed. The sample valve is then opened, drawing the gas from the sample cylinder into the apparatus. An airtight syringe is inserted into the sample port, used to collect a 10 μL sample, and injected directly into the GC/MS equipment. Multiple samples are collected from each sample container to ensure repeatability of the analysis.

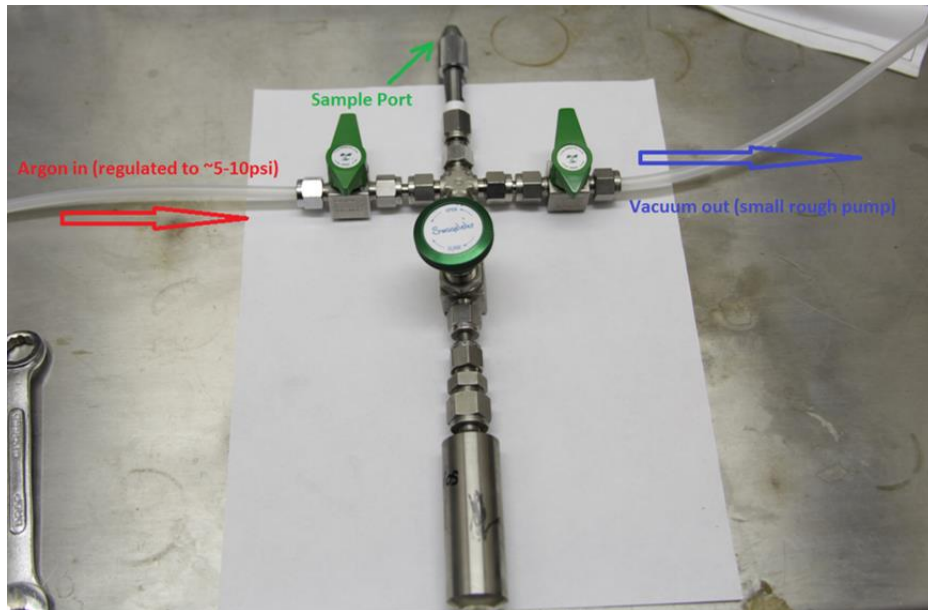


Figure 73: Gas sample extraction using an air-tight GC/MS syringe

5.4 – Results

5.4.1 – Overcharge with multiple gas samples

A total of three (3) cells underwent overcharge testing with multiple gas samples pulled during the course of the overcharge test. Cell failure occurred at various times between 48 and 72 minutes. Variability between the different cells seems to be partially due to the number of gas samples taken.

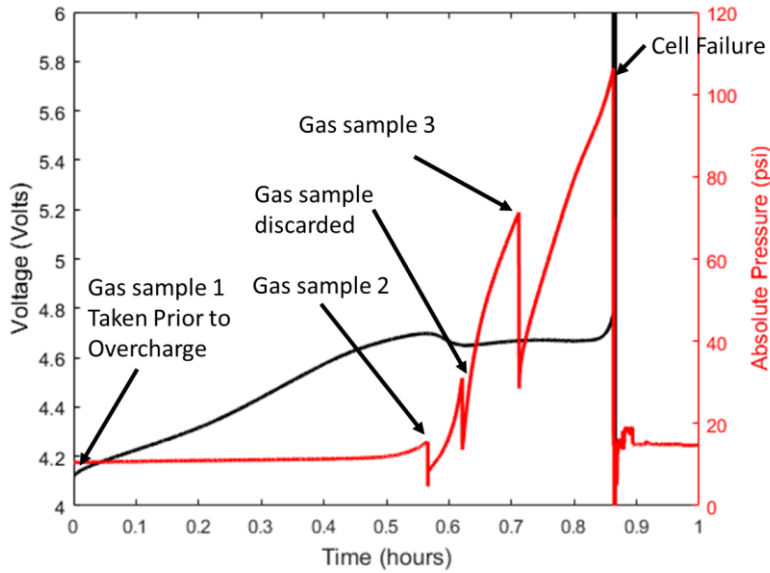


Figure 74: Pressure and voltage plot for cell 1.

The voltage and pressure plots for cell 1 are shown in Figure 74. The cell's internal pressure began to rise before the plateau in voltage, and a gas sample (sample # 2) was captured at 4.7 V before the decrease in voltage. After gas sample #2 was taken, the pressure began to rise again, and an additional sample was taken at 32 psi (absolute). This test only included 3 gas sampling canisters, and as the pressure continued to rise, the final sample was discarded by re-evacuating the sampling canister. Sample #3 was taken when the pressure reached 71 psi (absolute). The cell continued overcharging until it reached failure and rapidly disassembled. The failure occurred at the terminal end of the cylinder again as seen in Figure 75.



Figure 75: Failed cell with ejected terminal end and electrode jelly roll.

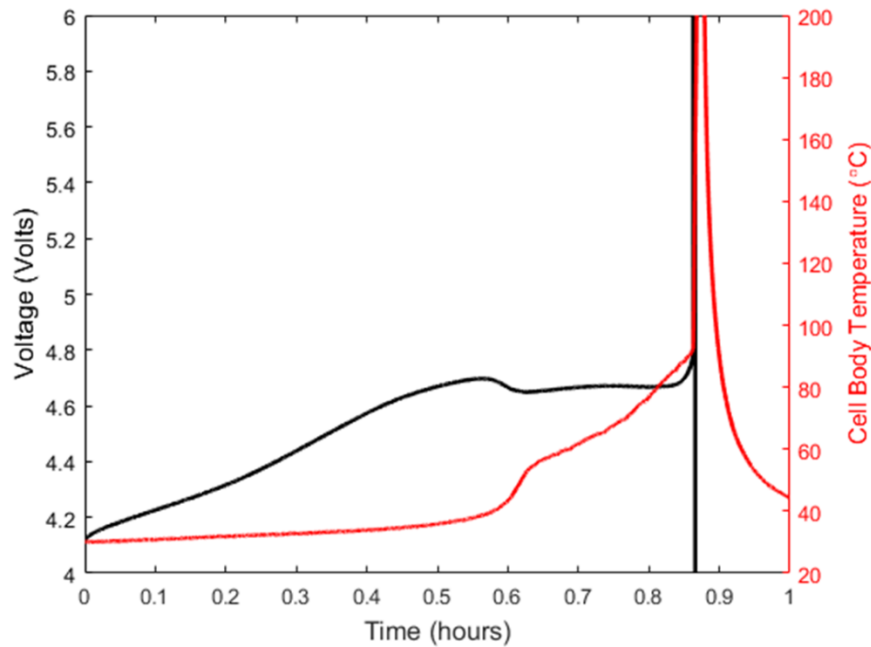


Figure 76: Temperature on side of cell 1 during overcharge.

The temperature plot in Figure 76 demonstrates that the temperature increase can be described by 4 phases. The first phase is a fairly linear increase ($\sim 0.2^{\circ}\text{C}/\text{min}$) in temperature during the first 30 minutes as the voltage increases to 4.7 V. The next phase is a steeper increase in temperature ($\sim 6^{\circ}\text{C}/\text{min}$) during the time the voltage is decreasing and starting to plateau. The third phase is an intermediate increase in temperature ($\sim 2.6^{\circ}\text{C}/\text{min}$) up until failure. The final phase is a rapid increase in

temperature above 200°C as the cell is failing. The bulk of the pressure growth occurs during the 2.6°C/min temperature increase as the cell voltage remains largely flat (phase 3). This supports the case that gas generating side reactions are occurring, likely from the destabilization of the mixed metal oxide positive electrode and oxidation of the electrolyte.

Sampling gas from cell 1 helped shed light on opportune times to sample gases during overcharge. Additional sample containers were added to the gas sampling manifold so that 5 gas samples could be collected for cell 2. Figure 77 shows the voltage and pressure data from cell 2. Similarly to previous tests, pressure begins to rise as the voltage peaks and decreases slightly. Gas sample # 2 was taken immediately following the peak in voltage at a pressure of 33 psi (absolute). Gas sample # 3-5 were taken at pressures of 45, 75, and 105 psi (absolute). Approximately 4 minutes after the final gas sample was taken, the cell underwent thermal runaway with spontaneous disassembly. The pressure at the time of failure was 95 psi (absolute). The cell's terminal end was ejected; however, the electrode jelly roll remained inside the cell for the most part as seen in Figure 78. Some small ribbons of copper current collector did get thrown from the cell, but it is minimal compared to previous tests. The precise reason of why the jelly roll failed to eject from the cell is unclear, but it could be due to the location of gas bubbles being closer to the terminal end cap rather than the opposite end of the cell. Pressure buildup at the smooth end of the cell would provide the thrust required to eject the jelly roll from the cell body. Furthermore, differences in the bond between the aluminum current collector and the cell casing could determine whether or not the jelly roll ejects from the cell body.

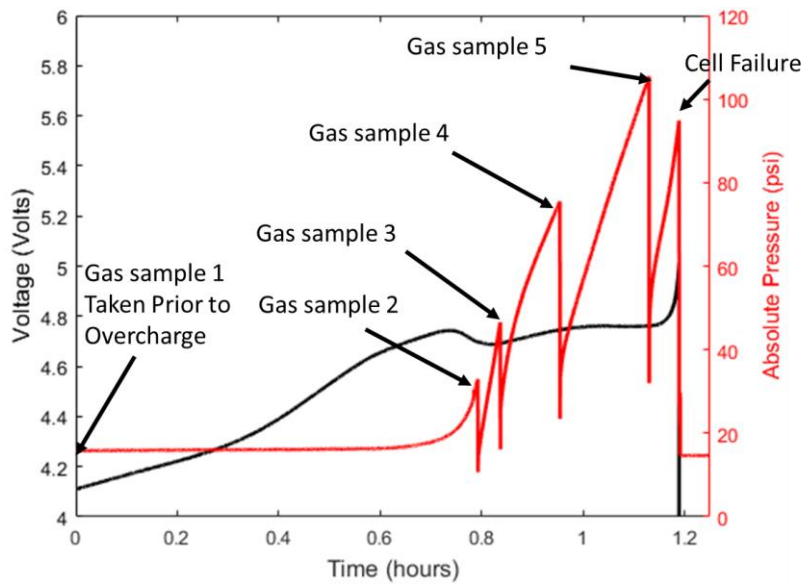


Figure 77: Pressure and voltage plot for cell 2.



Figure 78: Cell 2 following the overcharge test. The majority of the electrode jelly roll remained inside of the cell despite an internal pressure of 95 psi (absolute) immediately prior to failure.

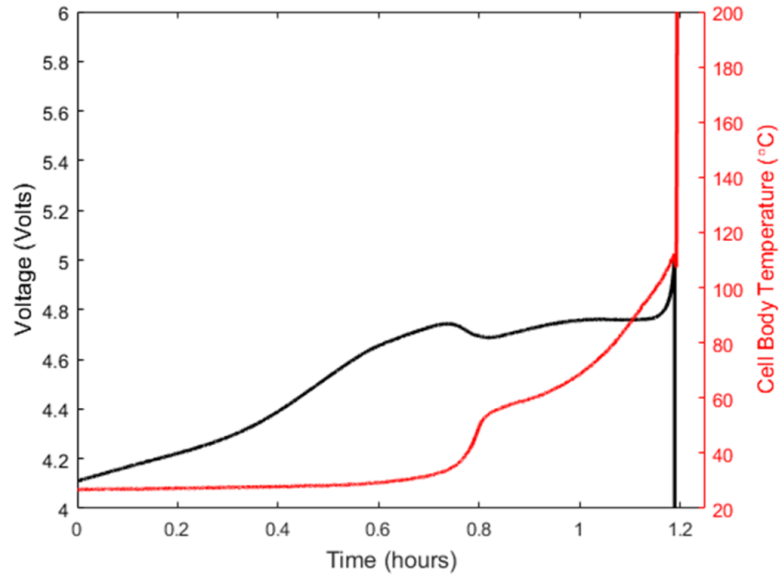


Figure 79: Temperature on side of cell 3 during overcharge.

The temperature on the side of cell 3 demonstrates similar behavior as cell 2 and can also be separated into 4 phases of temperature increase. The shape of the curve, as well as the magnitude of the linearized slopes of the temperature increase per minute, is very similar to cell 2. For cell 3, the phase 1 temperature increase is approximately $0.1\text{ }^{\circ}\text{C}/\text{min}$ compared to $0.2\text{ }^{\circ}\text{C}/\text{min}$ for cell 2. The phase 2 temperature increase is $6.9\text{ }^{\circ}\text{C}/\text{min}$ compared to $6\text{ }^{\circ}\text{C}/\text{min}$ for cell 2. Finally, the phase 3 temperature increase is approximately $2.7\text{ }^{\circ}\text{C}/\text{min}$ compared to $2.6\text{ }^{\circ}\text{C}/\text{min}$ for cell 2. The final phase is a rapid increase in cell temperature $> 200\text{ }^{\circ}\text{C}$, corresponding with cell failure and spontaneous disassembly with fire.

The gas sampling for cell 3 was very similar to cell 2, with the final sample collected only 1 minute prior to failure. The absolute pressure is initially below atmosphere due to the first gas sample pulling the transducer to vacuum. By the time the cell's voltage peaks and decreases, the gas pressure increased above atmosphere, and gas samples 2-5 were captured at 34, 45, 75, and 86 psi (absolute), respectively. Cell 3 failed in the same manner as cell 2, in which the terminal end of the cell was

ejected, but the electrode jelly roll mostly remained within the cell body save for some ribbons of copper current collector as seen in Figure 82.

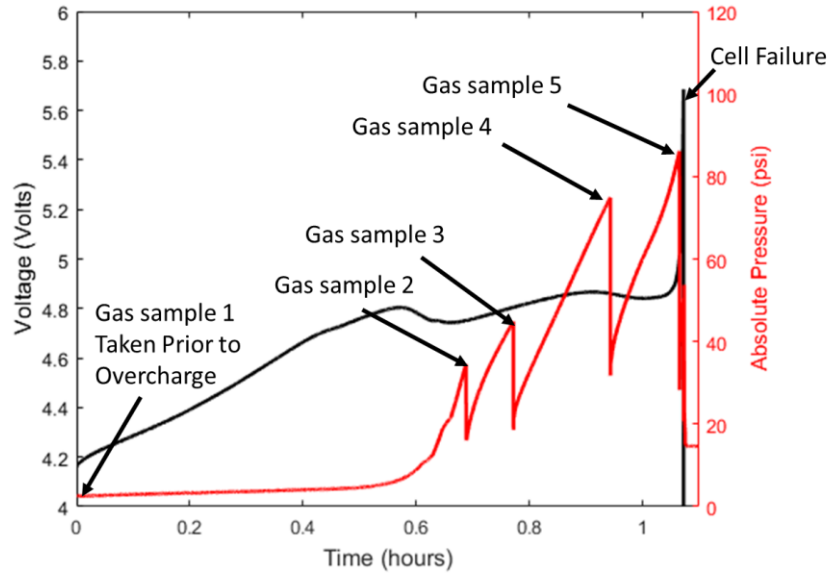


Figure 80: Pressure and voltage plot for cell 3.



Figure 81: Cell 3 following overcharge. The electrode jelly roll mostly remained in the cell except for some ribbons of copper current collector.

The temperature on the side of the cell displayed the same behavior as cells 1 and 2. Phases 1-3 demonstrated linearized slopes of the temperature curve of 0.25 °C/min, 4.5 °C/min, and 2.1 °C/min, respectively.

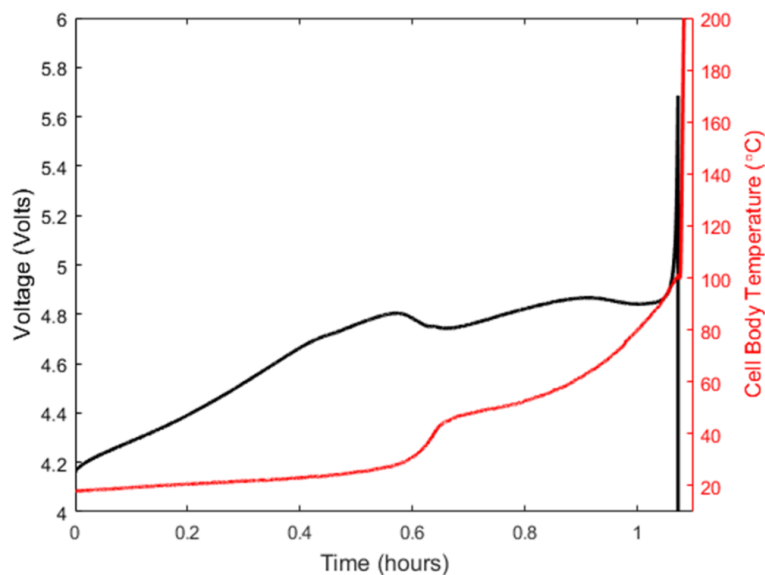


Figure 82: Temperature on side of cell 3 during overcharge.

Analysis of gas species was performed using GC/MS for the three cells. The gas species identified are consistent with literature, particularly the presence of CO, CO₂, O₂, hydrocarbons, and electrolyte vapor. As a sample is overcharged, changes in the chromatogram can be seen in the growth of peaks. The peaks in the chromatogram can then be identified with the MS measurements. Figure 83 shows the chromatogram for cell 2 before overcharge is initiated and during overcharge. As overcharge progresses, generation of gas leads to peak intensity increases and providing insight into the predominant gas species. Variability in the amount and composition of the gas samples can be seen in Table 10. Using integrated peak area as a rough measure of the percentage composition of each gas species, it is possible to identify the main contributors to the gas composition. Some of the cells exhibited a much greater diversity of gas species in the samples; however, the species accounting for the majority of the gas were consistent.

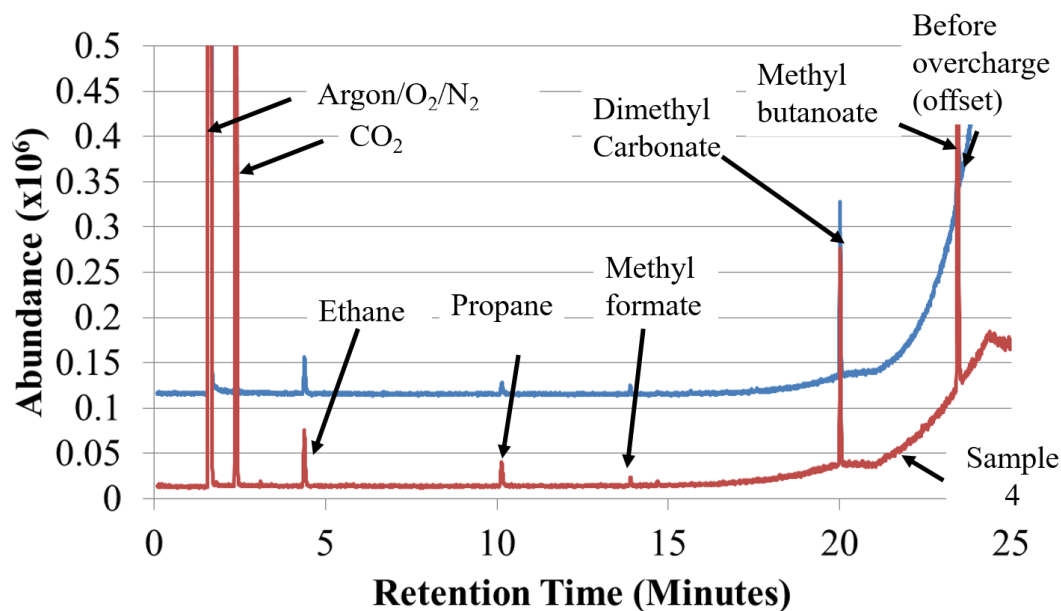


Figure 83: Chromatogram before and during overcharge with the curves offset for clarity.

Table 10: Gas species measured during overcharge at approximately 148% SOC.

Gas Species	Cell 2	Cell 3
O2	66.4	28.7
CO2	27.0	53.6
Methyl Fluoride		0.07
Ethylene		0.018
Ethane	0.36	0.70
Fluoroethane		0.018
Propene		0.014
Propane	0.20	0.38
Cyclopropane		0.023
Dimethyl Ether		0.029
2 Fluoro Propane		0.027
Methyl Formate	0.05	0.16
Butane		0.081
Isobutane	0.04	
Acetone		0.049
Methyl Acetate		0.033
Pentane		0.031
Dimethyl Carbonate	0.95	3.41
Methyl Propionate		0.019
Hexane		0.038
Column Bleed		0.065

Methyl Butanoate	4.95	12.58
------------------	------	-------

5.4.2 – Overcharge with single gas samples

Due to the role that gas samples play in the failure time of the batteries, subsequent tests focused on taking a single sample immediately prior to failure. A graph of two cells overcharged at 26 A until failure is shown in Figure 84. The cell voltage follows a similar path as the cells tested with multiple gas samples. Lack of changes in the voltage profile indicate that gas sampling did not remove significant electrolyte to alter the overcharge voltage profile. Instead, this curve is characteristic of NCA/graphite cells under overcharge conditions. Differences in initial pressure measured is the result of differences in aging between the cells. When puncturing cells, a distribution of cell internal pressures has been observed due to unit-to-unit differences. Despite differences in starting pressure, the overall pressure trend is consistent. Failure also occurs earlier for the cell with greater initial pressure; however, both occur approximately near 150% SOC, which is within the range seen for the samples with multiple gas samples.

The pressure rise due to overcharge does not occur until roughly 125%-130% SOC. At this point, the temperature of the cell has not changed significantly, and it is likely that the manufacturer built in a margin on the positive electrode to prevent release of oxygen from the positive electrode structure unless the battery significantly overcharged. The pressure begins to build at an increased rate over the next 5% SOC after which time the gas generation occurs at a slower, nearly linear rate.

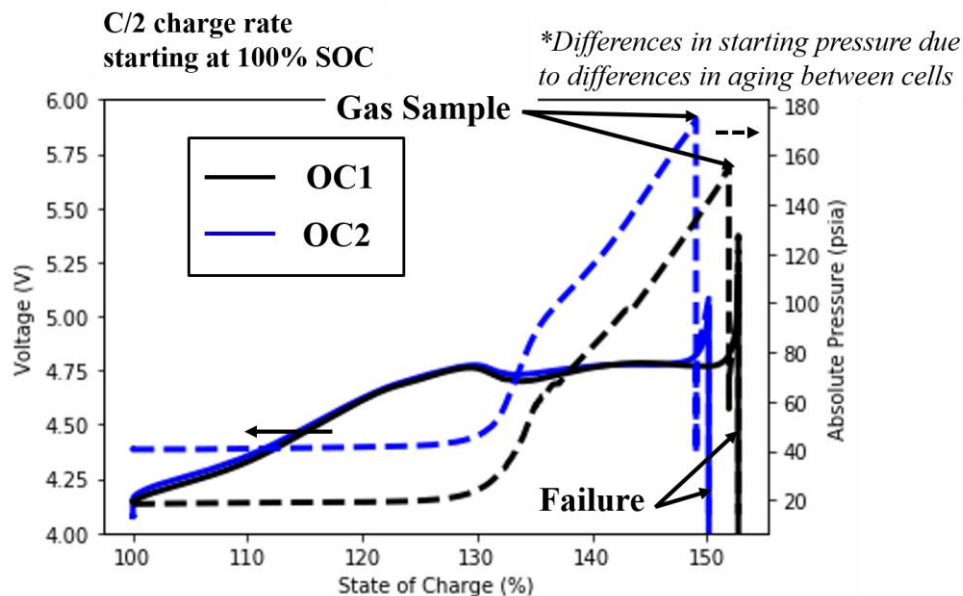


Figure 84: Overcharge test results with single gas sample taken

5.4.3 – Overcharge without gas samples

Overcharge tests are conducted on cells without collecting gas samples to minimize the free volume added with the full gas penetration and sampling apparatus. Cells were overcharged at either $C/2$ (26 A) or $C/5$ (10.4 A) until failure. The overcharge process can be separated into 4 different regimes based on the voltage, temperature, and pressure behavior. One of the cells overcharged at a $C/2$ rate is plotted in Figure 85 with the different stages labeled I-IV and the two cells overcharged at a $C/5$ rate are plotted in Figure 86. Stage I is characterized by an increase in the cell voltage above the electrolyte stability limit of approximately 4.5 V for carbonate solvent based electrolytes. During this stage, the internal pressure of the cell does not increase more than a few psi. At this point, either gas generation has not occurred or gas bubbles formed within the porous electrode structure have not diffused into the free volume of the cell headspace. Stage II is associated with a

nearly exponential increase in pressure while the voltage peaks followed by a decrease in voltage, although still above 4.6 V. During this stage, oxygen is released from the destabilized positive electrode and reactions between the electrolyte and the oxidized positive electrode are simultaneously producing gas. Based on the externally measured temperatures seen in Figure 86, the internal cell temperature is likely too low to initiate SEI layer decomposition. Stage III sees the pressure increase at a reduced rate as the voltage plateaus, indicating ongoing side reactions are occurring. Cell failure occurs shortly after entering into stage IV and sees a rapid increase in voltage and pressure before the cell casing bursts. At this point, lithium dendrites have likely formed due to the overly lithiated state of the negative electrode. The rapid pressure increase is indicative of a short circuit triggering a bursting of the cell casing.

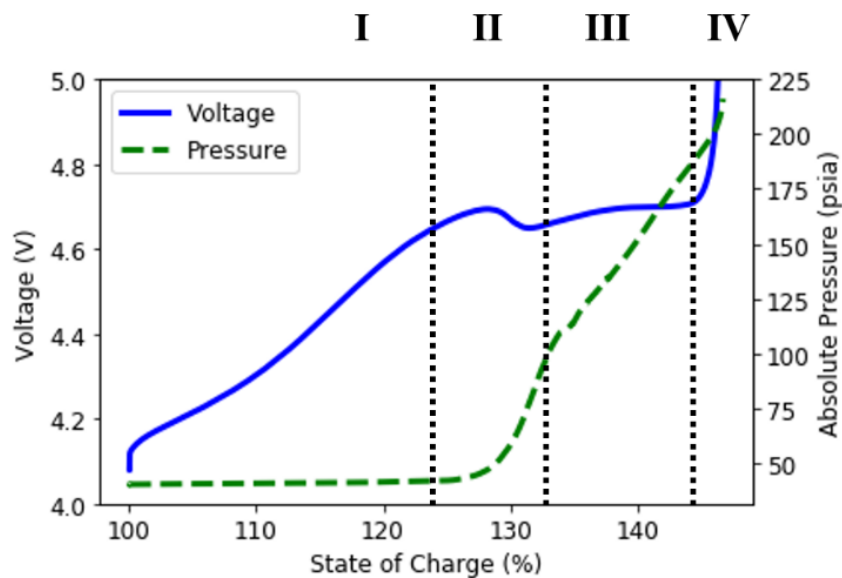


Figure 85: Overcharge at 26A (C/2 rate) can be separated into four different regimes. Failure occurs shortly after the cell enters into stage IV, in which rapid increases in voltage and pressure are observed.

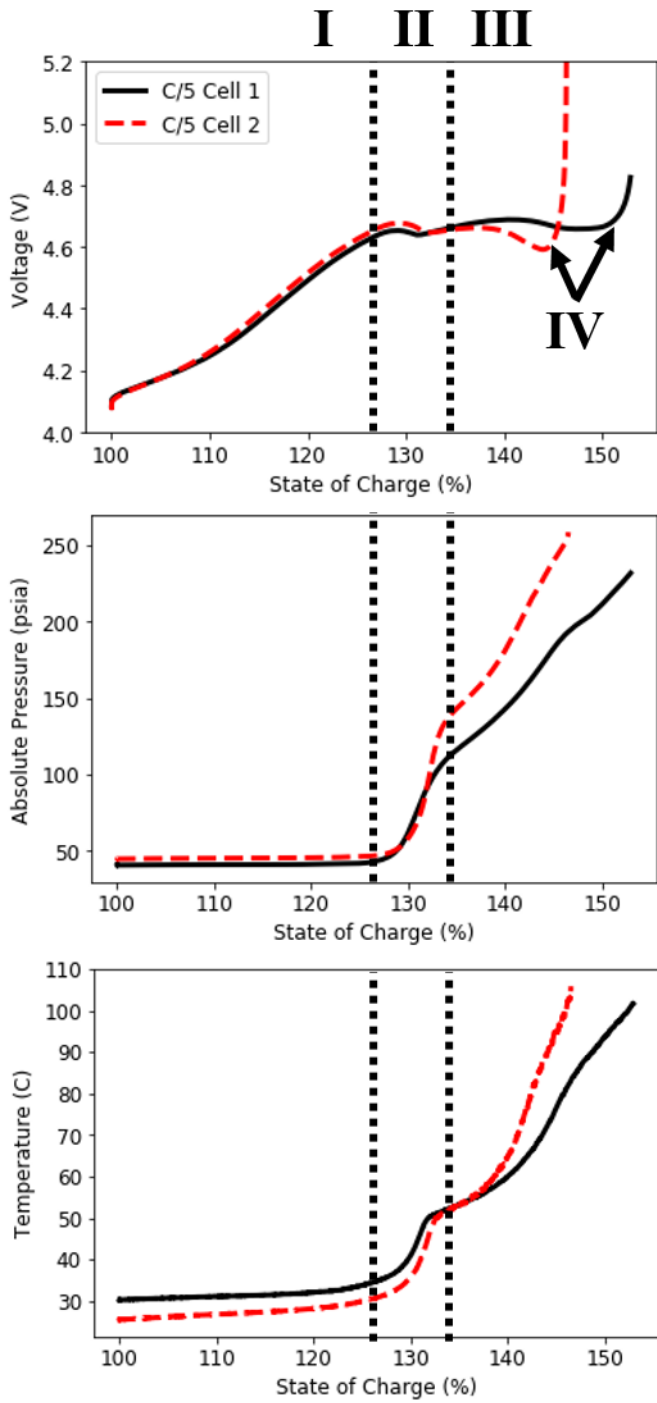


Figure 86: Overcharge of cells at 10.4 A (C/5) voltage (top), pressure (middle), temperature (bottom).

Chapter 6: Contributions, Future Work, and Conclusions

Lithium-ion batteries can undergo a variety of usage conditions throughout their life cycle. Even with the presence of protection circuitry and battery management systems, batteries can be operated outside of their manufacturers' recommended voltage, current, and temperature limits. Due to unintended operation or storage under non-ideal conditions, lithium-ion batteries can experience a variety of failure mechanisms that impact performance and safety. Battery performance and safety are critical for the host system to operate as intended without reducing capability or causing damage to the host system and its surroundings. In this research, failure mechanisms due to operation at voltage extremes (overdischarge and overcharge) and excessive temperatures (high temperature exposure) are elucidated. The research conducted significantly contributes to the state-of-the-art and provides critical knowledge into prominent failure mechanisms in lithium-ion batteries. The primary contributions of this work are:

- Developed a procedure for assembling three-electrode pouch cells and coin cells from disassembled large-format cells. Disassembly of large format cells is more complicated than commercial pouch and cylindrical (18650/26650) cells due to the higher energy content and associated risks of short-circuiting the electrodes during disassembled. The electrodes can then be placed in half-cell coin cells. The assembly of a three-electrode pouch cell using recovered electrodes allows for measurement of each individual electrode potential while also capturing interactions between the two electrodes.

- Developed a combined XPS/XAS approach to examine copper dissolution in lithium-ion cells. Previously, only the presence of copper was identified on lithium-ion battery components through the use of energy dispersive spectroscopy or inductively coupled plasma spectroscopy. These techniques do not provide chemical state information about the copper, and thus cannot provide any information about the propensity for a short circuit. The combination of XPS and XAS is necessary to observe both the surface (XPS) and bulk (XAS) properties of the deposited copper species.
- Identified the chemical state of copper resulting from current collector dissolution when a battery is overdischarged without entering into voltage reversal and subsequently recharged and cycled within typical operating ranges. The copper dissolves into the electrolyte and forms a mixture of Cu_2O and $\text{Cu}(\text{OH})_2$ on the surface of the electrodes. The state of the copper in overdischarged batteries has been assumed to be metallic copper, due to the failure mechanism experienced when cells are subjected to reversal; however, the failure mechanism when cells are overdischarged a single time is now demonstrated.
- Demonstrated that a single overdischarge event is not likely to result in a safety event. No evidence of short circuiting or sudden capacity loss were observed over at least 40 cycles. The rate of capacity fade did increase and was attributed to accelerated electrolyte decomposition due to the loss of intercalation sites and dislocation of active material from the conductive network.

- Development of a reliable, safe method for continuous internal pressure measurement in large-format lithium-ion cells. Pressures in excess of 225 psia were measured before the cell failed catastrophically without evidence of leaking.
- Measurement of internal pressure in a large-format lithium-ion cell as it undergoes abusive overcharge testing. Changes in pressure increase are well correlated with features of the voltage and temperature profiles and are attributable to gas generation mechanisms.

Future work can establish the effect of temperature and time of storage on the dissolution of copper and the likelihood of cell recovery. Experiments with three-electrode and optical cells can further elucidate the morphological changes associated with copper species deposition and electrode delamination, especially if combined with in-situ synchrotron radiation experiments to track the oxidation state of copper in a sealed cell. Continued cycling of overdischarged cells of various voltages can be performed to develop recovery guidelines for overdischarged cells.

The cell puncturing mechanism and gas pressure measurement apparatus can be improved to reduce the free volume of the measurement system. Development of a cell casing with a welded gas pressure fitting will also enable long-term measurement of gas pressure without leakage. This methodology could then be extended to smaller form-factor cells (18650, 26650) without needing to puncture the cell. Testing a larger number of cells with a reliable and consistent pressure measurement system can enable the development of a more generalizable model of gas generation as a function of different operating conditions. Further improvements in the gas sampling

and gas species measurement techniques can be used to develop chemical reactive models capturing the primary gas generation mechanisms. These models can be incorporated into a coupled thermal / mechanical / electrochemical / chemical model for battery diagnostics and prognostics.

Copper dissolution due to overdischarge is primarily a performance issue, although there are scenarios in which the increased cell impedance and gas pressure can put the cell in an unstable state, making it more susceptible to catastrophic failure. Understanding the threshold at which copper dissolution occurs for a given cell design (negative electrode and positive electrode chemistry, negative electrode to positive electrode active material ratio) is important for developing guidelines for cell recovery. When cells and battery packs are extremely costly or difficult to replace, as is the case for military and aerospace applications, it is critical to understand the potential benefits, risks, and trade-offs of recharging a battery that has been inadvertently overdischarged.

Overcharge and high temperature exposure are much more commonly associated with thermal runaway and catastrophic failure. This is due to a combination of the internal gas pressure and temperature rise that is seen as a result of the exothermic decomposition reactions inherent in lithium-ion battery materials. The differences in gas pressure rise observed for overcharge and high temperature exposure enables diagnostic and prognostic decision making. The data collected in this research can be used as inputs for modeling the mechanical interactions between internal gas pressure and the cell casing. This is tremendously useful for cell design in which alternate venting strategies may be employed to limit energy released during a

failure event or for modeling the venting electrolyte and fire propagation after a cell bursts. Knowledge of the gas pressure immediately preceding failure can be tremendously useful for simulating the effect of a failing battery on adjacent batteries. Furthermore, early failure detection through measurements of pressure or non-invasive measurements of the cell casing mechanical deformations (e.g., linear voltage displacement transducer, load cell, strain gauge) could be employed in applications where safety is critical and advanced warning of pressure buildup is advantageous.

Bibliography

1. T.B. Reddy and D. Linden (Eds.). (2011). Linden's Handbook of Batteries, 4th Edition. New York, NY: McGraw Hill
2. W. Du et al., "Energy density comparison of Li-ion cathode materials using dimensional analysis," Journal of the Electrochemical Society Vol. 160 Issue 8 (2013) pp. A1187-A1193.
3. W. F. Howard and R.M. Spotnitz, "Theoretical evaluation of high-energy lithium metal phosphate cathode materials in Li-ion batteries," Journal of Power Sources Vol. 165 Issue 2 (2007) pp.887-891.
4. M.A. Fetcenko et al., "Recent advances in NiMH Battery Technology," Journal of Power Sources Vol. 165 (2007) pp. 544-551.
5. C. Hendricks, N. Williard, S. Mathew, M. Pecht, A failure modes, mechanisms, and effects analysis (FMMEA) of lithium-ion batteries, J. Power Sources 297 (2015) 113–120.
6. Consumer Product Safety Commission, 2007 Recalls: Accessed on 6/18/14 from: <https://www.cpsc.gov/en/Recalls/2007/Sony-Recalls-Notebook-Computer-Batteries-Due-to-Previous-Fires/>
7. N. Williard, W. He, C. Hendricks, and M. Pecht, "Lessons learned from the 787 Dreamliner issue on lithium-ion battery reliability," Energies, Vol. 6 (2013) pp. 4682-4695.
8. E. Musk, "Tesla Adds Titanium Underbody Shield and Aluminum Deflector Plates to Model S," Accessed on 6/18/14 from:

<http://www.teslamotors.com/blog/tesla-adds-titanium-underbody-shield-and-aluminum-deflector-plates-model-s>

9. B. Mutzabaugh, “All of the USA’s big airlines now ban hoverboards,”
Accessed on 1/20/17 from:
<http://www.usatoday.com/story/travel/flights/todayinthesky/2015/12/10/delta-bans-hoverboards-airlines-fret-fire-risk/77110988/>
10. R. Campbell, “Electronic cigarette explosions and fires: the 2015 experience ,” Accessed on 1/20/17 from: <http://www.nfpa.org/news-and-research/fire-statistics-and-reports/fire-statistics/fire-causes/electrical-and-consumer-electronics/electronic-cigarette-explosions-and-fires-the-2015-experience>
11. T. Martin and J. McKinnon, “Samsung investigation blames battery size for Galaxy Note 7 fires,” Accessed on 1/20/17 from:
<http://www.wsj.com/articles/samsung-investigation-blames-battery-size-for-galaxy-note-7-fires-1484906193>
12. W.-J. Zhang, “A review of the electrochemical performance of alloy anodes for lithium-ion batteries,” *Journal of Power Sources*, Vol. 196, Issue 1 (2011) pp. 13-24.
13. J. W. Fergus, “Recent developments in cathode materials for lithium ion batteries,” *Journal of Power Sources*, Vol. 195, Issue 4 (2010) pp. 939-954.
14. X. Huang, “Separator technologies for lithium-ion batteries,” *J. Solid State Electrochem.*, 15 (2011) 649–662.

15. Y.P. Wu, E. Rahm, R. Holze, "Carbon anode materials for lithium ion batteries," *Journal of Power Sources*, Vol. 114, Issue 2 (2003) pp. 228-236
16. L. Yang, A. Xiao, and B. L. Lucht, "Investigation of solvation in lithium ion battery electrolytes by NMR spectroscopy," *J. Mol. Liq.*, 154 (2–3) (2010) 131–133.
17. H. Yang, G. V. Zhuang, and P. N. Ross Jr., "Thermal stability of LiPF₆ salt and Li-ion battery electrolytes containing LiPF₆," *J. Power Sources* 161 (1) (2006) 573-579B.
18. Scrosati and J. Garche, "Lithium batteries: Status, prospects and future," *J. Power Sources*, 195 (9) (2010) pp. 2419–2430.
19. G. G. Botte, R. E. White, Z. Zhang, "Thermal stability of LiPF₆-EC:EMC electrolyte for lithium ion batteries," *J. Power Sources* 97-98 (2001) 570-575.
20. J.S. Gnanaraj, E. Zinigrad, L. Asraf, H.E. Gottlieb, M. Sprecher, D. Aurbach, M. Schmidt, "The use of accelerating rate calorimetry (ARC) for the study of the thermal reactions of Li-ion battery electrolyte solutions," *J. Power Sources* 119-121 (2003) 794-798.
21. H. Ota, Y. Sakata, A. Inoue, and S. Yamaguchi, "Analysis of vinylene carbonate derived SEI layers on graphite anode," *J. Electrochem. Soc.*, 151 (10) (2004) A1659–A1669.
22. S. S. Zhang, "A review on electrolyte additives for lithium-ion batteries," *Journal of Power Sources*, Vol. 162, Issue 2 (2006) pp. 1379-1394.

23. V. A. Agubra and J. W. Fergus, "The formation and stability of the solid electrolyte interface on the graphite anode," *J. Power Sources*, 268 (2014) 153–162.
24. P. Arora, R. E. White, and M. Doyle, "Capacity fade mechanisms and side reactions in Lithium-ion batteries," *J. Electrochem. Soc.*, 145 (1998) 3647–3667.
25. S.-H. Lee, H.-G. You, K.-S. Han, J. Kim, I.-H. Jung, and J.-H. Song, "A new approach to surface properties of solid electrolyte interphase on a graphite negative electrode," *J. Power Sources*, 247 (2014) 307–313.
26. T. Ohzuku, Y. Iwakoshi, and K. Sawai, "Formation of lithium-graphite intercalation compounds in nonaqueous electrolytes and their application as a negative electrode for a lithium ion (shuttlecock) cell," *J. Electrochem. Soc.*, 140 (9) (1993) 2490–2498.
27. V.A. Sethuraman, "Surface structural disordering in graphite upon lithium intercalation/deintercalation," *Journal of Power Sources*, Vol. 195 (2010) pp. 3655-3660
28. J. Fan and S. Tan, "Studies on charging lithium-ion cells at low temperatures," *J. Electrochem. Soc.*, 153 (6) (2006) A1081–A1092.
29. J.-N. Chazalviel, "Electrochemical aspects of the generation of ramified metallic electrodeposits," *Phys. Rev. A*, 42 (1990) 7355–7367
30. P. Arora, M. Doyle, R. E. White, "Mathematical modeling of the lithium deposition overcharge reaction in lithium-ion batteries using carbon-based negative electrodes," *J. Electrochem. Soc.*, 146 (10) (1999) 3543–3553.

31. C. Monroe and J. Newman, "Dendrite growth in lithium/polymer systems: A propagation model for liquid electrolytes under galvanostatic conditions," *J. Electrochem. Soc.*, 150 (10) (2003) A1377–A1384.
32. K. Nishikawa, T. Mori, T. Nishida, Y. Fukunaka, and M. Rosso, "Li dendrite growth and Li⁺ ionic mass transfer phenomenon," *J. Electroanal. Chem.*, 661 (2011) 84–89.
33. R. Akolkar, "Modeling dendrite growth during lithium electrodeposition at sub-ambient temperature," *J. Power Sources*, 246 (2014) 84–89.
34. Jana, D. R. Ely, R. E. García, "Dendrite-separator interactions in lithium-based batteries," *J. Power Sources*, 275 (2015) 912–921
35. T. Love, O. A. Baturina, and K. E. Swider-Lyons, "Observation of lithium dendrites at ambient temperature and below," *Electrochem. Soc. Electrochem. Lett.*, 4 (2) (2015) A24–A27.
36. R. Bhattacharyya, B. Key, H. Chen, A. S. Best, A. F. Hollenkamp, and C. P. Grey, "In situ NMR observation of the formation of metallic lithium microstructures in lithium batteries," *Nature Mater.*, 9 (2010) 504–510.
37. M. Zier, F. Scheiba, S. Oswald, J. Thomas, D. Goers, T. Scherer, M. Klose, H. Ehrenberg, and J. Eckert, "Lithium dendrite and solid electrolyte interphase investigation using OsO₄," *J. Power Sources*, 266 (2014) 198–207.
38. Ganesan, V. Evely, D. Das, and M. Pecht, "Identification and utilization of failure mechanisms to enhance FMEA and FMECA," *Proc. IEEE Workshop Accel. Stress Test. Reliab. (ASTR)*, Austin, TX, Oct 3–5 (2005).

39. J. Hu, D. Barke, A. Dasgupta, and A. Arora, "Role of failure-mechanism identification in accelerated testing," *J. IES*, 36 (4) (1993) 39–45.
40. S. Cheng, M. Azarian, and M. Pecht, "Sensor systems for prognostics and health management," *Sensors*, 10 (2010) 5774–5797.
41. S. Mathew, M. Alam, and M. Pecht, "Identification of failure mechanisms to enhance prognostic outcomes," *J. Fail. Anal. Prev.*, 12 (2012) 66–73.
42. N. Dupré, J.-F. Martin, D. Guyomard, A. Yamada, and R. Kanno, "Characterization of interphases appearing on $\text{LiNi}_{0.5}\text{Mn}_{0.5}\text{O}_2$ using ^7Li MAS NMR," *J. Power Sources*, 189 (2009) 557-560.
43. N. Leifer, M. C. Smart, G. K. S. Prakash, L. Gonzalez, L. Sanchez, K. A. Smith, P. Bhalla, C. P. Grey, and S. G. Greenbaum, " ^{13}C Solid state NMR suggests unusual breakdown products in SEI formation on Lithium ion electrodes," *J. Electrochem. Soc.*, 158 (5) (2011) A471–A480.
44. F. M. Wang, D. T. Shieh, J. H. Cheng, and C. R. Yang. "An investigation of the salt dissociation effects on solid electrolyte interface (SEI) formation using linear carbonate-based electrolytes in lithium ion batteries," *Solid State Ionics*, 180 (40) (2010), 1660–1666.
45. J. T. Lee, N. Nitta, J. Benson, A. Magasinski, T. F. Fuller, and G. Yushin, "Comparative study of the solid electrolyte interphase on graphite in full Li-ion battery cells using X-ray photoelectron spectroscopy, secondary ion mass spectrometry, and electron microscopy," *Carbon*, 52 (2013) 388–397.

46. M. Herstedt, A. M. Andersson, H. Rensmo, H. Siegbahn, and K. Edstrom, "Characterisation of the SEI formed on natural graphite in PC-based electrolytes," *Electrochim. Acta*, 49 (27) (2004) 4939–4947
47. V. A. Agubra, J. W. Fergus, R. Fu, and S.-Y. Choe, "Analysis of effects of the state of charge on the formation and growth of the deposit layer on graphite electrode of pouch type lithium ion polymer batteries," *J. Power Sources*, 270 (2014) 213–220.
48. V. A. Agubra, J. W. Fergus, R. Fu, and S.-Y. Choe, "Analysis of the deposit layer from electrolyte side reaction on the anode of the pouch type lithium ion polymer batteries: The effect of state of charge and charge rate," *Electrochim. Acta*, 149 (2014), 1–10.
49. K. Edström, M. Herstedt, and D. P. Abraham, "A new look at the solid electrolyte interphase on graphite anodes in Li-ion batteries," *J. Power Sources*, 153 (2) (2006) 380–384.
50. S. Leroy, F. Blanchard, R. Dedryvère, H. Martinez, B. Carré, D. Lemordant, and D. Gonbeau, "Surface film formation on a graphite electrode in Li-ion batteries: AFM and XPS study," *Surf. Interface Anal.*, 37 (10) (2005) 773–781.
51. G. V. Zhuang, K. Xu, T. R. Jow, and P. N. Ross, "Study of SEI layer formed on graphite anodes in PC/LiBOB electrolyte using IR spectroscopy," *Electrochem. Solid State Lett.*, 7 (8) (2004) A224–A227.

52. K. Kwon, F. P. Kong, F. McLarnon, and J. W. Evans, "Characterization of the SEI on a carbon film electrode by combined EQCM and spectroscopic ellipsometry," *J. Electrochem. Soc.*, 150 (2) (2003) A229–A233
53. M. Broussely, S. Herreyre, P. Biensan, P. Kasztejna, K. Nechev, and R. J. Staniewicz, "Aging mechanism in Li ion cells and calendar life predictions," *J. Power Sources*, 97–98 (2001) 13–21.
54. R. Spotnitz, "Simulation of capacity fade in Lithium-ion batteries," *J. Power Sources*, 113 (2003) 72–80.
55. P. Ramadass, B. Haran, P. Gomadam, R. White, and B. Popov, "Development of first principles capacity fade model for Li-ion cells," *J. Electrochem. Soc.*, 151 (2) (2004) A196–A203.
56. H. J. Ploehn, P. Ramadass, and R. E. White, "Solvent diffusion model for aging of lithium-ion battery cells," *J. Electrochem. Soc.*, 151 (3) (2004) A456–A462.
57. X. Zhang, W. Shyy, and A. M. Sastry, "Numerical simulation of intercalation-induced stress in Li-ion battery electrode particles," *J. Electrochem. Soc.*, 154 (2007) A910–A916.
58. S. Renganathan, G. Sikha, S. Santhanagopalan, and R. E. White, "Theoretical analysis of stresses in a lithium-ion cell," *J. Electrochem. Soc.*, 157 (2010) A155–A163.
59. J. Christensen and J. Newman, "Stress generation and fracture in lithium insertion materials," *J. Solid State Electrochem.*, 10 (2006) 293–319.

60. J. Christensen and J. Newman, "A mathematical model of stress generation and fracture in lithium manganese oxide," *J. Electrochem. Soc.*, 153 (6) (2006) A1019–A1030.
61. R. Purkayastha and R. McMeeking, "A parameter study of intercalation of lithium into storage particles in a lithium-ion battery," *Comput. Mater. Sci.*, 80 (2013) 2–14.
62. Z. Choi, D. Kramer, and R. Moenig, "Correlation of stress and structural evolution in $\text{Li}_4\text{Ti}_5\text{O}_{12}$ -based electrodes for lithium ion batteries," *J. Power Sources*, 240 (2013) 245–251.
63. A.-C. Walk, M. Huttin, and M. Kamlah, "Comparison of a phase-field model for intercalation induced stresses in electrode particles of lithium ion batteries for small and finite deformation theory," *Eur. J. Mech. - A/Solids*, 48 (2014) 74–82.
64. S. Bhattacharya, A. R. Riahi, and A. T. Alpas, "A transmission electron microscopy study of crack formation and propagation in electrochemically cycled graphite electrode in lithium-ion cells," *J. Power Sources* 196 (20) (2011) 8719-8727.
65. B. M. L. Rao, R. W. Francis, and H. A. Christopher, "Lithium-aluminum electrode," *J. Electrochem. Soc.*, 124 (10) (1977) 1490–1492.
66. J.-M. Tarascon and M. Armand, "Issues and challenges facing rechargeable lithium batteries," *Nature*, 414 (2001) 359–367.
67. J. Vetter et al., "Ageing mechanisms in lithium-ion batteries," *J. Power Sources*, 147 (2005) 269–281.

68. M. Ender, J. Joos, T. Carraro, and E. Ivers-Tiffée, "Three-dimensional reconstruction of a composite cathode for lithium-ion cells," *Electrochem. Comm.* 13 (2) (2011) 166-168.
69. M. Ender, J. Joos, A. Weber, and E. Ivers-Tiffée, "Anode microstructures from high-energy and high-power lithium-ion cylindrical cells obtained by X-ray nano-tomography," *J. Power Sources* 269 (2014) 912-919.
70. J. Dahn, J. R. Fong, and M. Spoon. "Suppression of staging in lithium-intercalated carbon by disorder in the host." *Physical Review B*, Vol. 42, Issue 10 (1990) pp. 6424-6432.
71. J. Dahn, "Phase Diagram of Li_xC_6 ," *Physical Review B.*, Vol. 44, Issue 17 (1991), pp. 9170-9177
72. B. Key, R. Bhattacharyya, M. Morcrette, V. Seznéc, J.M. Tarascon, and C.P. Grey. "Real-time NMR investigations of structural changes in silicon electrodes for lithium-ion batteries." *Journal of the American Chemical Society*, Vol. 131, Issue 26 (2009) pp. 9239-49.
73. U. Kasavajjula, C. Wang, A. J. Appleby, "Nano- and bulk-silicon-based insertion anodes for lithium-ion secondary cells," *Journal of Power Sources*, Vol. 163, Issue 2 (2007) pp. 1003-1039
74. B.A. Boukamp, G.C. Lesh, and R.A. Huggins, "All-solid lithium electrodes with mixed-conductor matrix," *Journal of the Electrochemical Society*, Vol. 128, Issue 4 (1981) pp. 725-729

75. K. Padhi, K. S. Nanjundaswamy, and J. B. Goodenough, "Phospho-olivines as positive-electrode materials for rechargeable lithium batteries," *J. Electrochem. Soc.*, 144 (2) (1997) 1188–1194.
76. M. Y. Saïdi, J. Barker, and R Koksang. "Structural and electrochemical investigation of lithium insertion in the $\text{Li}_{1-x}\text{Mn}_2\text{O}_4$ spinel phase." *Electrochimica Acta*. Vol. 41, Issue 2 (1996), pp. 199-204.
77. J. N. Reimers and J. R. Dahn, "Electrochemical and in situ X-ray diffraction studies of Lithium intercalation in Li_xCoO_2 ," *Journal of the Electrochemical Society*, Vol. 139, Issue 8, 1992, pp. 2091-2097
78. R.-Z. Yin, Y.-S. Kim, S.-J. Shin, I. Jung, J.-S. Kim, and S.-K. Jeong, "In situ XRD investigation and thermal properties of Mg doped LiCoO_2 for lithium ion batteries," *Journal of the Electrochemical Society*, Vol. 159, Issue 3 (2012) pp. A253-A258.
79. Manthiram and J. Choi, Chemical and structural instabilities of lithium ion battery cathodes, *J. Power Sources* 159 (2006) p. 249-253.
80. P. Mukherjee, et al., Surface structural and chemical evolution of layered $\text{LiNi}_{0.8}\text{Co}_{0.15}\text{Al}_{0.05}\text{O}_2$ (NCA) under high voltage and elevated temperature conditions, *Chem. Mater.* 30 (2018) p. 8431-8445.
81. M. Onuki, et al. Identification of the source of evolved gas in Li-ion batteries using ^{13}C -labeled solvents, *J. Electrochem. Soc.* 155 (11) (2008) p. A794-A797.

82. L. Xing, et al. Theoretical investigations on oxidative stability of solvents and oxidative decomposition mechanism of ethylene carbonate for lithium ion battery use, *J. Phys. Chem. B.* 113 (2009) p. 16596-16602.
83. J. Xu, Y. Hu, T. Liu, and X. Wu, "Improvement of cycle stability for high-voltage lithium-ion batteries by in-situ growth of SEI film on cathode," *Nano Energy*, 5 (2014) 67–73.
84. S. Tan, Z. Zhang, Y. Li, Y. Li, J. Zheng, Z. Zhou, and Y. Yang, "Tris(hexafluoro-iso-propyl)phosphate as an SEI-forming additive on improving the electrochemical performance of the $\text{Li}[\text{Li}_{0.2}\text{Mn}_{0.56}\text{Ni}_{0.16}\text{Co}_{0.08}]\text{O}_2$ cathode material," *J. Electrochem. Soc.*, 160 (2) (2013) A285–A292.
85. T. Kawamura, A. Kimura, M. Egashira, S. Okada, and J.-I. Yamaki, "Thermal stability of alkyl carbonate mixed-solvent electrolytes for lithium ion cells," *J. Power Sources*, 104 (2) (2002) 260–264.
86. W. Kong, H. Li, X. Huang, and L. Chen, "Gas evolution behaviors for several cathode materials in lithium-ion batteries," *J. Power Sources*, 142 (2005) 285–291.
87. K.-W. Nam, S.-M. Bak, E. Hu, X. Yu, Y. Zhou, X. Wang, L. Wu, Y. Zhu, K.-Y. Chung, and X.-Q. Yang, "Combining in situ synchrotron X-ray diffraction and absorption techniques with transmission electron microscopy to study the origin of thermal instability in overcharged cathode materials for lithium-ion batteries," *Adv. Funct. Mater.*, 23 (8) (2013) 1047–1063.

88. J. W. Braithwaite, A. Gonzales, G. Nagasubramanian, S. J. Lucero, D. E. Peebles, J. A. Ohlhausen, and W. R. Cieslak, "Corrosion of lithium-ion battery current collectors," *J. Electrochem. Soc.*, 146 (2) (1999) 448–456.
89. M. Xu and H. D. Dewald, "Controlled-potential electrolysis of copper foil and graphite-coated copper foil in a nonaqueous 1 M LiPF₆ in a ternary organic carbonate solvent," *Microchem. J.*, 81 (2005) 225–229.
90. S. S. Zhang and T. R. Jow, "Aluminum corrosion in electrolyte of Li-ion battery," *J. Power Sources*, 109 (2) (2002) 458–464.
91. E. Cho et al., "Corrosion/passivation of aluminum current collector in bis(fluorosulfonyl)imide-based ionic liquid for lithium-ion batteries," *Electrochem. Commun.*, 22 (2012) 1–3.
92. P. Arora and Z. Zhang, "Battery separators," *Chem. Rev.*, 104 (2004) 4419–4462.
93. C. Peabody and C. B. Arnold, "The role of mechanically induced separator creep in lithium-ion battery capacity fade," *J. Power Sources*, 196 (19) (2011) 8147–8153.
94. G. Venugopal, J. Moore, J. Howard, and S. Pandalwar, "Characterization of microporous separators for lithium-ion batteries," *J. Power Sources*, 77 (1) (1999) 34–41.
95. W. Wu, X. Xiao, X. Huang, and S. Yan, "A multiphysics model for the in situ stress analysis of the separator in a lithium-ion battery cell," *Comput. Mater. Sci.*, 83 (2014) 127–136.

96. G.-H. Kim, A. Pesaran, and R. Spotnitz, "A three-dimensional thermal abuse model for lithium-ion cells," *J. Power Sources*, 170 (2007) 476–489.
97. S. Santhanagopalan, P. Ramadass, and J. Zhang, "Analysis of internal short-circuit in a Lithium-ion cell," *J. Power Sources*, 194 (2009) 550–557.
98. T. G. Zavalis, B. Behm, and G. Lindbergh, "Investigation of short-circuit scenarios in a Lithium-ion battery cell," *J. Electrochem. Soc.*, 159 (6) (2012), A848–A859.
99. National Highway Transportation Safety Administration, Chevrolet Volt battery incident overview report, 2012, accessed on 1/11/15 from:
<http://www-odi.nhtsa.dot.gov/acms/cs/jaxrs/download/doc/UCM399393/INRP-PE11037-49880.pdf>
100. B. Reich and E. B. Hakim, "Environmental factors governing field reliability of plastic transistors and integrated circuits," *Reliab. Phys. Symp.*, (1972) 82–87.
101. E. Bumiller and C. Hillman, "A review of models for time-to-failure due to metallic migration mechanisms," DfR Solutions White Paper, 2012, accessed on 8/22/13 from: <http://www.dfrsolutions.com/wp-content/uploads/2012/06/Review-of-Models-for-Time-to-Failure-Due-to-Metallic-Migration-Mechanisms.pdf>
102. R. T. Howard, "Electrochemical model for corrosion of conductors on ceramic substrates," *IEEE Trans. Compon., Hybrids, Manuf. Technol.*, 4 (4) (1981) 520–525.

103. M. Pecht and W. C. Ko, "A corrosion rate equation for microelectronic die metallization," *Int. J. Hybrid Microelectron.*, 13 (2) (1990) 42–51.
104. E. Sahraei, J. Campbell, and T. Wierzbicki, "Modeling and short circuit detection of 18650 Li-ion cells under mechanical abuse conditions," *J. Power Sources*, 220 (2012) 360–372.
105. E. Sahraei, J. Meier, and T. Wierzbicki, "Characterizing and modeling mechanical properties and onset of short circuit for three types of lithium-ion pouch cells," *J. Power Sources*, 247 (2014) 503–516.
106. M. Zhao, S. Kariuki, H.D. Dewald, F.R. Lemke, R.J. Staniewicz, E.J. Plichta, and R.A. Marsh, Electrochemical stability of copper in lithium-ion battery electrolytes, *J Electrochem Soc*, Vol. 147 (8) (2000) p. 2874-2879.
107. M. Zhao, H. D. Dewald, and R. J. Staniewicz, Quantitation of the dissolution of battery-grade copper foils in lithium-ion battery electrolytes by flame atomic absorption spectroscopy, *Electrochim Acta*, Vol. 49 (2004) p. 683-689.
108. M. Zhao, H.D. Dewald, F. R. Lemkie, and R.J. Staniewicz, Electrochemical stability of graphite-coated copper in lithium-ion battery electrolytes, *J Electrochem Soc*, Vol. 147 (11) (2000) p. 3983-3988.
109. M. Zhao, H.D. Dewald, and R.J. Staniewicz, Quantitation of the dissolution of the graphite-coated copper foil in lithium-ion battery electrolytes by flame absorption spectroscopy, *Electrochim Acta*, Vol. 49 (2004) p. 677-681.
110. L. Wu, Y. Liu, Y. Cui, Y. Zhang, and J. Zhang, In situ temperature evolution and failure mechanisms of $\text{LiNi}_{0.33}\text{Mn}_{0.33}\text{Co}_{0.33}\text{O}_2$ cell under over-

- discharge conditions, *J Electrochem Soc*, Vol. 165 (10) (2018) p. A2162-A2166.
111. J. Kasnatscheew, M. Börner, B. Steipert, P. Meister, R. Wagner, I.C. Laskovic, and M. Winter, Lithium ion battery cells under abusive discharge conditions: electrode potential development and interactions between positive and negative electrode, *J Power Sources*, Vol. 362 (2017) p. 278-282.
112. C. Fear, D. Juarez-Robles, J. A. Jeevarajan, and P. P. Mukherjee, Elucidating copper dissolution phenomenon in li-ion cells under overdischarge extremes, *J Electrochem Soc*, Vol. 165 (9) (2018) p. A1639-A1647.
113. H. He, Y. Liu, Q. Liu, Z. Li, F. Xu, C. Dun, Y. Ren, M-x. Wang, and J. Xie, Failure investigations of LiFePO₄ cells in over-discharge conditions, *J Electrochem Soc*, Vol. 160 (6) (2013) p. A793-A804.
114. R. Guo, L. Lu, M. Ouyang, and X. Feng, Mechanism of the entire overdischarge process and overdischarge-induced internal short circuit in lithium-ion batteries, *Sci Rep-UK*, Vol. 6 (2016) p. 1- 9.
115. H. Maleki and J. N. Howard, Effects of overdischarge on performance and thermal stability of a Li-ion cell, *J Power Sources*, Vol. 160 (2006) p.1395-1402.
116. K. R. Crompton and B. J. Landi, Opportunities for near zero volt storage of lithium ion batteries, *Energy Environ Sci*, Vol. 9 (2016) p. 2219-2239.
117. D. Fuentevilla, C. Hendricks, and A. Mansour, Quantifying the impact of overdischarge on large-format lithium-ion cells, *ECS Trans*, 69 (20) (2015) p. 1-4.

118. C. Hendricks, A. Mansour, D. Fuentevilla, J. Ko, G. Waller, Copper Dissolution Investigations in Large-Format Lithium-ion Cells, 48th Power Sources Conference, June 11, 2018
119. H.-F. Li, J.-K. Gao, and S.-L. Zhang, Effect of overdischarge on swelling and recharge performance of lithium ion cells, Chinese J of Chem, Vol 26 (2008) p. 1585-1588.
120. K. Kumai, H. Miyashiro, Y. Kobayashi, K. Takei, and R. Ishikawa, Gas generation mechanism due to electrolyte decomposition in commercial lithium-ion cell, J Power Sources, Vol. 81-82 (1999) p. 715-719.
121. C. Love and A. Gaskins, Performance loss of lithium ion polymer batteries subjected to overcharge and overdischarge abuse, Memorandum Report, NRL/MR/6110 -- 12-9455 (2012) p. 1-19.
122. APS Systems Map, <https://www.aps.anl.gov/About/Overview/APS-Systems-Map>, accessed on 10/3/18.
123. B. Ravel and M. Newville, ATENA, ARTEMIS, HEPHAESTUS: data analysis for X-ray absorption spectroscopy using IFEFFIT, J. of Sync. Rad. 12 (2005), pp. 537-541
124. N.S. McIntyre and M.G. Cook, X-ray photoelectron studies on some oxides and hydroxides of Cobalt, Nickel, and Copper, Anal Chem, 47 (13) (1975) p. 2208-2213.
125. H.R. Oswald, A. Reller, H.W. Schmalle, and E. Dubler, Structure of Copper (II) Hydroxide, $\text{Cu}(\text{OH})_2$, Acta Cryst Sec C, Vol. 46 (12) (1990) p. 2279-2284.

126. A.N. Mansour, F. Badway, W.S. Yoon, K.Y. Chung, and G.G. Amatucci, In-situ X-ray absorption spectroscopic investigation of the electrochemical conversion reactions of CuF₂-MoO₃ nanocomposite, *Journal of Solid State Chemistry* 183 (2010) pp. 3029-3038.
127. N. V. Mdlovu, C.-L. Chiang, K.-S. Lin, and R.-C. Jeng, Recycling copper nanoparticles from printed circuit board waste etchants via a microemulsion process, *Journal of Cleaner Production* 185 (2018) pp. 781-796.
128. D. L. Schulz, C. J. Curtis, and D. S. Ginley, Surface chemistry of copper nanoparticles and direct spray printing of hybrid particle/metalorganic inks, *Electrochemical and Solid-State Letters* 4 (8) (2001) pp. C58-C61.
129. P. Villars, L.D. Calvert, *Pearson's Handbook of Crystallographic Data for Intermetallic Phases*, vol. 2, American Society for Metals, Metals Park, OH, 1985, p. 19943.
130. Q. Wang, P. Ping, X. Zhao, G. Chu, J. Sun, C. Chen, "Thermal runaway caused fire and explosion of lithium ion battery," *Journal of Power Sources*, Vol. 208 (2012) pp. 210-224.
131. J. Vetter, P. Novák, M.R. Wagner, C. Veit, K.-C. Möller, J.O. Besenhard, M. Winter, M. Wohlfahrt-Mehrens, C. Vogler, and A. Hammouche, "Ageing mechanisms in lithium-ion batteries," *Journal of Power Sources*, Vol. 147, No. 1-2 (2005) pp. 269-281

132. T. Ohzuku, N. Matoba, and K. Sawai, "Direct evidence on anomalous expansion of graphite-negative electrodes on first charge by dilatometry," *Journal of Power Sources*, Vol. 97–98 (2001) pp. 73-77
133. T. Ohsaki, T. Kishi, T. Kuboki, N. Takami, N. Shimura, Y. Sato, M. Sekino, and A. Satoh, Overcharge reaction of lithium-ion batteries, *J. Power Sources* 146 (2005) p. 97-100.
134. R. A. Leising, M. J. Palazzo, E.S. Takeuchi, and K. J. Takeuchi, Abuse testing of Lithium-ion batteries, *J. Electrochem Soc.* 148 (8) (2001) p. A838-A444.
135. E. Roth, C. Crafts, D. Doughty, and J. McBreen, "Advanced technology development program for lithium-ion batteries: thermal abuse performance of 18650 li-ion cells," Sandia National Laboratory Report, SAND2004-0584, 2004
136. Y. Fernandes, A. Bry, S. de Persis, Identification and quantification of gases emitted during abuse tests by overcharge of a commercial Li-ion battery, *J. Power Sources* 389 (2018) pp. 106-119.
137. D. Belov and M.-H. Yang, Failure mechanism of li-ion battery at overcharge conditions, *J. Solid State Electrochem* 12 (2008) p. 885-894
138. K. H. Lee, E. H. Song, J. Y. Lee, B. H. Jung, H.S. Lim, Mechanism of gas build-up in a Li-ion cell at elevated temperature, *J. Power Sources* 132 (2004) p. 201-205.

139. A.W. Golubkov, et al., Thermal-runaway experiments on consumer Li-ion batteries with metal-oxide and olvin-type cathodes, *RSC Advances* 4 (2014) p. 3633-3642.
140. B. Michalak, H. Sommer, D. Mannes, A. Kaestner, T. Brezesinski, J. Janek, Gas evolution in operating lithium-ion batteries studied in situ by neutron imaging, *Sci. Rep.* 5 (15627) (2015) p. 1-9
141. B. Sood, C. Hendricks, M. Osterman, and M. Pecht, "Health Monitoring of Lithium-ion Batteries," *Electronic Device Failure Analysis*, Vol. 16, No. 2 (2014) pp. 4-16.
142. V. Somandepalli, K. C. Marr, Q. Horn, Explosion hazards due to failures of lithium-ion batteries, 9th Global Congress on Process Safety
143. P.T. Coman, S. Rayman, and R.E. White, A lumped model of venting during thermal runaway in a cylindrical lithium cobalt oxide lithium-ion cell, *J. Power Sources* 307 (2016) p. 56-62
144. P.T. Coman, S. Matefi-Tempfli, C.T. Veje, and R.E. White, Modeling vaporization, gas generation and venting in li-ion battery cells with a dimethyl carbonate electrolyte, *J. Electrochem Soc.* 164 (9) (2017) p. A1858-A1865.
145. M. Ottaway, in *AWbriefing* (2015) p. 13.